Coarse-Graining Frequency-Dependent Phenomena and Memory in Soft Matter Systems

Dissertation

vorgelegt von

Gerhard Jung

geboren in Wiesbaden

Mainz, den 15. Mai 2018

JG|U

JOHANNES GUTENBERG
UNIVERSITÄT MAINZ

Teile dieser Dissertation wurden veröffentlicht:

"Computing bulk and shear viscosities from simulations of fluids with dissipative and stochastic interactions",
Gerhard Jung and Friederike Schmid,
The Journal of Chemical Physics, **144**, 204104 (2016)

"Iterative reconstruction of memory kernels",
Gerhard Jung, Martin Hanke and Friederike Schmid,
Journal of Chemical Theory and Computation, **13**, 2481 (2017)

Zusammenfassung

Vergröberung von frequenzabhängigen Phänomenen und "Gedächtnis" in der Physik weicher Materie

In den letzten Jahren hat sich der Fokus in der Physik weicher Materie stark von Gleichgewichts- zu Nichtgleichgewichtssystemen verschoben. Das vielleicht beste Beispiel dafür ist die derzeitige Popularität von aktiven Teilchen und Mikroschwimmern in der Forschung. Eine wichtige Eigenschaft von Prozessen im Nichtgleichgewicht ist ihre Abhängigkeit von den dynamischen Eigenschaften des Systems. Dies verkompliziert die Herleitung von vergröberten Modellen erheblich, da diese automatisch eine stark veränderte Dynamik aufweisen. In dieser Doktorarbeit untersuchen und vergröbern wir frequenzabhängige Phänomene in der Physik weicher Materie. Die in dieser Arbeit vorgestellten Methoden sind weiterhin auf Gleichgewichtssysteme beschränkt, allerdings stellen sie einen wichtigen Schritt zur Entwicklung von Vergröberungstechniken von Nichtgleichgewichtssimulationen dar.

Im ersten Teil dieser Doktorarbeit werden die dielektrischen Eigenschaften von Polyelektrolyten in ionischer Lösung analysiert. Wir können zeigen, dass die elektrische Polarisierbarkeit stark von der Qualität des Lösungsmittels abhängt. Aufgrund der überlappenden Relaxationszeitskalen beobachten wir außerdem eine nicht-monotone Frequenzabhängigkeit der dielektrischen Eigenschaften des Polyelektrolyts. Im Anschluss werden die hydrodynamischen Wechselwirkungen von gelösten Nanokolloiden untersucht. Auch diese Studie zeigt, dass physikalische Prozesse auf unterschiedlichen aber überlappenden Zeitskalen "Gedächtniseffekte" im System hervorrufen. Zum Beispiel erzeugt die Bewegung eines Nanokolloids Wirbel im Lösungsmittel, welche seine eigene Dynamik und die Bewegung benachbarter Kolloide beeinflussen. Diese "Gedächtniseffekte" können mithilfe der verallgemeinerten Langevin Gleichung beschrieben werden, indem man frequenzabhängige Reibungsfunktionen und zeitkorrelierte Zufallskräfte einführt.

Um diese Erkenntnisse für dynamisches Vergröbern zu nutzen, haben wir zwei neuartige Methoden entwickelt: Die "iterative Gedächtnisrekonstruktion", um systematisch Gedächtnisfunktionen von mikroskopischen Systemen herzuleiten, und die "verallgemeinerte Brownsche Dynamik", um die verallgemeinerte Langevin Gleichung zu lösen. Die Kombination dieser Techniken ermöglicht die Erzeugung eines vergröberten nicht-Markovschen Modells der gelösten Nanokolloide, welches die Dynamik des zugrundeliegenden mikroskopischen Systems perfekt reproduziert. Die Besonderheit dieses Modells ist, dass es nicht nur die Selbstdiffusion der Kolloide nachstellt, sondern auch die korrekten Kreuzkorrelationen zwischen unterschiedlichen Teilchen integriert. Zusätzlich können wir zeigen, dass die Zeitintegration dieses transferierbaren vergröberten Modells etwa 10^4 Mal schneller ist als die ursprünglichen Molekulardynamik-Simulationen.

Abstract

Coarse-Graining Frequency-Dependent Phenomena and Memory in Soft Matter Systems

In recent years, the focus of soft matter science has shifted more and more from equilibrium to non-equilibrium systems. One of the best examples for this trend is the popularity of active matter and microswimmers in modern research. One major feature of non-equilibrium processes is their strong dependence on the dynamical properties of the system. This complicates the construction of coarse-grained models for these systems, because the coarse-graining inherently changes their dynamics. In this thesis, we investigate and coarse-grain frequency-dependent phenomena in soft matter science. The methods proposed in this work are still restricted to systems in equilibrium, however, they represent an important first step to develop coarse-graining techniques for non-equilibrium simulations.

In the first part of this thesis we investigate the dielectric properties of flexible polyelectrolytes in ionic solution. We can demonstrate that the electric polarizability strongly depends on the solvent quality. Due to the overlapping of different relaxation times, it is also revealed that the dielectric properties depend non-monotonically on the frequency of the externally applied electric field. Afterwards, the hydrodynamic interactions of dispersed nanocolloids are analyzed. Similar to the observation made for the previous system, the study shows that physical processes on different but overlapping time scales induce significant memory effects in the system. The movement of a nanocolloid in dispersion, e.g., generates fluid vortices that affect its own dynamics and the movement of other nearby nanocolloids at later times. These memory effects can be described with a generalized Langevin equation by including frequency-dependent friction kernels and time-correlated stochastic forces.

To utilize these insights for dynamic coarse-graining, we develop two novel methods: the "iterative memory reconstruction" to systematically determine memory kernels from microscopic systems, and the "generalized Brownian dynamics" technique to integrate the generalized Langevin equation. The combination of these tools enables the construction of a non-Markovian coarse-grained model for the dispersed nanocolloids that perfectly reproduces the dynamics of the underlying microscopic system. The distinct feature of this model is that it not only includes the hydrodynamic self-diffusion of the colloids but it also incorporates the correct frequency-dependent pair-correlations between different particles. Additionally, we can show that the time-integration of this transferable coarse-grained model is roughly 10^4 times faster than the original molecular dynamics simulations.

Meinen Großeltern gewidmet.

"Das erste, das der Mensch im Leben vorfindet, das letzte, wonach er die Hand ausstreckt, das kostbarste, was er im Leben besitzt, ist die Familie."

Adolph Kolping

Contents

i

1

Introduction

The field of soft condensed matter includes the study of liquids, polymers and colloids. All these systems have in common that their dynamics is governed by physical processes on very different length and time scales. Brownian motion is a characteristic example of this feature. It describes the dynamics of colloids or macroscopic particles in dispersion. While the microscopic dynamics of the fluid particles happen on time scales of picoseconds, the diffusion time of the colloid is between nanoseconds and seconds, depending on the size of the dispersed particle. Bridging the gap between these scales is a major challenge when studying Brownian motion or other soft matter phenomena with computer simulations. The method used to approach this problem is called *coarse-graining*.

Coarse-graining describes the process of reducing the number of degrees of freedom of a system. In the example of Brownian motion, the positions of the colloids are relevant and not the detailed configurations of the fluid particles. This suggests the use of an effective model with the colloid positions as the coarse-grained variables and replace the solvent particles by effective equations of motion. Such a model is called *implicit solvent model* and is widely used in soft matter physics. In most implicit solvent models, the fluid is replaced by effective potentials that restore the correct structural properties of the coarse-grained variables. This process, however, often changes the dynamical properties of the system significantly. In colloidal systems, for example, the movement of a colloid induces a fluid flow which indirectly affects its own dynamics and that of other colloids. This long-range interaction is called *hydrodynamic interaction* and it crucially influences various physical processes in soft matter science, including Brownian motion. To construct coarse-grained models with meaningful dynamics, it is therefore necessary to go beyond mere static pair-potentials.

Various techniques have been proposed in the literature to preserve the correct dynamical properties in a coarse-grained model. Basically, they can be divided into two fundamentally different approaches. The first approach is to introduce pseudo particles that interact with the coarse-grained variables and thus restore the hydrodynamic interactions. Examples are smoothed particle hydrodynamics (SPH), dissipative particle dynamics (DPD), lattice Boltzmann (LB) or multi particle collision dynamics (MPCD). In the second approach, the equations of motion of the coarse-grained particles are manipulated in such a way that the important

dynamical properties of the underlying system are restored. This class includes techniques like Stokesian dynamics or Brownian dynamics (BD). These approaches have the advantage of being computationally efficient, since the number of degrees of freedom is small. However, they are based on the assumption of time scale separation. This means it is assumed that the dynamics of the fluid particles are much faster than the dynamics of the coarse-grained variables. This is a reasonable assumption for colloidal dispersions with micrometer-sized colloids, however it is questionable for smaller colloids, proteins or polymers. In general, coarse-graining *frequency-dependent phenomena* is difficult, since the dynamics strongly depend on the interplay between different time scales and a separation cannot be assumed. In this case, it is necessary to consider coarse-grained equations of motion with non-Markovian time-dependent interactions. Such a coarse-grained model can be constructed on the basis of the Mori-Zwanzig formalism.

The Mori-Zwanzig formalism was introduced in the 1950s by Robert Zwanzig and Hajime Mori to understand the principles of systematic coarse-graining theoretically. Their formalism applies projection operators to divide the whole set of dynamical variables into relevant, coarse-grained, variables and irrelevant variables. For Brownian motion, for example, the relevant variables would be the positions and momenta of the colloids and the irrelevant variables would be the fluid particles. The result of the Mori-Zwanzig formalism is a non-Markovian stochastic differential equation called "generalized Langevin equation" (GLE). The GLE includes frequency-dependent friction functions, called memory kernels, to model the frequency-dependent dynamical properties of the underlying system. Although this formalism has been known since 60 years, only in recent years people started to use it as a framework to construct coarse-grained models. However, most of the proposed techniques are restricted to one or two particles and cannot be used to construct realistic models of soft matter systems. The reasons for this lack of suitable methods are first, the difficulties in the numerical integration of the GLE in many-body systems, and second, the efficient determination of transferable memory kernels from first principles.

The aim of this thesis is to approach the two problems stated above. For this purpose two methods have been developed: the "iterative reconstruction of memory kernels" and "generalized Brownian dynamics" techniques. It will be shown that this toolkit is very versatile and allows for a general and transferable coarse-graining procedure. This thesis thus combines the best of both worlds: Computational efficiency as well as correct dynamics even when a complete separation of time scales cannot be assumed. To show the range of possible applications of these methods, two model systems will be presented which are governed by frequency-dependent phenomena. The first system is a polyelectrolyte in ionic solution driven by an AC electric field. The polarizability of the polyelectrolyte strongly depends on the dynamical properties of the system and the frequency of the external field. The second system is a nanocolloid dispersion. The overlapping of fluid and colloid relaxation times

leads to strong memory effects in the hydrodynamic interactions. The latter system will be chosen for a first application of the proposed coarse-graining techniques.

The first part of this thesis is a general literature review of frequency-dependent phenomena in dispersions. Chapter 2 gives an introduction to rheology and fluid dynamics. These basics are then used to describe the frequency-dependent hydrodynamic interactions between colloids in Chapter 3. In Chapter 4, polyelectrolytes in ionic solution are discussed. This includes a presentation of the electrokinetic equations that can be used to describe the frequency-dependent polarizability of polyelectrolytes. Afterwards, the principles of static and dynamic coarse-graining are explained in Chapter 5. In Chapter 6, the relevant simulation methods are introduced: DPD, non-Markovian DPD and the ConDiff algorithm.

In the second part, the frequency-dependent polarizability of polyelectrolytes is investigated. So far, all simulation studies assumed stiff, rod-like particles as models for the polyelectrolytes. However, this assumption is questionable, especially for the application to proteins or DNA, since their chain length is much larger than their persistence length. Therefore, the effect of solvent quality on the polarizability of flexible polyelectrolytes is analyzed in the present work. First, the coarse-grained simulation model for the polyelectrolyte in ionic suspension is described in Chapter 7. Afterwards, it will be shown in Chapter 8 that the polarizability depends non-monotonically on the frequency of the applied AC electric field. In Chapter 9, the main results for the dependence of the polarizability on chain length and solvent quality are reported. Chapter 10 summarizes and concludes this part.

The third and main part of this thesis presents the newly developed "iterative reconstruction of memory kernels" and "generalized Brownian dynamics" techniques, applied to nanocolloid dispersions. To derive theoretical memory kernels that describe hydrodynamic interactions between the colloids, the transport coefficients of the dispersion medium have to be determined. Chapter 11 therefore discusses generalized Green-Kubo relations to determine the shear and bulk viscosity of complex fluids. In Chapter 12, the iterative reconstruction of memory kernels from simulation data is presented. With this technique, the theoretically derived memory kernel can be compared to results from molecular dynamics simulations. Afterwards, the "generalized Brownian dynamics" algorithm is introduced in Chapter 13. Applying the proposed methods, the frequency-dependent hydrodynamic interactions between nanocolloids can be analyzed in-depth in Chapter 14. This chapter also includes an investigation of the efficiency and transferability of the constructed non-Markovian coarse-grained models. In Chapter 15, conclusions are drawn and an outlook for future work is given.

Part I

Frequency-Dependent Phenomena in Dispersions

<div align="right">

2

</div>

Fluid Dynamics

Fluid dynamics is the study of flows in gases or liquids. Historically, scientists wanted to understand the fundamental properties of moving liquids which led to discoveries like Bernoulli's principle. In the 19th century advances in mathematics finally enabled the derivation of the basic equations that govern the dynamics of liquids and it was observed that these equations are based on only a few important principles.[1;2] Today, fluid dynamics is a huge field of research including topics like aerodynamics that have many important applications, e.g., in the automobile industry (see Figure 2.1).

The main principle behind fluid dynamics is the *continuum hypothesis*, stating that the fluid is described by effective, hydrodynamic fields instead of single particles. This assumption is justified if the mean free path λ_{f} of the fluid is much smaller than the relevant length scales in the system (e.g. the size of an immersed particle) and if the mean collision time τ_{c} is much shorter than the relevant time scales. However, it has been observed that the description of fluids in terms of hydrodynamic fields is still applicable on very small length and time scales, even if the above conditions are not strictly fulfilled.[5] The analysis that will be presented in Chapter 14 of this thesis is an example for this observation.

The hydrodynamic fields that are most commonly used for fluid dynamics are the particle density $\rho(\boldsymbol{r}, t)$, the velocity field $\boldsymbol{u}(\boldsymbol{r}, t)$, and the energy density $e(\boldsymbol{r}, t)$, which are all related to macroscopically conserved quantities. To derive the equations of
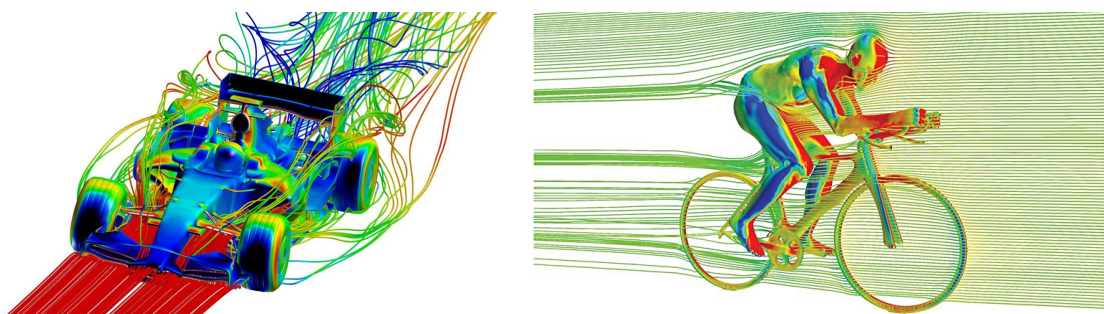

Figure 2.1: Aerodynamic analysis of a race car and a cyclist. Small changes in the shape of the object can lead to significant turbulences which make an optimization of air drag inevitable for the construction of fast moving vehicles. Pictures taken from Ref. 3 (left) and Ref. 4 (right).

motion for these hydrodynamic fields, it is necessary to utilize two fundamental relations: the *conservation laws* and the *constitutive relations*. The conservation laws are based on the aforementioned relation between hydrodynamic fields and conserved macroscopic quantities. For example, it is assumed that the total mass M of the fluid is conserved. Therefore, the particle density $\rho(\boldsymbol{r}, t)$ in an arbitrary volume can only change in time if a flow of particles out of this volume emerges. Similarly, the total linear momentum P, and the total energy E are conserved. Consequentially, three fundamental conservation laws can be derived,

$$\frac{\partial}{\partial t}\rho(\boldsymbol{r}, t) + \nabla \cdot \boldsymbol{J_\rho}(\boldsymbol{r}, t) = 0, \quad \boldsymbol{J_\rho}(\boldsymbol{r}, t) = \rho(\boldsymbol{r}, t)\boldsymbol{u}(\boldsymbol{r}, t), \tag{2.1}$$

$$\frac{\partial}{\partial t}\boldsymbol{J_\rho}(\boldsymbol{r}, t) + \nabla \cdot \boldsymbol{\Pi}(\boldsymbol{r}, t) = 0, \quad \Pi_{ij} = \rho(\boldsymbol{r}, t)u_i(\boldsymbol{r}, t)u_j(\boldsymbol{r}, t) + \sigma_{ij}(\boldsymbol{r}, t),$$

$$\frac{\partial}{\partial t}e(\boldsymbol{r}, t) + \nabla \cdot \boldsymbol{J_e}(\boldsymbol{r}, t) = 0, \quad \boldsymbol{J_e}(\boldsymbol{r}, t) = (e(\boldsymbol{r}, t) + p(\boldsymbol{r}, t))\boldsymbol{u}(\boldsymbol{r}, t) + \boldsymbol{J'_e}(\boldsymbol{r}, t),$$

with particle flux $\boldsymbol{J_\rho}(\boldsymbol{r}, t)$, momentum flux tensor $\boldsymbol{\Pi}(\boldsymbol{r}, t)$, and energy flux $\boldsymbol{J_e}(\boldsymbol{r}, t)$. To close these equations, it is necessary to find explicit expressions for the dissipative stress tensor $\boldsymbol{\sigma}(\boldsymbol{r}, t)$ and the dissipative energy flux $\boldsymbol{J'_e}(\boldsymbol{r}, t)$. These dissipative currents depend on the microscopic interactions of the fluid particles and are thus important for modeling distinct fluids. The equations for these currents are called constitutive relations. In this thesis we investigate isotropic, compressible Newtonian fluids. Under these assumptions, the constitutive relations are[2]

$$\sigma_{ij}(\boldsymbol{r}, t) = p(\boldsymbol{r}, t)\delta_{ij} + \left(\frac{2}{3}\eta - \zeta\right)\nabla \cdot \boldsymbol{u}(\boldsymbol{r}, t)\delta_{ij} - \eta\left(\partial_i u_j + \partial_j u_i\right), \tag{2.2}$$

$$\boldsymbol{J'_e}(\boldsymbol{r}, t) = \boldsymbol{u}(\boldsymbol{r}, t) \cdot \boldsymbol{\sigma}(\boldsymbol{r}, t) - \lambda\nabla T(\boldsymbol{r}, t), \tag{2.3}$$

with thermodynamic pressure $p(\boldsymbol{r}, t)$, shear viscosity η, bulk viscosity ζ, heat conductivity λ and temperature $T(\boldsymbol{r}, t)$.

By combining these relations, the Navier-Stokes equations can be derived. However, solving these equations is very complicated, especially due to their non-linearity. Finding general solutions of the Navier-Stokes equations for arbitrary initial conditions is in fact one of the Millennium Price Problems.[6] In the following, we will be using a simplified version: the linearized Navier-Stokes equations. These equations are a suitable approximation of the Navier-Stokes equations if the velocities in the system are small and a non-turbulent flow can be assumed. For the system investigated in the present work, this assumption is well justified. The linearized Navier-Stokes equations read as follows,

$$\rho_e\frac{\partial}{\partial t}\boldsymbol{u}(\boldsymbol{r}, t) = -\nabla\boldsymbol{\sigma}(\boldsymbol{r}, t) + \boldsymbol{F}_1^{(1)}(\boldsymbol{r}, t),$$

$$\frac{\partial}{\partial t}\rho(\boldsymbol{r}, t) = -\rho_e\nabla \cdot \boldsymbol{u}(\boldsymbol{r}, t), \tag{2.4}$$

with uniform equilibrium density of the fluid ρ_e, external force density $\boldsymbol{F}_1^{(1)}(\boldsymbol{r}, t)$, $\nabla p(\boldsymbol{r}, t) = c_0^2\nabla\rho(\boldsymbol{r}, t)$, and the speed of sound c_0. To solve the linearized Navier-

Stokes equations analytically, we determine the Fourier transform of velocity field,

$$\hat{\boldsymbol{u}}(\boldsymbol{r},\omega) = \int_{-\infty}^{\infty} e^{\mathrm{i}\omega t} \boldsymbol{u}(\boldsymbol{r},t), \tag{2.5}$$

particle density $\hat{\rho}(\boldsymbol{r},\omega)$ and external force density $\hat{\boldsymbol{F}}_1^{(1)}(\boldsymbol{r},\omega)$. In Fourier space, the linearized Navier-Stokes equations transform to[7]

$$(-\mathrm{i}\omega\rho_e - \eta\Delta)\hat{\boldsymbol{u}}(\boldsymbol{r},\omega) = -\mu\nabla\hat{\rho}(\boldsymbol{r},\omega) + \hat{\boldsymbol{F}}_1^{(1)}(\boldsymbol{r},\omega), \tag{2.6}$$

$$(-\omega^2\rho_e - c^2\Delta)\hat{\rho}(\boldsymbol{r},\omega) = -\nabla\cdot\hat{\boldsymbol{F}}_1^{(1)}(\boldsymbol{r},\omega). \tag{2.7}$$

Here, we have introduced the parameter $\mu(\omega)$ and the frequency-dependent speed of sound $c(\omega)$,

$$\mu(\omega) = c_0^2 - \mathrm{i}\omega\left(\frac{1}{3}\eta + \zeta\right)\rho_e^{-1}, \tag{2.8}$$

$$c(\omega)^2 = c_0^2 - \mathrm{i}\omega\left(\frac{4}{3}\eta + \zeta\right)\rho_e^{-1}, \tag{2.9}$$

with $\mathrm{Im}(c) > 0$. Equations (2.6) and (2.7) can be solved using the Green's function formalism.[8] The final result for the Fourier transform of the velocity field $\hat{\boldsymbol{u}}(\boldsymbol{r},\omega)$ induced by an external force density $\boldsymbol{F}_1^{(1)}(\boldsymbol{r},\omega)$ published by Mazur *et al.*[7] is

$$\hat{\boldsymbol{u}}(\boldsymbol{r},\omega) = \int \mathrm{d}\boldsymbol{r}'\Big(G_{\mathrm{tr}}(\boldsymbol{r}-\boldsymbol{r}',\omega) + \alpha^{-2}\frac{\partial}{\partial\boldsymbol{r}'}\frac{\partial}{\partial\boldsymbol{r}'} \tag{2.10}$$

$$\times \left[\eta^{-1}c^2 G_{\mathrm{l}}(\boldsymbol{r}-\boldsymbol{r}',\omega) - G_{\mathrm{tr}}(\boldsymbol{r}-\boldsymbol{r}',\omega)\right]\Big)\cdot\boldsymbol{F}_1^{(1)}(\boldsymbol{r}',\omega),$$

with longitudinal and transversal Green's functions,

$$G_{\mathrm{tr}}(\boldsymbol{r},\omega) = (4\pi\eta r)^{-1}e^{-\alpha(\omega)r}, \tag{2.11}$$

$$G_{\mathrm{l}}(\boldsymbol{r},\omega) = (4\pi c(\omega)^2 r)^{-1}e^{-\mathrm{i}\omega r/c(\omega)}, \tag{2.12}$$

distance $r = |\boldsymbol{r}|$, and $\alpha(\omega) = (-\mathrm{i}\omega\rho_e/\eta)^{\frac{1}{2}}$, $\mathrm{Re}(\alpha) > 0$. The origin of the force density $\boldsymbol{F}_1^{(1)}(\boldsymbol{r},\omega)$ can, for example, be the movement of a colloid immersed in the fluid. The induced velocity field $\hat{\boldsymbol{u}}(\boldsymbol{r},\omega)$ then affects the movement of other colloids and thus mediates hydrodynamic interactions between colloids. In Chapter 3 we will utilize the equations presented in this section to derive theoretical predictions for these hydrodynamic interactions.

To describe a certain Newtonian fluid, it is necessary to determine the transport coefficients of the fluid, namely the shear viscosity η and the bulk viscosity ζ.

2.1   Transport coefficients and rheology

The shear viscosity η is a measure for the resistance of the fluid against *deformation of shape*. It thus determines how much energy is dissipated in the fluid if layers of different flow velocities emerge. Therefore, it is an important quantity to describe flows in the fluid close to boundaries or immersed particles. Additionally, it describes the propagation of the transversal shear waves (see Eq. (2.11)). Contrarily, the bulk viscosity ζ is related to the movement and damping of longitudinal sound waves (see Eq. (2.12)). It is thus a measure for the resistance of the fluid against *deformation of volume*. In many studies, the bulk viscosity is neglected due to incompressibility of the fluid. However, on small time scales, the propagation of sound waves does matter, even in liquids that are generally assumed to be approximately incompressible (see also Chapters 3 and 14).

In computer simulations two fundamentally different approaches exist to determine these transport coefficients. The first one is creating a non-equilibrium state by externally inducing a flow and calculating the transport coefficients by direct measurements (e.g., the flow velocity or the dissipative stress tensor). These methods are generally referred to as non-equilibrium molecular dynamics (NEMD) methods.[9–13] The other option is to evaluate equilibrium fluctuations and use the well-known Green-Kubo[14;15] or Einstein-Helfand relations.[16] In the main part of this thesis we will discuss the second option in detail, for NEMD we refer to Attachment B and Ref. 17.

The standard Green-Kubo formulas for the shear viscosity η and the bulk viscosity ζ used in the literature are

$$\eta = \frac{V}{k_{\mathrm{B}}T} \int_0^\infty dt \, \langle \sigma_{xz}(0)\sigma_{xz}(t) \rangle_0 \,, \tag{2.13}$$

$$\zeta = \frac{V}{k_{\mathrm{B}}T} \int_0^\infty dt \, \langle I_\zeta(0)I_\zeta(t) \rangle_0 \,, \tag{2.14}$$

where $\sigma_{xz}(t)$ are the off-diagonal components of the volume-averaged dissipative stress tensor, and

$$I_\zeta(t) = \frac{1}{3}\sum_\alpha \left[\sigma_{\alpha\alpha}(t) - \langle\sigma_{\alpha\alpha}\rangle_0 \right], \tag{2.15}$$

with the diagonal-components $\sigma_{\alpha\alpha}(t)$ of the dissipative stress tensor and the time-average $\langle ... \rangle_0$. These equations were derived by Green[14] and Kubo[15] and have found a huge variety of applications (see, e.g., Refs. 18–20). To derive the Green-Kubo relations, it is necessary to understand the coarse-graining procedure from a microscopic system of particles i at positions $\boldsymbol{r}_i$ with velocities $\boldsymbol{v}_i$ to an effective system described by the hydrodynamic fields, $\rho(\boldsymbol{r},t)$, $\boldsymbol{u}(\boldsymbol{r},t)$, and $e(\boldsymbol{r},t)$. For this coarse-graining procedure, the Mori-Zwanzig projection operator formalism can be

utilized (for details see Section 5.2). This formalism defines projection operators to project from the full space of dynamical variables (which are the trajectories of the particles) onto a subspace that is given by the dynamics of the hydrodynamic fields. In this way it can be shown that the Fourier transform of the transverse particle flux $\boldsymbol{J}_\rho^\perp(\boldsymbol{r}, t)$ follows the non-Markovian evolution equation[21;22]

$$\lim_{k\to 0} \frac{\mathrm{d}}{\mathrm{d}t} J_{\rho,z}^\perp(k_x, t) = \frac{-k_x^2}{3Nk_\mathrm{B}T} \int_0^t \mathrm{d}s \, \langle \sigma_{xz}(k_x, s)\sigma_{xz}(-k_x, 0)\rangle_0 \, J_{\rho,z}^\perp(k_x, t-s) + ik_x\sigma_{xz}(k_x, t),$$

$$(2.16)$$

with wavevector $\boldsymbol{k}$ and the Fourier transforms,

$$J_{\rho,z}^\perp(k_x, t) = \int \mathrm{d}x J_{\rho,z}^\perp(x, t)e^{ik_x x}, \tag{2.17}$$

$$\sigma_{xz}(k_x, t) = \int \mathrm{d}x \sigma_{xz}(x, t)e^{ik_x x}. \tag{2.18}$$

For simplicity, we have defined the coordinate system such that $\boldsymbol{k} = k_x\boldsymbol{e}_x$ and the transverse particle flux in z-direction, obviously related equations can be derived for $J_{\rho,z}^\perp(k_y, t)$ and $J_{\rho,y}^\perp(k_x, t)$. The conservation laws introduced in this chapter indicate that the left-hand side of Eq. (2.16) corresponds to a momentum flux Π_{xz} in the fluid,

$$\lim_{k\to 0} \frac{\mathrm{d}}{\mathrm{d}t} J_{\rho,z}^\perp(k_x, t) = ik\Pi_{xz}. \tag{2.19}$$

Similarly, the transverse particle flux $J_{\rho,z}^\perp(k_x, t)$ is related to the strain rate,

$$\dot{\gamma}_{xz} = -\frac{ikJ_{\rho,z}^\perp(k_x, t)}{\rho}. \tag{2.20}$$

Eq. (2.16) therefore corresponds to a constitutive relation, $\Pi_{xz} = -\eta\dot{\gamma}_{xz}$. This indicates that the term $\langle \sigma_{xz}(k_x, t)\sigma_{xz}(-k_x, 0)\rangle_0$ is connected to the shear viscosity η and indeed, the Green-Kubo relations can be derived with this formalism. An extended and complete derivation can be found in the article by Ernst *et al.*[21] and in Ref. 22.

For the application of the Mori-Zwanzig formalism it is necessary that the time evolution of the system is defined by a Hermitian Liouville operator $\mathcal{L}$. This also requires the forces to be *invariant under time reversal symmetry*.[23] For dissipative, velocity-dependent forces that are used in many simulation techniques (see, e.g., Section 6.1) the symmetry is, however, broken, since the velocity changes the sign under time inversion. In Chapter 11 we will therefore introduce a generalized Green-Kubo relation that can be applied to fluids with dissipative and stochastic forces.

3

Colloids and Hydrodynamic Interactions

Colloidal systems play an important role in physics, chemistry and medicine. In physics, they are often used as a model for atomic systems, for example to study nucleation,[25] crystallization[26;27] or melting phenomena.[28;29] The big advantage over atomistic systems is the huge amplification of relevant length and time scales. This allows the investigation of colloidal systems with visible light on time scales of the order of milliseconds making single-particle tracking possible (see Fig. 3.1). Additionally, colloids are subject to Brownian motion which makes them an interesting model system in the field of statistical physics. In chemistry, the synthesis and characterization of colloids is studied extensively, in particular because of their applications in inks, emulsions or composite materials. Recently, colloids also received
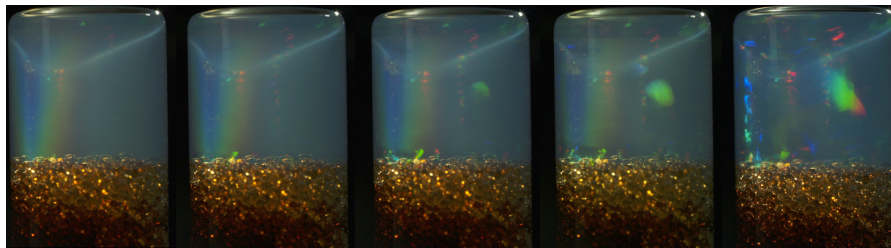
(a) The nucleation and growth of colloidal crystals induces bragg reflections in the visible spectrum. The time between two photographs is 3 min.
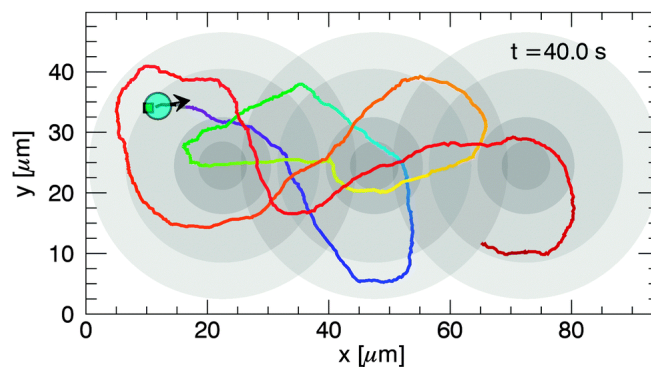
(b) Single-particle tracking of an active colloidal Janus particle under the influence of three point traps. Picture taken from Ref. 24.

Figure 3.1: Examples for experiments with colloids that are possible due to the huge amplification of length and time scales of colloidal dispersions compared to atomistic systems.

an increasing amount of attentions in the field of nanomedicine. New technologies, for example, could allow for the embedding of genetic material in nanoparticles and thus the controlled manipulation of genetically modified cells.[30]

The category "colloid" includes particles of very different length scale, type and surface structure. The length scales range from nanometers to micrometers, leading to completely different static and dynamical properties (see also Tab. 3.1). Colloids can have a significant surface charge and therefore a strong polarizability, which can for example be utilized to grow two-dimensional crystals.[31] In recent years active colloids have been investigated extensively to model dynamic phase separation and swarming behavior.[32;33] The surface of colloids can be very smooth, leading to nearly perfect hard-core interactions, which makes it possible to perform experiments with hard spheres[29;34] and testing several theories known from statistical mechanics[35] and simulations.[36;37] But various studies have also been performed with thermo-responsive polymer-coated colloids, leading to temperature-dependent short-range attraction between the colloids. This allows the investigation of reversible colloid aggregation and absorption.[38;39]

The focus of this thesis is on an important dynamical feature of colloidal dispersions, viz. their hydrodynamic interactions. The movement of colloids in a fluid induces a disturbance of the velocity field that affects the movement of themselves and of other colloids. Therefore, hydrodynamic interactions strongly depend on the interplay of colloid and fluid dynamics. The relevant time scales for colloid ($R_c \approx 100\,\mathrm{nm}$) and nanocolloid ($R_c \approx 1\,\mathrm{nm}$) dynamics in water are presented in Tab. 3.1. For the large colloids the compressibility of the fluid does not play an important role, since sound waves are propagated on time scales much smaller than the Brownian relaxation time. This picture completely changes when considering nanocolloids. Now, three different time scales overlap, which leads to significant memory effects in the dynamics. The best known memory effect is hydrodynamic backflow, which is a consequence of the non-Markovian self-interaction of colloids in dispersion. The origin of hydrodynamic backflow are fluid vortices, which are induced by the movement of a colloid and interact with it at later times. The long-time tail in the velocity auto-correlation function observed by Alder *et al.*[40] is one important consequence of this hydrodynamic self-interaction (see Section 5.3). The pair-interactions of nanocolloids are also governed by memory effects. The theoretical and simulation analysis of these pair-memory effects were part of my master thesis[a] and published in Ref. 5. The main results of this work will be shortly recapitulated on the following three pages.

Using the solution of the linearized Navier-Stokes equations, derived in Chapter 2, allows to derive the velocity field $\hat{\boldsymbol{u}}(\boldsymbol{r}, \omega)$ created by a point force $\hat{\boldsymbol{F}}_1^{(1)}(\boldsymbol{r}, \omega) =$

---

[a]My cumulative master thesis was written as part of the Fast-Track program of the Department of Physics at the University of Mainz. Therefore, the work presented in this paper was done in summer 2017, parallel to the research presented in this PhD thesis.

	Time scale	Colloid	Nanocolloid
Sonic time	$\tau_s = R_c/c_0$	10^{-10} s	10^{-12} s
Kinematic time	$\tau_v = \rho R_c^2/\eta$	10^{-8} s	10^{-12} s
Brownian relaxation time	$\tau_B = \rho R_c^2/\eta$	10^{-8} s	10^{-12} s
Colloid diffusion time	$\tau_d = \eta R_c^3/k_B T$	10^{-3} s	10^{-9} s

Table 3.1: Different time scales that are relevant in colloidal dispersions. The time scales of colloids ($R_c \approx 100$ nm) are compared to nanocolloids ($R_c \approx 1$ nm). The parameters in SI units are derived in Appendix A. Table adapted from Ref. 5.

$\hat{\boldsymbol{F}}_1^{(1)}(\omega)\delta(\boldsymbol{r})$ acting on the center of particle 1,

$$\hat{\boldsymbol{u}}(\boldsymbol{r},\omega) = -\frac{1}{8\pi\eta}\left[A(\boldsymbol{r},\omega)\hat{\boldsymbol{F}}_1^{(1)}(\omega) + B(\boldsymbol{r},\omega)(\hat{\boldsymbol{F}}_1^{(1)}(\omega)\cdot\boldsymbol{n})\boldsymbol{n}\right], \tag{3.1}$$

with $\boldsymbol{n} = \boldsymbol{r}/|\boldsymbol{r}|$. The interaction parameters $A(\boldsymbol{r},\omega)$ and $B(\boldsymbol{r},\omega)$ depend on the longitudinal and transversal modes of the fluid,

$$A(\mathbf{r},\omega) = A_l(\mathbf{r},\omega) + A_{tr}(\mathbf{r},\omega), \tag{3.2}$$

$$B(\mathbf{r},\omega) = B_l(\mathbf{r},\omega) + B_{tr}(\mathbf{r},\omega), \tag{3.3}$$

$$A_l(\mathbf{r},\omega) = -\left(\frac{2i\omega}{r^2\alpha^2 c} + \frac{2}{r^3\alpha^2}\right)e^{-i\omega r/c}, \tag{3.4}$$

$$A_{tr}(\mathbf{r},\omega) = \left(\frac{2}{r} + \frac{2}{\alpha r^2} + \frac{2}{\alpha^2 r^3}\right)e^{-\alpha r}, \tag{3.5}$$

$$B_l(\mathbf{r},\omega) = \left(-\frac{\omega^2}{c^2}\frac{2}{\alpha^2 r} + \frac{6i\omega}{r^2\alpha^2 c} + \frac{6}{r^3\alpha^2}\right)e^{-i\omega r/c}, \tag{3.6}$$

$$B_{tr}(\mathbf{r},\omega) = -\left(\frac{2}{r} + \frac{6}{\alpha r^2} + \frac{6}{\alpha^2 r^3}\right)e^{-\alpha r}. \tag{3.7}$$

The velocity field created by the movement of the colloids can now be decomposed into basic velocity fields described by Eq. (3.1). This decomposition is possible due to the linearity of the underlying equations. [41–43] In the method of reflections the velocity field created by particle 1 induces the friction force $\hat{\mathbf{F}}_2^{(1)}(\omega) = -\hat{\gamma}(\omega)(\hat{\mathbf{v}}_2 - \hat{\mathbf{u}}(\mathbf{r},\omega))$ on particle 2. Here, $\hat{\gamma}(\omega)$ denotes the frequency-dependent friction of a solitary sphere in a flow $\hat{\boldsymbol{u}}(\boldsymbol{r},\omega)$. Additionally, the velocity field is reflected and applies a similar force on particle 1. With every reflection, the amplitude of the velocity field is reduced and the sum of forces describes the hydrodynamic interactions between the colloids.

The final result for the force $\hat{\boldsymbol{F}}_1(R,\omega)$ on particle 1 induced by the velocities $\hat{\boldsymbol{v}}_1(\omega)$ and $\hat{\boldsymbol{v}}_2(\omega)$ of particles 1 and 2, respectively, can be expressed as

$$\hat{F}_{1,\|}(R,\omega) = -\hat{\gamma}_{11,\|}(R,\omega)\hat{v}_{1,\|}(\omega) - \hat{\gamma}_{12,\|}(R,\omega)\hat{v}_{2,\|}(\omega), \tag{3.8}$$

with colloid distance $R = |\boldsymbol{R}_{12}|$. The subscript ($\|$) stands for the contributions parallel to the line-of-centers $\boldsymbol{R}_{12}$ between particles 1 and 2. Similar equations can

be derived for the perpendicular direction ($\perp$). The frequency-dependent self- and pair-memory kernels are given by

$$\hat{\gamma}_{11,\parallel}(R,\omega) = \frac{\hat{\gamma}(\omega)}{1 - D_{\parallel}(R,\omega)^2}, \tag{3.9}$$

$$\hat{\gamma}_{12,\parallel}(R,\omega) = -\frac{\hat{\gamma}(\omega)D_{\parallel}(R,\omega)}{1 - D_{\parallel}(R,\omega)^2}, \tag{3.10}$$

and the interaction functions are defined as

$$D_{\parallel}(R,\omega) = \frac{\hat{\gamma}(\omega)}{8\pi\eta}\left(A(R,\omega) + B(R,\omega)\right), \tag{3.11}$$

$$D_{\perp}(R,\omega) = \frac{\hat{\gamma}(\omega)}{8\pi\eta}A(R,\omega). \tag{3.12}$$

This result is valid for small radius to distance ratios R_{c}/R. It can be further improved, by considering appropriate boundary conditions for the velocity at the surface of the sphere (see Refs. 5; 43 for details). Our theoretical results refer to this
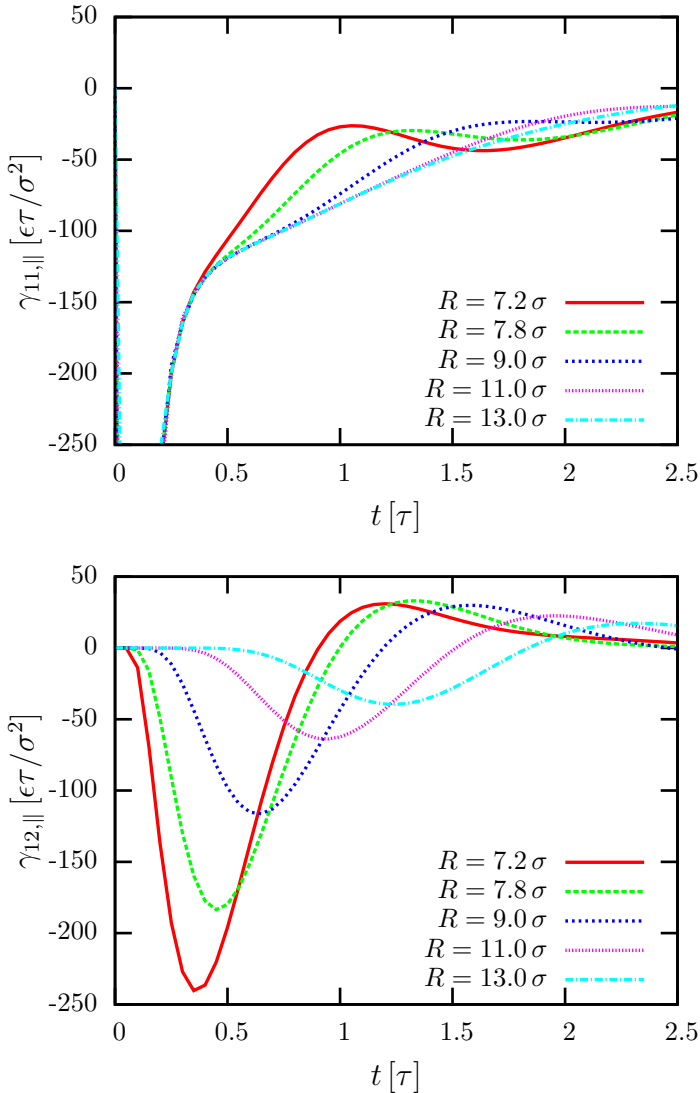

Figure 3.2: Time-dependence of the hydrodynamic memory kernels for different colloid distances R. The input parameters roughly correspond to a nanocolloid ($R_{\mathrm{c}} \approx 1\,\mathrm{nm}$) in water (see Appendix A). The upper panel shows the self-memory kernel and the lower panel the pair-memory kernel. Figure adapted from Ref. 5.

16

quantitatively improved theory, however, qualitatively the results do not change significantly.

Figure 3.2 illustrates the Fourier transform of the frequency-dependent memory kernels describing the hydrodynamic interaction of nanocolloids. The response function of the solitray sphere, $\hat{\gamma}(\omega)$, in a compressible fluid was derived by Mazur *et al.*[7] The input parameters that are chosen to evaluate the results from fluid dynamics are equivalent to the ones of the nanocolloid dispersion which is studied in this thesis (see Chapter 5 and Tab. 5.2). The upper panel of Figure 3.2 shows the self-interaction of the colloids. The curves visualize hydrodynamic backflow, which becomes apparent through the negative values in the self-memory kernel. It can be observed that nearby colloids have a significant influence on the self-diffusion of a nanocolloid in dispersion. It should be mentioned that the values for $t < 0.25\,\tau$ are not comparable to computer simulations or experiments, since the particle-character of the fluid molecules significantly influences the dissipative force on the nanocolloids on small time scales. These high-frequency interactions cannot be modeled within the fluid dynamics framework because of the continuum hypothesis (see Chapter 2). The lower panel of Figure 3.2 visualizes the pair-interactions of the nanocolloids *via* sound waves that are induced by the motion of the colloids. This can for example be shown by calculating the propagation velocities of these waves, and proving that they are equivalent to the speed of sound c_0 in the fluid. As a major result of my master thesis it could be shown that on this scale the hydrodynamic pair-interaction is actually dominated by sound waves.

In this thesis we will go further and establish a coarse-graining procedure that is able to construct effective models which precisely reproduce the presented results. This will be the topic of Part III.

4

Polyelectrolytes and Electric Polarizability

Understanding the physical behavior of polyelectrolytes became increasingly important since proteins and DNA were brought into the focus of biology and biotechnology. For example, one of the key elements of a supervised gene transfer is a controlled separation, manipulation and navigation of DNA molecules. Dielectrophoresis is one possibility to achieve the former, however, it strongly depends on the dielectric properties of the DNA.[44;45] Therefore, it is of large interest to investigate dielectric properties of polyelectrolytes and understand the conformation- and frequency-dependence of the electric polarizability.

Polyelectrolytes in ionic solution are characterized by many different relevant length and time scales. The length scales, for example, range from the diameters of the solute particles and ions over the size of the electric double layer around the polyelectrolyte to the radius of gyration of the polyelectrolytes. The interplay of these different scales complicates the modeling of polyelectrolytes in ionic solution and makes it difficult to derive theoretical predictions for the electric polarizability. To give an insight into the system, we will therefore first discuss the dynamics and dielectric properties of charged colloids.[46–49]

It is well known that charged colloids in ionic solution are surrounded by an electric double layer (see Figure 4.1). The thickness of the double layer is given by the Debye screening length,

$$\lambda_{\mathrm{D}} = \left[4\pi\lambda_{\mathrm{B}} \sum_i z_i^2 c_i^0 \right]^{-\frac{1}{2}}. \tag{4.1}$$

Here, $\lambda_{\mathrm{B}} = e^2/(4\pi\epsilon_m k_{\mathrm{B}} T)$ is the Bjerrum length ($\lambda_{\mathrm{B}} \approx 0.7\,\mathrm{nm}$ in water), z_i and c_i^0 the valency and bulk concentration of ion species i, respectively, and ϵ_m the medium permittivity. The properties of the electric double layer can be well described within the Poisson-Boltzmann theory since dynamical effects do not play a role.

However, the situation gets more complicated if an external electric field drives the system out of equilibrium. Now, the interplay of ion and colloid mobilities strongly effects the dynamics of the system. In fact, the mobility of the ions is not constant,
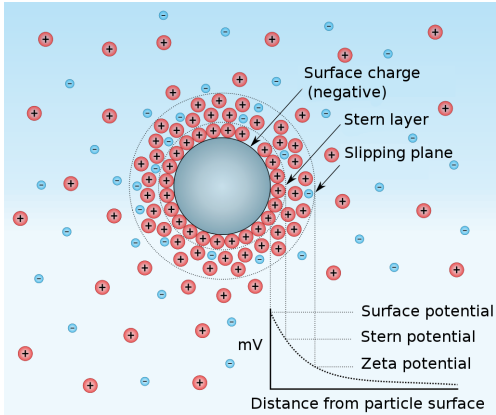
Figure 4.1: Sketch of the electric double layer that surrounds a charged colloid in ionic solution. The Stern layer includes condensed counterions and the slipping plane uncondensed ions with high mobility. Due to the aggregation of counterions around the colloid, its charge is effectively screened. Figure adapted from Ref. 50.

but depends on the distance of the ions to the colloid surface.[49;51] Therefore, the different constituents of the electric double layer will react very differently to the external field. To describe this system it is necessary to combine three different fundamental equations: the Poisson equation, the Nernst-Planck equation and the Navier-Stokes equations. The Poisson equation defines the electric field created by the charged particles. The Nernst-Planck equation describes the convection and diffusion of ions in a fluid flow and their dynamics in a given electric field. It is therefore sometimes called convection-diffusion equation. The Navier-Stokes equations describe the hydrodynamic interactions in the ionic solution (see also Chapter 2). Combining these three equations leads to the *electrokinetic equations*,

$$0 = \nabla^2 \psi + \frac{e}{\epsilon_m} \sum_i z_i c_i, \tag{4.2}$$

$$0 = \nabla \cdot \left(D_i \nabla c_i + \frac{D_i}{k_B T} e z_i (\nabla \psi) c_i - \boldsymbol{u} c_i \right), \tag{4.3}$$

$$0 = -\nabla p + \eta \nabla^2 \boldsymbol{u} - e(\nabla \psi) \sum_i z_i c_i, \tag{4.4}$$

$$0 = \nabla \cdot \boldsymbol{u}. \tag{4.5}$$

Here, we assume an incompressible flow and introduce the electrostatic potential ψ as well as the diffusion constant D_i of ion species i. These equations can be solved numerically using finite-element techniques.[51–53] Additionally it is possible to apply appropriate boundary conditions to consider large molecules, like colloids, in ionic solution.

If a charged colloid is immersed in ionic solution and an external electric field is applied, several polarization mechanisms play an important role. For very high frequencies the permanent dipole moments of the water molecules are reorientated in the electric field. The characteristic frequency of this *orientation polarization* is in the gigahertz regime. Due to the non-polarity of the solvent particles used in our simulations (see Chapter 7), this contribution cannot be captured in the model, however, the orientation time scales of water do not overlap with the polarization time scales that will be discussed in the following. This effect would therefore just

be an additive factor to the other polarization mechanisms. At medium frequencies the electric double layer will be deformed, because the counterions in the solution are dragged in the opposite direction of the charged colloid. This *deformation polarization* leads to the emergence of a strong dipole moment around the colloid on a time scale τ_{uc}. The field-induced ion concentration gradient, however, leads to diffusion of both co- and counterions. This *diffusion polarization* reduces the strength of the induced dipole on a time scale τ_{d}, that is larger than the deformation time scale τ_{uc}. For colloids we expect an additional contribution to the polarizability due to steric effects, called *volume polarization*. Since the ions cannot pass the hard-core colloid, the anions will accumulate on the side facing the direction of the external field, and the cations on the opposite side.

The polarizability of charged colloids has been extensively studied in the literature.[46–49;54;55] Zhou *et al.* compared in Ref. 49 simulation results to results from Maxwell-Wagner-O'Konski (MWO) theory[46;47;54] and from numerically solving the electrokinetic equations (using the software MPEK[52]). The Maxwell-Wagner-O'Konski theory models the electric polarizability by introducing a frequency-dependent conductivity $K(\omega)$, called the Clausius-Mossotti factor. This factor is related to the difference between the frequency-dependent dielectric constants of the colloid and the ions (for details, see Appendix A in Ref. 49). In Figure 4.2 results from Zhou *et al.*[49] for the polarizability of a charged colloid in ionic solution are presented. The system chosen in the reference is a colloid of size $R = 3\,\sigma$ and charge $Q = 50\,e$ in a DPD fluid (see Section 6.1). The ions are modeled by assigning a unit charge to some DPD particles and adding a hard-core repulsion to avoid accumulation of oppositely charged ions. The detailed parameters of the system can be found in Ref. 49. Since the frequency-dependence shown in this figure is universal for very different systems, the precise values are not of importance for this thesis. The figure clearly shows that the MWO theory gives a qualitatively good prediction for the polarizability. Especially the transition frequency $f_{\mathrm{t}} = 0.1\,\tau^{-1}$, where the dielectric loss has a maximum (corresponding to a minimum in the imaginary part α'' of the polarizability), is modeled very accurately, considering the simplicity of the MWO theory. This transition is also called *anomalous dispersion*.[56] The MWO theory, however, fails to describe the non-trivial behavior of the polarizability at small frequencies because it does not consider the diffusion of ions on the time scale τ_{d}. In the zero-frequency limit the diffusion of ions significantly reduces the electric polarizability. When increasing the frequency of the electric field to $f \approx 0.01\,\tau^{-1}$ its period becomes larger than the diffusion time τ_{d} and an increase in the electric polarizability compared to the zero-frequency limit is observed. This non-monotonic frequency dependence can be described by the electrokinetic equations and indeed their numerical solution is in perfect agreement with the simulation results.

We expect to observe a similar frequency-dependence for the polarizability of polyelectrolytes. This has already been extensively studied in experiments,[45;57–63] theory[64–70] and simulations.[71–73] However, in most theoretical and simulation studies
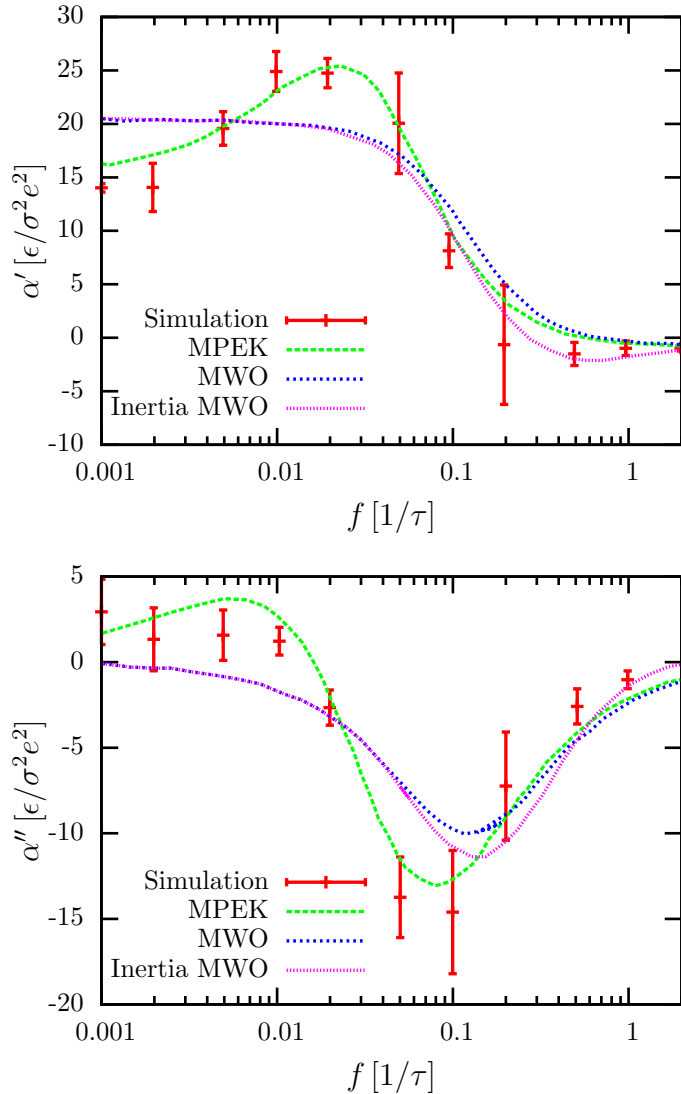
Figure 4.2: Frequency-dependence of the real part α' and imaginary part α'' of the electric polarizability of a charged colloid. The red data points are simulation results for a colloid of size $R = 3\sigma$ and charge $Q = 50\,e$ in a DPD fluid. The green lines were obtained by numerically solving the electrokinetic equations (using the software MPEK). The blue lines correspond to the original Maxwell-Wagner-O'Konski (MWO) theory. The pink lines show a correction to the MWO theory for finite ion inertia. Figure adapted from Ref. 49.

rod-like, stiff polyelectrolytes are considered. The models range from stiff cylinders[71] over rod-like particles[64–67] to short weakly-bent chains.[72;73] The conclusion of these studies is that the chain length dependence of the polarizability α is given by a power law, $\alpha \propto N^\gamma$, with $\gamma = 2 - 3$. This super-linear growth of the polarizability is explained by correlations between local dipoles induced in the backbone of the chain. For flexible chains, a generalization of these formulas has been proposed that considers a finite persistence length λ_Q.[59;68] This leads to reduced scaling exponents for chains that are longer than their persistence length $L > \lambda_Q$. In the limit of very long polyelectrolytes the scaling exponent is $\gamma = 1$. The transition from cubic to linear scaling could be observed in an outstanding experiment by Elias and Eden[59] (see Fig. 4.3). Moreover, in recent experiments by Regtmeier *et al.*, a sub-linear scaling was observed[45] ($\gamma = 0.4$). They explain their findings by proposing a modified power law that scales linearly with the radius of gyration R_g, i.e. the polyelectrolytes could be modeled as spheres with radius R_g and constant surface charge density.
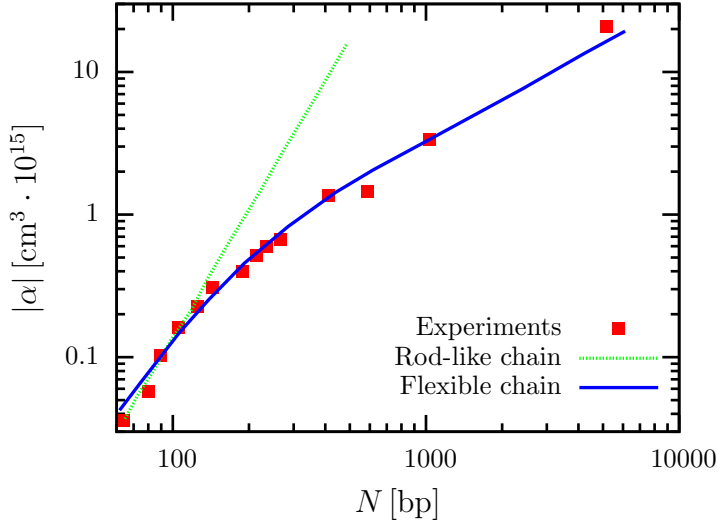
Figure 4.3: Log-log plot of the chain length dependence of the electric polarizability of DNA. The dotted line represents the cubic length dependence for rod-like chains.[64] The solid curve shows the modified theory for flexible chains with finite persistent length ($\lambda_Q = 32\,\mathrm{nm}$). Figure adapted from Ref. 59.

In a Master thesis I recently supervised it could be shown by computer simulations that for flexible polyelectrolytes in a good solvent a scaling exponent $\gamma = 1.1$ can be observed.[74] In Part II of this thesis, we will continue this study and analyze the polarizability of polyelectrolyte chains with flexible backbone. There, we will investigate three models corresponding to polyelectrolytes in solvents of different quality. This enables us to systematically analyze the influence of chain length and solvent quality on the frequency-dependent polarizability of flexible polyelectrolyte chains. The advantage of computer simulations compared to experiments is that they enable a detailed comparison between the contribution of counterion polarization in close vicinity to the polyelectrolyte and that of high-mobility uncondensed co- and counterions. This allows us to get a much deeper insight into the mechanisms that drive the polarization of the polyelectrolytes.

5

Systematic Coarse-Graining of Soft Matter Systems

To simulate complex phenomena in soft matter, it is very often necessary to coarse-grain (CG) atomistic details and construct reduced model systems. In the example of colloidal dispersions, it would be preferable to consider an implicit solvent model and simulate colloids with effective interactions. However, it has already been shown in Chapter 3 that these interactions will include frequency-dependent pairwise friction forces. It is therefore non-trivial to construct and simulate such a dynamic coarse-grained model. In some situations, reproducing the correct dynamics is not necessary, because one is only interested in static properties[a]. Therefore, we will first give an introduction to *static coarse-graining*. Afterwards, we will present the Mori-Zwanzig formalism to theoretically understand the transition from a fine-grained system to a coarse-grained model. In this section we will also derive the generalized Langevin equation (GLE), which is the fundamental equation for the CG procedure that will be derived in Part III. In the last section we will analyze the GLE and discuss how it can be applied to dynamic coarse-graining.

5.1 Static coarse-graining

The main idea behind static coarse-graining is reproducing structural properties of an underlying fine-grained system. In Figure 5.1, a coarse-graining procedure of a biomembrane is sketched. Firstly, one has to define a mapping from the all-atom system to the effective coarse-grained model. Here, every DOPC[b] lipid is replaced by 14 beads that are supposed to resemble the original atomistic lipid. Secondly, the interaction between the beads has to be determined. For this step, a huge variety of methods have been proposed. Each method targets the optimization of one or several static properties. The example in Figure 5.1 is based on a MARTINI force-field.[75;76] This force-field is optimized to reconstruct thermodynamic properties of biomolecules like solvation free energy, interfacial tension or curvature profile.

---

[a]Even in these situations one has to be careful. In systems with particle aggregation, for example, the dynamics can have an impact on the emerging structures.

[b]DOPC stands for Dipalmitoylphosphatidylcholin, a biomolecule that is an important building block of many biomembranes.
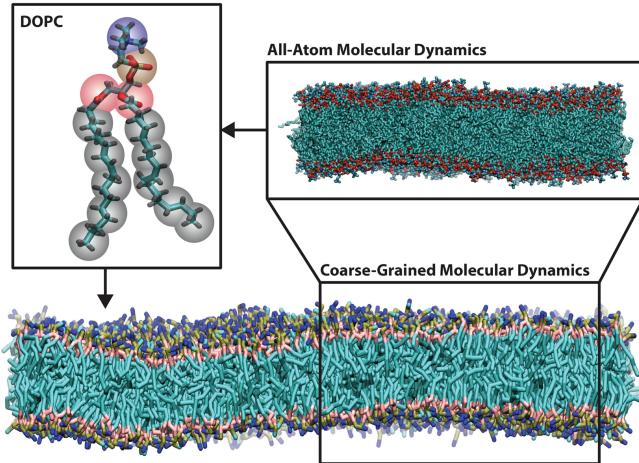
Figure 5.1: Example for a static coarse-graining procedure of a biomembrane. The all-atom DOPC lipid is replaced by effective beads that reproduce the static properties of the lipid. Figure taken from Ref. 76.

Other coarse-graining techniques are based on reproducing the mean force,[77] radial distribution functions[78;79] or entropy.[80] Since the dynamic coarse-graining procedure that is proposed in this thesis builds upon the iterative Boltzmann inversion (IBI) method,[79] we will present this technique in the following.

The basis of the iterative Boltzmann inversion is Henderson's theorem. It states that "for quantum and classical fluids with only pairwise interactions, and under given conditions of temperature and density, the pair potential $V(r)$ which gives rise to a given radial distribution function $g(r)$ is unique up to a constant." (Henderson 1974).[81] The radial distribution function (RDF) or pair-correlation function $g(r)$ describes the local, distance-dependent density around a tagged particle. The RDF is normalized by the bulk density so that an ideal gas particle fulfills,

$$g(r) = 1 \ \forall r. \tag{5.1}$$

A radial distribution function $g(r) \neq 1$ for some distances r is an indication of local structure formation and thus describes a complex fluid. It follows from the Henderson theorem that there exists a unique coarse-grained pair potential $V_{\mathrm{CG}}(r)$ that reproduces a given fine-grained radial distribution function $g_{\mathrm{FG}}(r)$. In practice it is, however, non-trivial to reconstruct the pair potential $V_{\mathrm{CG}}(r)$ because small fluctuations in $g_{\mathrm{FG}}(r)$ lead to large differences in the reconstructed potential. The aim of the iterative Boltzmann method is to construct a static coarse-grained model with a straightforward and robust algorithm that perfectly reproduces the fine-grained radial distribution function[c].

Table 5.1 summarizes the important properties of the iterative Boltzmann inversion. The first iteration step is initialized with the inverse Boltzmann potential. This potential is the final solution if the simulated fluid is infinitely dilute. In every subsequent iteration step i, a coarse-grained simulation is performed using the pair potential $V_{\mathrm{CG},i}(r)$. From these simulations, a coarse-grained RDF $g_{\mathrm{CG},i}(r)$ can be

---

[c]Recently, it could in fact be shown that IBI is similar to iterative regularization techniques known from numerical analysis.[82]

	Iterative Boltzmann inversion
Unknown quantity X	PMF $V(r)$
Matched observable Y	RDF $g(r)$
Mapping function $\phi(Y)$	$-k_B T \ln(Y)$
Initial guess X_0	$\phi(Y)$
Iteration step	$X_{i+1} = X_i + \phi(Y_{\mathrm{MD}}) - \phi(Y_i)$
$X = X_0 = \phi(Y_{\mathrm{MD}})$ valid in limit	$\rho \to 0$

Table 5.1: Summary of the important properties of the iterative Boltzmann inversion (IBI).[79] Table adapted from Ref. 83.

determined. The difference between $g_{\mathrm{CG},i}(r)$ and $g_{\mathrm{FG}}(r)$ is then used to calculate a better guess $V_{\mathrm{CG},i+1}(r)$ for the static pair potential. If the algorithm converges, the iteration ensures that the final pair potential $V_{\mathrm{CG}}(r)$ indeed reproduces the correct radial distribution function $g_{\mathrm{FG}}(r)$.

An exemplary coarse-graining procedure applying the IBI method is shown in Figure 5.2. The investigated system is nanocolloids in a Lennard-Jones (LJ) fluid. The system is initialized by placing LJ particles on a fcc-lattice with lattice constant $a = 1.71\,\sigma$ and therefore a reduced density of $\rho^* = \rho\sigma^3 = 0.8$. The reduced

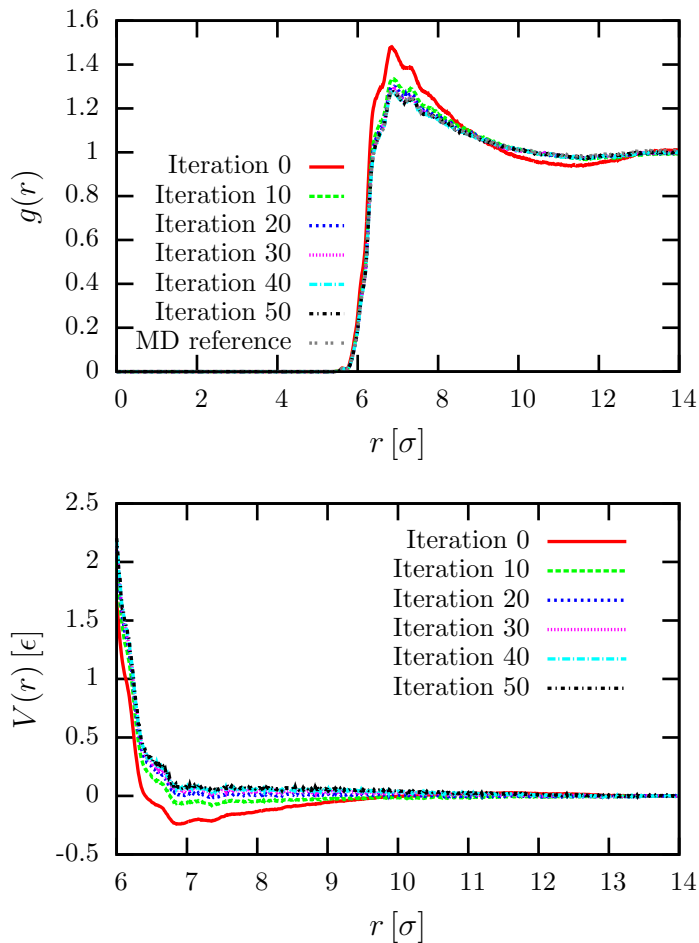**Figure 5.2:** Exemplary iterative Boltzmann inversion (IBI) steps of the static pair potential between two nanocolloids

The upper figure shows the different iterations of the radial distribution function $g(r)$. The gray reference curve lies precisely on top of iteration 50.

The lower figure visualizes the static pair potential $V(r)$. For $r < 6\,\sigma$ the potential just corresponds to a hard-core potential.

temperature is set to $T^* = k_{\mathrm{B}}T/\epsilon = 1.0$. The LJ diameter σ, energy ϵ and time $\tau = \sigma\sqrt{m/\epsilon} = 1$ are defining the length, energy and time units of the simulation. The LJ interactions are determined for a diameter $\sigma_{\mathrm{LJ}} = 1\,\sigma$, amplitude $\epsilon_{\mathrm{LJ}} = 1\,\epsilon$, cutoff $r_{\mathrm{c}} = 2.5\,\sigma$ and a particle mass $m^* = 1\,m$. This corresponds to a hard-core interaction with a small attractive tail. The colloid is carved out off the fcc-lattice with a radius $R_{\mathrm{c}} = 3\,\sigma$ and defined as a rigid body, i.e., the distances of all LJ particles forming one colloid are fixed. The resulting colloid mass is $M = 80\,m$ with a hydrodynamic radius $R_{\mathrm{H}} = 2.7\,\sigma$ (determined by the radial distribution function). LJ particles that are part of a colloid interact with other LJ particles with a cutoff $r_{\mathrm{c}} = \sqrt[6]{2}\,\sigma$, and are purely repulsive. The cubic simulation box has periodic boundary conditions in all three dimensions. To sample at the correct temperature, we equilibrate the system using a Langevin thermostat. It is then integrated with a time step $\Delta t_{\mathrm{MD}} = 0.001\,\tau$ in the NVE-ensemble. The simulations are performed with the simulation package $Lammps$.[84] This system is used for all simulations concerning hydrodynamic interactions and coarse-graining (see Part III). The important parameters and transport coefficients of the fluid are summarized in Tab. 5.2. Here, we derive the static pair-potential between two nanocolloids that will be later used to determine the conservative force for the coarse-grained simulations (see also Eq. (5.16)). The upper panel of Figure 5.2 shows that in the first iteration step, the structure is significantly overestimated. The reason for this overestimation is that the structure in the many-body simulations emerges due to layering effects, as a consequence of the hard-core potential, and not due to an attractive pair potential (see red line in the lower figure). This shows that the inverse Boltzmann potential is only valid in an infinitely dilute system. Using the iterative procedure, the potential can then be corrected until the original structure is reproduced. In the last iteration, the results for the radial distribution function from coarse-grained and molecular dynamics simulations coincide and the static pair potential has converged.

With the static pair potential derived with the IBI technique it is now possible to perform large-scale coarse-grained simulations that reproduce the correct static properties of the underlying microscopic system. The dynamical features of the two systems will, however, be completely different. To perform dynamical coarse-graining it is necessary to go one step further and derive extended equations of motion with dissipative and stochastic forces using the Mori-Zwanzig formalism.

5.2 Mori-Zwanzig formalism

In the previous section, it was shown how structural properties of atomistic systems can be recovered in coarse-grained models. The proposed methods, however, do not include the interactions of the coarse-grained variables with the fluid particles. A colloid, for example, will dissipate energy when propagating through the fluid.

	Parameter description	Value LJ	Value SI
$k_B T$	temperature	$1.0\,\epsilon$	$300\,\mathrm{K}$
L	box size	$40.0 - 100.0\,\sigma$	-
ρ_{LJ}	LJ number density	$0.8\,\sigma^{-3}$	-
ϵ	LJ interaction amplitude	$1.0\,\epsilon$	-
σ_{LJ}	LJ particle diameter	$1.0\,\sigma$	-
r_c	LJ cutoff	$2.5\,\sigma$	-
R_{c}	radius of the nanocolloid	$3.0\,\sigma$	$3.45\,\sigma$
η	shear viscosity	$2.11\,\epsilon\tau/\sigma^3$	$6.23\,\epsilon\tau/\sigma^3$
ζ	bulk viscosity	$0.88\,\epsilon\tau/\sigma^3$	$18.69\,\epsilon\tau/\sigma^3$
c_0	speed of sound	$5.63\,\sigma/\tau$	$4.05\,\sigma/\tau$

Table 5.2: Summary of the coarse-grained model parameters for the colloidal dispersion. The transport coefficients are determined with Green-Kubo relations introduced in Section 2.1 and Chapter 11. The values used in this thesis are compared to a nanocolloid ($R_{\mathrm{c}} \approx 1\,\mathrm{nm}$) in water ($30\,^{\circ}\mathrm{C}$) by applying the conversion derived in Appendix A.

Additionally, the fluid particles will randomly collide with the colloid and thus transfer energy back to the colloid. We therefore expect additional dissipative and stochastic contributions to the coarse-grained force and these contributions can be systematically derived using the Mori-Zwanzig formalism.[85–88]

The Mori-Zwanzig formalism starts with a microscopic system consisting of N particles with positions q_i and momenta p_i. The time evolution of the phase space variables $\Gamma = \{\{q_i\}, \{p_i\}\}$ is given by Hamilton's equations of motion,

$$\dot{q}_i = \frac{\partial \mathcal{H}}{\partial p_i}, \tag{5.2}$$

$$\dot{p}_i = -\frac{\partial \mathcal{H}}{\partial q_i}, \tag{5.3}$$

with the Hamiltonian $\mathcal{H}$. Using these equations, we can write down the time-dependence of an observable $A(\Gamma)$,

$$\frac{\mathrm{d}}{\mathrm{d}t} A(\Gamma(t)) = \sum_i \left[\frac{\partial \mathcal{H}}{\partial p_i} \frac{\partial}{\partial q_i} - \frac{\partial \mathcal{H}}{\partial q_i} \frac{\partial}{\partial p_i} \right] A(\Gamma) \equiv \mathrm{i}\mathcal{L}A. \tag{5.4}$$

Here, we introduced the Liouville operator $\mathcal{L}$. The formal solution of this equation is

$$A(t) = \exp(\mathrm{i}\mathcal{L}t) A(0). \tag{5.5}$$

Next, we assume the system to be in equilibrium with Boltzmann distributed phase space variables. For this system, we can define a scalar product,

$$\langle A|B \rangle = \int \mathrm{d}\Gamma \rho(\Gamma) A(\Gamma) B^*(\Gamma), \tag{5.6}$$

with Boltzmann distribution,

$$\rho(\Gamma) = \frac{\exp(-\beta\mathcal{H}(\Gamma))}{\int d\Gamma \exp(-\beta\mathcal{H}(\Gamma))}, \tag{5.7}$$

and $\beta = 1/k_{\mathrm{B}}T$. In the physical picture, this scalar product determines the correlation between the observables $A(\Gamma)$ and $B(\Gamma)$. This scalar product can now be utilized to define a projection operator $\mathcal{P}$ that distinguishes between relevant and irrelevant dynamical variables. It is important to point out that the choice of relevant and irrelevant variables is therefore not an outcome of the Mori-Zwanzig formalism but an input. To identify the most reasonable choice of coarse-grained variables already requires some insight into the microscopic system. In the following, the unspecified observable $A(\Gamma)$ will be considered as relevant variable and $\mathcal{P}$ is defined as,

$$\mathcal{P} = \frac{|A\rangle\langle A|}{\langle A|A\rangle}. \tag{5.8}$$

It is easy to show that $\mathcal{P}$ is indeed a projection operator. For the derivation of the coarse-grained equations of motion the operator $\mathcal{Q} = 1 - \mathcal{P}$ on the irrelevant variables is of great importance. The definitions of $\mathcal{P}$ and $\mathcal{Q}$ are also intuitively accessible since it is

$$\langle A|\,Q\,|B\rangle = 0 \tag{5.9}$$

for an arbitrary observable $B(\Gamma)$. Thus there are no correlations between $A(\Gamma)$ and the space of irrelevant variables. To derive the equations of motion of $A(\Gamma)$, we determine its time derivative using Eq. (5.5),

$$\frac{dA(t)}{dt} = i\mathcal{L}\exp(i\mathcal{L}t)A(0), \tag{5.10}$$

and then apply Dyson's operator relation,[87]

$$\exp(i\mathcal{L}t) - \exp(i\mathcal{L}t)\mathcal{P} = \exp(i\mathcal{L}t)\mathcal{Q} = \int_0^t du \exp(i\mathcal{L}(t-u))\mathcal{P}i\mathcal{L}\exp(i\mathcal{Q}\mathcal{L}u)\mathcal{Q} + \exp(i\mathcal{Q}\mathcal{L}t)\mathcal{Q}. \tag{5.11}$$

After some transformation we finally end up with the generalized Langevin equation (GLE),[87;88]

$$\frac{dA(t)}{dt} = i\Omega A(t) - \int_0^t ds K(t-s)A(s) + R(t), \tag{5.12}$$

with

$$i\Omega \quad = \frac{\langle A(0)|\dot{A}(0)\rangle}{\langle A(0)|A(0)\rangle}, \tag{5.13}$$

$$K(t) = \frac{\langle \dot{A}(0)|R(t)\rangle}{\langle A(0)|A(0)\rangle}, \tag{5.14}$$

$$R(t) = \exp(i\mathcal{Q}\mathcal{L}t)\mathcal{Q}\dot{A}(0). \tag{5.15}$$

In the next chapter we interpret the different terms in the GLE to give an insight into the physical picture behind this equation.

5.3 Generalized Langevin equation and dynamic coarse-graining

In the following, we will make the particular choice that $A(\Gamma) = \boldsymbol{P}$, where $\boldsymbol{P}$ are the momenta of the coarse-grained particles in the system. The three contributions to the GLE can then be identified straightforwardly.

The first term in Eq. (5.12) is already the full solution if $A(\Gamma)$ is eigenvector of the Liouville operator $\mathcal{L}$. Therefore, this term corresponds to coarse-grained forces without the influence of the irrelevant variables. This term can thus be identified as the coarse-grained force-field that was derived in the previous section about static coarse-graining.

The second term in the GLE is a time-dependent friction force. This contribution therefore represents the systematic interaction of the coarse-grained particles with the irrelevant variables. The non-Markovian nature of the interaction indicates that this term represents the "memory" of the system. Consequentially, the tensor $K(t)$ is called the memory kernel. If the relaxation of the irrelevant variables is much faster than the relaxation of the coarse-grained particles, the memory kernel becomes a delta-distribution, $K(t) = \gamma\delta(t)$. In this limit, the GLE therefore becomes the standard Langevin equation.

The third term in the GLE mimics the random collisions between the coarse-grained particles and the irrelevant degrees of freedom. Similar to the standard Langevin equation, the time-correlation function of this stochastic force is directly related to the memory kernel. This connection is called the generalized fluctuation-dissipation theorem[89] (FDT) (see Eq. (5.14)). This fundamental relation will be very important for the non-Markovian modeling since it allows one to determine the properties of the stochastic force by measuring time-correlation functions and reconstructing the memory kernel only.

Applying the above identifications, the generalized Langevin equation and the FDT

for a system of N identical particles of mass M become,

$$\boldsymbol{F}(t) = M\dot{\boldsymbol{V}}(t) = \boldsymbol{F}^{\mathrm{C}}(t) - \int_0^t \mathrm{d}s\boldsymbol{K}(t-s)\boldsymbol{V}(s) + \partial\boldsymbol{F}(t), \tag{5.16}$$

$$\langle\partial\boldsymbol{F}(t)\partial\boldsymbol{F}(t')\rangle = k_{\mathrm{B}}T\boldsymbol{K}(t-t'). \tag{5.17}$$

Here, we have introduced the velocities of the coarse-grained particles $\boldsymbol{V}(t)$, the conservative force-field $\boldsymbol{F}^{\mathrm{C}}(t)$, and the stochastic force $\partial\boldsymbol{F}(t)$. The memory kernel is now a $3N \times 3N$-dimensional tensor, describing the dissipative self- and pair-interactions between the particles. The identification of the conservative, dissipative and stochastic contributions to the GLE can be done more rigorously by applying the projection operator formalism on a concrete atomistic system (see Ref. 88). The final result is then similar to Eq. (5.16).

For a systematic coarse-graining procedure it is necessary to determine the memory kernel of a microscopic system by computer simulations or theory. The latter has already been discussed in Chapter 3 using the example of frequency-dependent hydrodynamic interactions. For more complex soft matter systems it will, however, be very difficult to determine theoretical predictions for the memory kernel. Therefore, it is important to develop a coarse-graining technique to determine memory kernels from atomistic simulations. Several methods have been proposed in the literature for this purpose.[90–95] From these, the most efficient and stable method is the inverse Volterra technique[92] that will be derived in the following. Like all the other methods the inverse Volterra technique cannot be applied to many-body systems. We will therefore consider the one-dimensional single-particle GLE in this section.

By definition, the stochastic force $\partial F(t)$ and the velocity $V(t)$ are orthogonal,

$$\langle\partial F(t)V(0)\rangle = 0, \tag{5.18}$$

which can be used to derive a noise-free differential equation for the velocity correlation function using the GLE. For this purpose, we multiply Eq. (5.16) with $V(0)$ and take the ensemble average. The result is

$$M\frac{\mathrm{d}}{\mathrm{d}t}C(t) = -\int_0^t \mathrm{d}s K(t-s)C(s), \tag{5.19}$$

with $C(t) = \langle V(t)V(0)\rangle$. This Volterra equation of first kind can in principle be numerically inverted to determine the memory kernel. However, Shin *et al.*[92] showed that it is more stable to invert a Volterra equation of second kind. This can be achieved by taking the time derivative of Eq. (5.19),

$$M\frac{\mathrm{d}^2}{\mathrm{d}t^2}C(t) = -C(0)K(t) - \int_0^t \mathrm{d}s K(s)\frac{\mathrm{d}}{\mathrm{d}t}C(t-s), \tag{5.20}$$

and identifying the derivatives of the velocity correlation function:

$$\frac{\mathrm{d}}{\mathrm{d}t}C(t) = \frac{1}{M}\langle F(t)V(0)\rangle = \frac{1}{M}C_{FV}(t),$$

(5.21)

$$\frac{\mathrm{d}^2}{\mathrm{d}t^2}C(t) = -\frac{1}{M^2}\langle F(t)F(0)\rangle = -\frac{1}{M^2}C_F(t).$$

(5.22)

Now, it is straightforward to discretize the equations and reconstruct the memory kernel:

$$K(i\Delta t) = \left\{\frac{1}{M}C_F(i\Delta t) - \frac{\Delta t}{M}\sum_{j=0}^{i-1}\omega_j C_{FV}((i-j)\Delta t)K(j\Delta t)\right\} \Big/ \left\{C(0) + \frac{\Delta t\omega_i}{M}C_{FV}(0)\right\}.$$

(5.23)

Here, we have introduced the time resolution Δt of the correlation functions determined from atomistic simulations and the weight factor $\omega_i = 1/2$ for $i = 0$ and $\omega_i = 1$ otherwise. The initial condition of the reconstruction is $MK(0) = C_F(0)/C(0)$.

Figure 5.3 shows an application of the inverse Volterra method to the self-memory kernel of a single nanocolloid. The memory kernel shows hydrodynamic backflow. At small times, the interaction of the colloid with the fluid decelerates the particle, which becomes apparent through a positive friction kernel. But the motion of the colloid induces fluid vortices which interact with the colloid at later times and therefore accelerate the particle again. At intermediate times, we can thus observe negative values for the memory kernel (see upper figure). This negative friction leads to the long-time tail in the velocity auto-correlation function.[40] The lower figure shows the relation between the memory kernel and the force auto-correlation function in Fourier space. Surprisingly, this relation is very simple, which allows a straightforward reconstruction of the memory kernel. This observation can be understood by applying a one-sided Fourier transform,

$$K(\omega) = \int_0^\infty \mathrm{d}t e^{i\omega t}K(t),$$

(5.24)

on Eq. (5.20). The result is

$$-M\omega^2 C(\omega) = -C(0)K(\omega) + i\omega K(\omega)C(\omega),$$

(5.25)

$$\Rightarrow \frac{M}{K(\omega)} = \frac{k_\mathrm{B}TM}{C_F(\omega)} + \frac{1}{i\omega}.$$

(5.26)

Here, we have used $C(0) = k_\mathrm{B}T/M$. The inverse Volterra method, memory reconstruction *via* Fourier transform and other related techniques like the orthogonal backward dynamics[93] are very efficient for non-interacting particles. In special cases they can also be applied to two-particle systems with pair-interactions.[5] However, these methods are restricted in their applicability, since they require a default input. Additionally, they are strongly dependent on the quality and time-resolution of the input correlation functions. The most successful static coarse-graining techniques
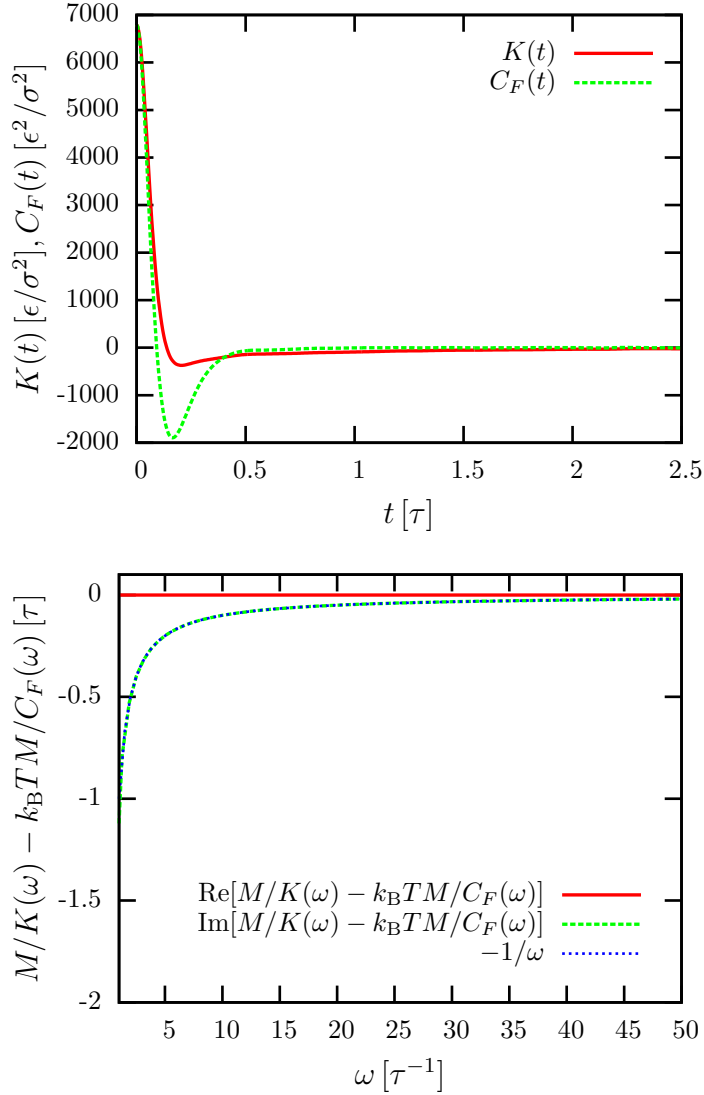
Figure 5.3: Exemplary memory reconstruction with the inverse Volterra technique using the example of hydrodynamic backflow of a nanocolloid in solution.

The upper figure visualizes the time-dependence of the memory kernel and the force auto-correlation function.

The lower figure shows the difference of the (inverse) memory kernel and force auto-correlation function in Fourier space by applying a one-sided Fourier transform (see Eq. (5.24)). The second and third curve lie exactly on top of each other.

are based on iterative algorithms. This means that they perform coarse-grained simulations with initial input parameters and optimize these parameters depending on the difference between the target function and the output of the coarse-grained simulation (see Section 5.1 about IBI). In Part III we will transfer this idea to dynamic coarse-graining using the generalized Langevin equation.

6

Computer Simulations: State of the Art

The simulations performed for this thesis are all based on the molecular dynamics (MD) method.[96;97] The basic idea of MD is to numerically solve Newton's equations of motion,

$$\frac{\mathrm{d}X(t)}{\mathrm{d}t} = V(t), \tag{6.1}$$

$$\frac{\mathrm{d}V(t)}{\mathrm{d}t} = \frac{1}{M}F(t), \tag{6.2}$$

with position $X(t)$, velocity $V(t)$ and mass M of the particles. The force-field $F(t)$ is defined by the underlying microscopic model. On the smallest, quantum mechanical scale, this could be the force exerted by the electronic structure on the nucleus.[98–100] The nucleus itself is described classically because of its large mass. On the atomistic scale, huge effort has been invested to derive consistent force-fields that model covalent or hydrogen bonds.[75;101;102] This already allows the description of single biomolecules. Furthermore, as discussed in the previous chapter, many techniques have been proposed to develop coarse-grained force-fields on the mesoscale. For a detailed description of the MD method we refer to the two excellent books "Understanding Molecular Simulation" from D. Frenkel and B. Smit[103] and "Computer Simulation of Liquids" from M. P. Allen and D. J. Tildesley.[104]

In this chapter we introduce three advanced simulation techniques that are fundamental for this work. First, we present the dissipative particle dynamics (DPD) method, a versatile Galilean-invariant thermostat that allows to efficiently model simple liquids but can also be used for polymers or colloids.[105;106] The inclusion of charged particles in the system is, however, problematic, since DPD is based on soft potentials. To efficiently simulate ionic systems, it is thus convenient to describe the charged particles within a mean-field theory. In Section 6.2, we will therefore present a numerical integrator to solve the convection-diffusion equation (see Eq. (4.3)).[107] The last section of this chapter introduces the non-Markovian DPD method, a generalization of DPD using memory kernels instead of simple friction constants.[108;109]
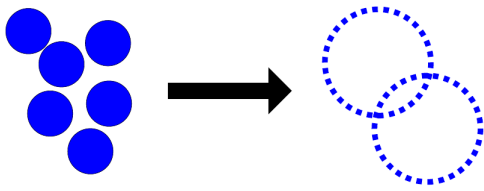
Figure 6.1: Illustration of the DPD coarse-graining procedure. Every DPD "blob" is built up of several solvent molecules. Picture taken from Ref. 113.

6.1 Dissipative particle dynamics (DPD)

The basic idea behind dissipative particle dynamics is modeling simple or complex fluids in a coarse-grained fashion. DPD was developed in 1992 by Hoogerbrugge and Koelman[105] and reformulated in a thermodynamic consistent way by Español and Warren.[106] In the former version, the algorithm did not strictly fulfill the fluctuation-dissipation theorem and the system therefore did not represent a canonical ensemble. Following the lines of Español and Warren,[106] the DPD equations of motion can be written as stochastic differential equations,

$$\frac{\mathrm{d}\boldsymbol{X}_i}{\mathrm{d}t} = \boldsymbol{V}_i \tag{6.3}$$

$$M\frac{\mathrm{d}\boldsymbol{V}_i}{\mathrm{d}t} = \sum_{j\neq i} \boldsymbol{F}_{ij}^C(\boldsymbol{R}_{ij}) - \sum_{j\neq i} \gamma\omega_{\mathrm{D}}(\boldsymbol{R}_{ij})(\boldsymbol{e}_{ij} \cdot \boldsymbol{V}_{ij})\boldsymbol{e}_{ij} + \sum_{j\neq i} \sigma\omega_{\mathrm{R}}(\boldsymbol{R}_{ij})\boldsymbol{e}_{ij}W_{ij},$$

with the velocity difference $\boldsymbol{V}_{ij} = \boldsymbol{V}_i - \boldsymbol{V}_j$, the distance $\boldsymbol{R}_{ij} = \boldsymbol{X}_i - \boldsymbol{X}_j$, $\boldsymbol{e}_{ij} = \boldsymbol{R}_{ij}/|\boldsymbol{R}_{ij}|$, Gaussian white noise, $\langle W_{ij}(t)W_{i'j'}(t')\rangle = (\delta_{ii'}\delta_{jj'} + \delta_{ij'}\delta_{ji'})\delta(t - t')$, the friction constant γ and the fluctuation-dissipation theorems $\sigma = \sqrt{2k_{\mathrm{B}}T\gamma}$ and $\omega_{\mathrm{D}}(r) = \omega_{\mathrm{R}}(r)^2$. In this work we use the weight function,

$$\omega_{\mathrm{R}}(r) = \begin{cases} 1 - \frac{r}{r_{\mathrm{c,DPD}}}, & \text{if } r < r_{\mathrm{c,DPD}} \\ 0, & \text{otherwise.} \end{cases} \tag{6.4}$$

The DPD interactions are governed by two main properties: they are pairwise and soft. The former feature is necessary to ensure local momentum conservation and therefore a straightforward implementation of hydrodynamic interactions. The softness of the interactions is important to allow large time steps and further increase the efficiency of the method. The picture behind the DPD algorithm is that every DPD "blob" represents a whole fluid region (see Fig. 6.1). If two "blobs" approach each other, they will have coarse-grained, soft interactions and the dynamics are governed by dissipative and stochastic forces (see Eq. (6.3)). Obviously, this resembles a Markovian formulation of the generalized Langevin equation. Is has indeed been shown that the DPD technique can be motivated using the Mori-Zwanzig formalism.[110;111] There are many extensions to DPD like energy-conserving, many-body or non-Markovian dissipative particle dynamics. A recent review of these extensions can be found in Ref. 112.

DPD has two major drawbacks. Although it is a very efficient mesoscale simulation technique, it is still significantly slower than similar techniques that use slightly different approaches: the Lattice-Boltzmann (LB) method[114;115] and multiparticle collision dynamics (MPCD).[116] However, DPD is more versatile and easier to implement, especially if particles are suspended in the DPD fluid. For further information, we recommend Refs. 117 and 118. Another problem is the complicated relationship between DPD input parameters and the transport coefficients of the model. Since the analytic formulas are only approximations,[119] it is always necessary to determine the transport coefficients like shear or bulk viscosity explicitly. This will be the topic of Chapter 11.

6.2 ConDiff

Since the DPD technique is based on soft potentials, the inclusion of charges in the system is problematic. Oppositely charged particles will have divergent interaction energies if they are not separated by a hard-core potential. In the literature, one can find two ways to deal with this challenge. In many studies, hard-core potentials are included, and the time step is adapted in a way that the simulation is still stable and represents a canonical ensemble with a predefined temperature (see, e.g.,[49]). Alternatively, the Coulomb interaction can be split into a short-range and a long-range contribution. The long-range contribution can be calculated using Ewald summation or related methods,[120;121] and the short-range interaction is neglected, accounting for smeared charges. Both techniques function in practice, however, it is very difficult to tune ion specific properties like their diffusivity, since the ions still interact *via* the DPD equations of motion.

In our group Stefan Medina has developed an alternative method that treats the ions on a mean-field basis.[107;113] The idea is to solve the convection-diffusion equation (see Eq. (4.3)) using pseudo particles. The velocities of these ConDiff particles are linked to the velocities of the DPD particles and thus couple to the hydrodynamic flow. Additionally, the forces of the ConDiff particles are transferred to the DPD particles according to Eq. (4.4). This force-coupling is defined in a momentum-conserving way to maintain the hydrodynamic interactions (see Fig. 6.2). The derivation of the ConDiff algorithm utilizes the well known correspondence between a deterministic Fokker-Plank equation, describing the time evolution of a density field $\rho(\boldsymbol{x}, t)$,

$$\frac{\partial \rho(\boldsymbol{x}, t)}{\partial t} + \nabla \cdot [\boldsymbol{v}(\boldsymbol{x}, t)\rho(\boldsymbol{x}, t)] = D\nabla^2 \rho(\boldsymbol{x}, t), \tag{6.5}$$

and a stochastic process $\boldsymbol{X}(t)$ describing the equations of motion of individual particles,

$$\mathrm{d}\boldsymbol{X}(t) + \boldsymbol{V}(\boldsymbol{X}(t))\mathrm{d}t = \sqrt{2D}\mathrm{d}\boldsymbol{W}(t). \tag{6.6}$$
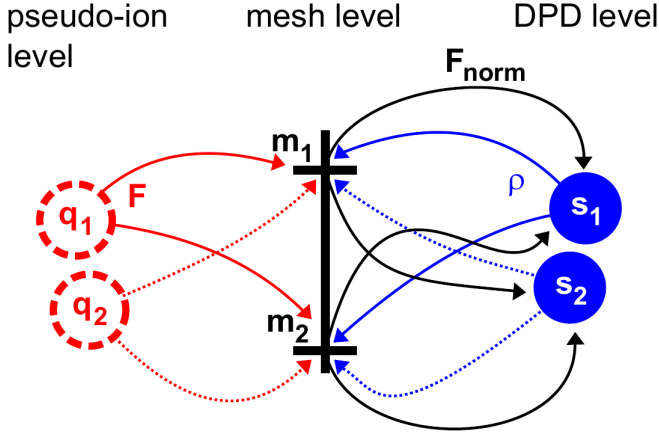
Figure 6.2: Illustration of the force-coupling between ConDiff pseudo-ions and DPD particles. The electric force is mapped on a grid, and then transferred to the DPD particles. Similarly, the velocity of the DPD particle is transferred to the pseudo-ions. Picture taken from Ref. 113.

Here, D is the diffusion constant of the particles and $\boldsymbol{W}(t)$ a Wiener process with zero mean and unit variance. It can be shown that the density of the particles evolved according to the stochastic process in Eq. (6.6) can indeed be described by the Fokker-Plank Eq. (6.5).[122] With this relationship we find that the stochastic process $\boldsymbol{X}(t)$ of the ions in the hydrodynamic flow $\boldsymbol{V}(\boldsymbol{X}(t))$ of the solute is defined by

$$\mathrm{d}\boldsymbol{X}(t) + \boldsymbol{V}(\boldsymbol{X}(t)) - zD\nabla\psi(\boldsymbol{X}(t))\mathrm{d}t = \sqrt{2D}\mathrm{d}\boldsymbol{W}(t), \tag{6.7}$$

with the valency z of the ions and the electrostatic potential $\psi(\boldsymbol{X}(t))$. This stochastic process can be integrated numerically, similar to the Langevin equation, and coupled to the DPD algorithm. For a detailed description of the algorithm, see Ref. 107.

6.3   Non-Markovian DPD

The DPD equations of motion that were introduced in Section 6.1 obviously describe a Markov process, since the time evolution of the system only depends on the present state. The algorithm can, however, be generalized to frequency-dependent friction functions using the generalized Langevin equation.[108;109] The derivation starts by rewriting the GLE Eq. (5.16) in a pairwise fashion under the assumption that one has

$$\partial \boldsymbol{F}_i(t) \approx \sum_{j\neq i} \delta \boldsymbol{F}_{ij}(t). \tag{6.8}$$

38

The equations of motion for particle i then read as follows,

$$\boldsymbol{F}_i(t) = M\dot{\boldsymbol{V}}_i(t) = \sum_{j \neq i} \left[\boldsymbol{F}_{ij}^{\mathrm{C}}(\boldsymbol{R}_{ij}) - \int_0^t \mathrm{d}s \boldsymbol{K}_{ij}(t-s)\boldsymbol{V}_{ij}(s) + \partial \boldsymbol{F}_{ij}(t) \right], \quad (6.9)$$

$$\langle \partial \boldsymbol{F}_{ij}(t) \partial \boldsymbol{F}_{ij}(t') \rangle = k_{\mathrm{B}}T \boldsymbol{K}_{ij}(t-t'), \quad (6.10)$$

with the same notation as used for the DPD equations of motion. If the coarse-grained particles have spherical symmetry, it is natural to decompose the friction into contributions parallel and orthogonal to the line-of-centers $\boldsymbol{R}_{ij}$ between the particles,

$$\boldsymbol{K}_{ij}(t) \approx K_{ij}^{\parallel}(t)\boldsymbol{e}_{ij}\boldsymbol{e}_{ij}^T + K_{ij}^{\perp}(t)(\mathbb{1} - \boldsymbol{e}_{ij}\boldsymbol{e}_{ij}^T), \quad (6.11)$$

$$\partial \boldsymbol{F}_{ij}(t) = \partial \boldsymbol{F}_{ij}^{\parallel}(t) + \partial \boldsymbol{F}_{ij}^{\perp}(t) = [\boldsymbol{e}_{ij} \cdot \partial \boldsymbol{F}_{ij}(t)]\,\boldsymbol{e}_{ij} + (\mathbb{1} - \boldsymbol{e}_{ij}\boldsymbol{e}_{ij}^T)\partial \boldsymbol{F}_{ij}(t). \quad (6.12)$$

If it is further assumed that the orthogonal contribution is negligible, and a straightforward discretization of the generalized Langevin equation is applied, one ends up with the non-Markovian DPD model,[108]

$$\frac{\mathrm{d}\boldsymbol{X}_i}{\mathrm{d}t} = \boldsymbol{V}_i, \quad (6.13)$$

$$M\frac{\mathrm{d}\boldsymbol{V}_i}{\mathrm{d}t} = \sum_{j \neq i} \boldsymbol{F}_{ij}^C(\boldsymbol{R}_{ij})$$

$$- \sum_{j \neq i}\sum_{n=0}^{T} \Delta t K_{ij,n}^{\parallel}(\boldsymbol{R}_{ij}(t-n\Delta t))\boldsymbol{V}_{ij}^{\parallel}(t-n\Delta t) + \sum_{j \neq i} \partial \boldsymbol{F}_{ij}^{\parallel}. \quad (6.14)$$

Here, we discretize the memory kernel $K_{ij}^{\parallel}(t) = \sum_{n=0}^{T} \Delta t K_{ij,n}^{\parallel}\delta(t-n\Delta t)$ and define $\boldsymbol{V}_{ij}^{\parallel}(t-n\Delta t) = [\boldsymbol{e}_{ij}(t-n\Delta t) \cdot \boldsymbol{V}_{ij}(t-n\Delta t)]\,\boldsymbol{e}_{ij}(t-n\Delta t)$.

This model was introduced by Li *et al.*[108] and represents the first numerical integrator of the generalized Langevin equation that includes pairwise interactions. The huge advantage of the model is that albeit it introduces cross-correlations between the particles, the pairs themselves are uncorrelated. This allows to integrate the equations of motion very efficiently, especially since the determination of the time-correlated random forces is more or less straightforward (see also Section 13.2.1). Li *et al.* applied their method to an incompressible star-polymer melt and they reported very promising results.[108;109]

The modeling of the colloidal suspension is, however, difficult with this technique because the coarse-grained system containing only colloidal particles is not Galilean-invariant. The reason of this symmetry breaking is the interaction of the colloids with the fluid, which is, on average, at rest in the underlying microscopic system. Therefore, the memory kernel tensor introduced in Eq. (5.16) cannot be decomposed into purely pairwise memory kernels (which corresponds to the assumption made in Eq. (6.8)). Similar to Brownian[123;124] or Stokesian dynamics[125] it is thus necessary to consider separately the dissipative self- and pair-interactions and include auto-

and cross-correlated stochastic forces. Otherwise, it would already be impossible to describe the Brownian motion of a single particle, because it only depends on the self-memory kernel of the colloids. The inclusion of self- and pair-memory kernels, however, complicates the generation of the stochastic force, since it has to be time- and cross-correlated. The discretization of this extended generalized Langevin equation and a suitable integrator will be presented in Chapter 13.

Part II

Frequency-Dependent Polarizability in Polyelectrolyte Dispersions

A Coarse-Grained Model for Polyelectrolytes in Ionic Solution

The investigation of the frequency-dependent dielectric properties of flexible polyelectrolytes cannot be carried out with atomistic simulations, because the necessary system size does not allow for sufficiently long simulations. It is therefore necessary to establish an efficient coarse-grained model for the polyelectrolytes (PE). This model should maintain several important properties of the microscopic system: the flexibility of the chain, the hydrodynamic interactions and a realistic diffusion of the fluid and the ions. All these features have an important impact on the frequency-dependent polarizability of the PE.

The model proposed in this thesis is a combination of the DPD method[105;106] as a model for the fluid and the ConDiff technique[126] to include ions within a mean-field description (see also Chapter 6). To evaluate the long-range electrostatic interactions between charged particles the P3M technique is used.[121] The PE consists of N "beads" that are DPD particles themselves, connected by harmonic bonds. The monomers in each chain additionally interact *via* a 12-6-Lennard Jones (LJ) potential. This enables the regulation of the chain solvent quality. The total charge of the PE is $q = N/2\,e$ since every second bead is charged. Taking all of this into account, the total force on bead i in the polyelectrolyte chain is given by the following contributions,

$$\boldsymbol{F}_i^{\mathrm{PE}} = \boldsymbol{F}_i^{\mathrm{DPD}} + \lambda_{\mathrm{B}} \sum_j \frac{q_i q_j}{|\boldsymbol{R}_{ij}|^2} \mathbf{e}_{ij} - 2K \sum_{\{j\}} (|\boldsymbol{R}_{ij}| - r_0) \mathbf{e}_{ij} \tag{7.1}$$

$$-4\epsilon_{\mathrm{LJ}} \sum_{j:|\boldsymbol{R}_{ij}|<r_{\mathrm{c,LJ}}} \left[12 \left(\frac{\sigma_{\mathrm{LJ}}}{|\boldsymbol{R}_{ij}|} \right)^{13} - 6 \left(\frac{\sigma_{\mathrm{LJ}}}{|\boldsymbol{R}_{ij}|} \right)^7 \right] \mathbf{e}_{ij}. \tag{7.2}$$

Here, $\{j\}$ denotes the sum over next neighbors along the chain and $r_{\mathrm{c,LJ}}$ the cutoff of the LJ potential between the polyelectrolyte beads. In Table 7.1 the model parameters are summarized. This model was introduced in the Master thesis by Sebstian Kasper, which I recently supervised.[74] There, the power law dependence of the electric polarizability on the chain length of a polyelectrolyte in a good solvent was analyzed.[127;128] It could be shown that the polarizability of the polyelectrolytes was negligible for ions with hard-core repulsion (see Section 6.2), which made the usage of a mean-field description inevitable. This observation can be explained by

	Parameter explanation	Value	Influence
$k_B T$	temperature	$1.0\,\epsilon$	-
L	box size	$20.0 - 70.0\,\sigma$	-
ρ_{DPD}	DPD number density	$3.0\,\sigma^{-3}$	-
γ	DPD friction constant	$5.0\,\tau\epsilon/\sigma^2$	-
$r_{\mathrm{c,DPD}}$	DPD cutoff	$1.0\,\sigma$	-
D	ConDiff diffusion constant	$0.1 - 0.5\,\sigma^2/\tau$	diffusion of the ions
ρ_{salt}	salt number density	$0.025\,\sigma^{-3}$	-
λ_{B}	Bjerrum length	$1.0\,\sigma$	-
z	valency of the ions	± 1	-
N	number of monomers	$10 - 100$	size of the PE
Q	charge of the polyelectrolyte	$N/2\,e$	-
K	harmonic bond strength	$60\,\epsilon/\sigma^2$	-
r_0	harmonic bond length	$1.0\,\sigma$	-
ϵ_{LJ}	LJ interaction strength	$0.6 - 1.0\,\epsilon$	solvent quality
σ_{LJ}	LJ particle diameter	$1.0\,\sigma$	-
$r_{\mathrm{c,LJ}}$	LJ cutoff	$\sqrt[6]{2} - 2\sqrt[6]{2}\,\sigma$	solvent quality

Table 7.1: Summary of the coarse-grained model parameters for the polyelectrolyte (PE) solution, including the values used in this thesis and a short explanation of their influence on the PE ("-" indicates that the influence has not been analyzed in this thesis).

the emergence of an unphysical volume polarization due to the hard-core interactions of the ions with the charged beads of the PE. Subsequently, we continued this study by investigating the influence of solvent quality and frequency on the dielectric properties of the polyelectrolyte. Since the system represents a perfect example for frequency-dependent phenomena in dispersions, it is included in this thesis. To vary the solvent quality, we studied three different polyelectrolyte models:

- PE 1: $\epsilon_{\mathrm{LJ}} = 1.0\,\epsilon, r_{\mathrm{c,LJ}} = \sqrt[6]{2}\,\sigma$,

- PE 2: $\epsilon_{\mathrm{LJ}} = 0.6\,\epsilon, r_{\mathrm{c,LJ}} = 2\sqrt[6]{2}\,\sigma$,

- PE 3: $\epsilon_{\mathrm{LJ}} = 0.7\,\epsilon, r_{\mathrm{c,LJ}} = 2\sqrt[6]{2}\,\sigma$.

The conversion from LJ units to SI units shows that the polyelectrolyte models are comparable to DNA with about 50-500 basepairs. However, the total charge of the coarse-grained polyelectrolyte is smaller than for DNA. We therefore expect quantitative differences between the polarizability of DNA and the model studied in this thesis (see also Appendix A.1).

Figure 7.1 visualizes the apparent scaling exponents ν of the radius of gyration, $R_g \propto N^\nu$, of the different PE models in equilibrium. The first polyelectrolyte without any attractive interaction between the beads is strongly elongated corresponding
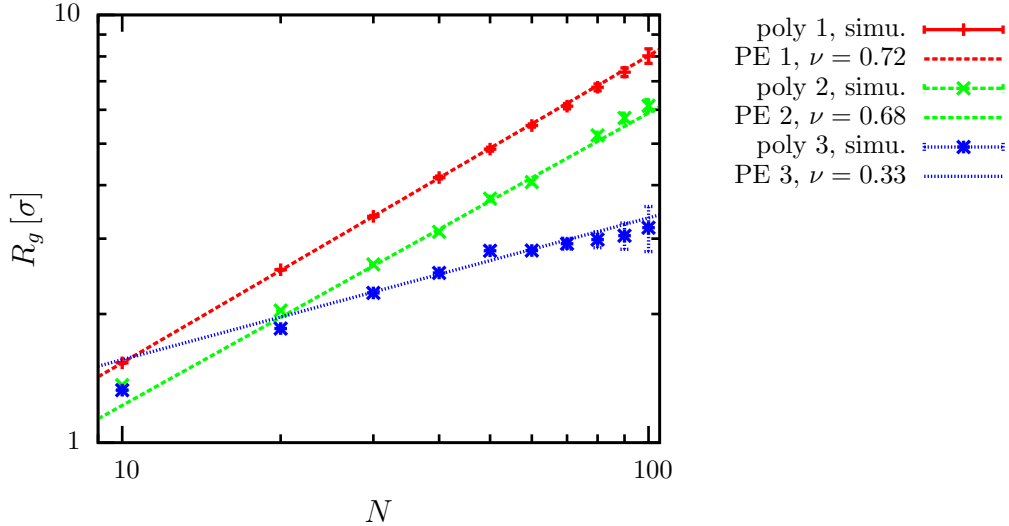
Figure 7.1: Dependence of the radius of gyration R_g on size of the polyelectrolyte (PE) and solvent quality. Simulation results are fitted to power laws, $R_g \propto N^\nu$ (the data points for $N = 10, 20$ were not included in the fit).

to a power law exponent of $\nu = 0.718 \pm 0.002$. This is much larger than the scaling expected from real chains ($\nu \approx 0.58$). Experiments on DNA have shown Flory exponents in the range of $0.45 - 0.57$, depending on their length and the salt concentration.[45;129;130] The reason for this discrepancy is the significant contribution of charged-induced repulsion since the screening length $\lambda_\mathrm{D} = 1.78\,\sigma$ is in the same order of magnitude as the size of the polyelectrolyte. Comparing the screening length to the standard scaling theories for polyelectrolytes in ionic solution[127;131–134] confirms that we are indeed in the transition regime between the rod-like limit and the ideal chain. We therefore include a small short-range attraction between the beads in the second polyelectrolyte model, leading to an apparent scaling exponent of $\nu = 0.68 \pm 0.01$. The inclusion of this short-range attraction corresponds to a change of solvent quality from good to poor. However, for small chains as simulated in this thesis, the electrostatic repulsion still leads to elongated chains. This pictures changes in the third polyelectrolyte model. The quality of the solvent is even worse in this model which leads to an exponent of $\nu = 0.33 \pm 0.02$. This value perfectly matches the scaling of real chains in a poor solvent. The linear fits in Figure 7.1 show that the scaling of the polyelectrolytes depends on the chain length which indicates that we are not yet in the long-chain limit. Exemplary configurations of polyelectrolyte model 3 are visualized in Figure 7.2. It can indeed be observed that the configuration of the longer chain is much more coiled.

To induce a dipole moment around the polyelectrolyte an external electric field $\boldsymbol{E}(t) = \boldsymbol{E}_0 e^{\mathrm{i}\omega t}$ with frequency $\omega = 2\pi f$ and amplitude $\boldsymbol{E}_0$ is applied to the system. To determine the polarizability, all ions i that are within the range $R = 4.5\,\sigma$ of the
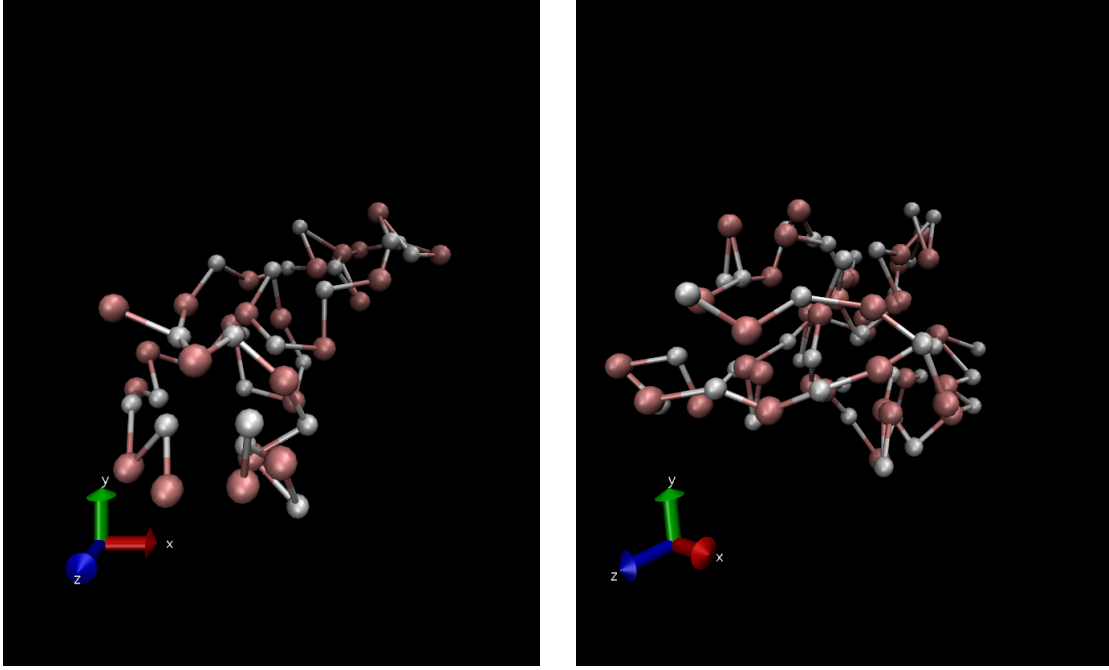
Figure 7.2: Configurations of the polyelectrolyte (PE 3) for different chain lengths N (left panel $N = 50$, right panel $N = 80$). Obviously, the right panel shows a more coiled conformation. The illustrations were created using the visualization software VMD.[135]

polyelectrolyte are considered, and the time-dependent dipole moment is,

$$\boldsymbol{p}(t) = \sum_i q_i(\boldsymbol{r}_i(t) - \boldsymbol{r}_{\text{com}}(t)). \tag{7.3}$$

Here, $q_i = \pm 1\,e$ is the charge of the co- and counterions, $\boldsymbol{r}_i$ their position and $\boldsymbol{r}_{\text{com}}$ the center-of-mass of the polyelectrolyte. The total charge Q within the considered tube around the polyelectrolyte is zero, therefore, the dipole moment does not depend on the reference point. The amplitude of the electric field is $\boldsymbol{E}_0 = (0.5\,\epsilon/(\sigma e), 0, 0)^T$, which is well within the linear response regime. The time-dependence of the dipole moment is Fourier transformed,

$$\boldsymbol{p}(\omega) = \int_0^T \mathrm{d}t e^{\mathrm{i}\omega t}\boldsymbol{p}(t), \tag{7.4}$$

which enables the determination of the frequency-dependent polarizability,

$$\alpha(w) = p_x(\omega)/E_x(\omega). \tag{7.5}$$

In general, the polarizability $\alpha(\omega)$ is a complex number. The real part, $\alpha'(\omega) = \text{Re}[\alpha(w)]$, characterizes the in-phase and lossless response of a dielectric material to an electric field. On the contrary, the imaginary part $\alpha''(\omega) = \text{Im}[\alpha(w)]$, also called the dielectric loss, quantifies the absorption of electric energy of this dielectric material. The transition from large values in the real part of the polarizability at small frequencies to a vanishing polarizability at high frequencies is called *anomalous dispersion*.[56] The transition frequency f_t is related to a typical relaxation time $\tau \approx 1/f_t$ of the polarization. If the externally applied electric field has a

frequency $f_{\mathrm{AC}} \approx f_{\mathrm{t}}$, we therefore expect a phase difference between the field and the polarization leading to an increase in the dielectric loss.

It has to be mentioned that the polyelectrolytes have the tendency to slightly unfold under the influence of the external field. This can be explained by the deformation of the double layer and therefore reduced screening of the electrostatic repulsion. However, the radius of gyration R_g did not show any significant frequency-dependence, this observation will thus not have an impact on the reported results. Interestingly, Zhou and Riehn[136] found the opposite effect for DNA under very strong alterning electric fields. They interpret their findings by large scale polarization of uncondensed ions that could lead to attractive interactions between polarizable subunits. Investigating the scaling behavior of polyelectrolytes in strong electric fields would be an interesting field of research, however, it goes beyond the scope of this work. In the next chapter we will study the anomalous dispersion of the polyelectrolyte model introduced in the previous paragraph and compare it to the results of colloid polarizability (see Chapter 4).

The Frequency-Dependence of the Electric Polarizability

The polyelectrolyte in ionic solution as described in the previous chapter is surrounded by an electric double layer of co- and counterions. Similar to the polarization mechanisms of charged colloids as discussed in Chapter 4, this double layer will deform in an external electric field and induce an effective dipole moment. The main difference compared to the polarization of colloids is the negligible contribution of volume polarization. Since the polyelectrolytes do not have a hard core, the ions can freely diffuse along the polyelectrolyte and will therefore not accumulate on its surface. This free diffusion of ions also leads to an increased relaxation of the polarized double layer. Especially for small frequencies, this is expected to have a significant impact on the polarizability of the polyelectrolytes.

When applying an external AC field with a frequency f_{AC} to the system, there are three important time scales that have an impact on the polarizability: the period of the external field $\tau_{AC} = 1/f_{AC}$, the time scale on which the electric double layer is deformed τ_{uc}, and the time τ_d in which the ions can diffuse along the polyelectrolyte to compensate ion concentration gradients. The time scale τ_{uc} is directly related to the size of the double layer, given by the Debye length $\lambda_D = 1.78\,\sigma$. In our system, the Debye length is smaller than the size of the polyelectrolyte R_g and we expect $\tau_{uc} < \tau_d$. However, the two length scales are not strongly separated which automatically implies an overlapping of these time scales.

The simulation results are shown in Figure 8.1. At high frequencies $f > 1.0\,\tau^{-1}$, the electric polarizability α is zero, because the time scale on which the electric field is varied is much smaller than the deformation time scale τ_{uc}. In other words, the particles do not have enough time to respond to the electric field. In this regime, the system with the largest ion diffusion constant D has the highest polarizability. When decreasing the frequency to $f \approx 0.1\,\tau^{-1}\,(100\,\text{MHz})$ the polarization grows significantly. Interestingly, at this point all three curves collapse, indicating that the polarizability is independent of the ion diffusion constant D. For lower frequencies, the system with the smaller diffusion constant has larger polarizability. This can be explained by the negative contribution of ion concentration relaxation, which becomes more significant on larger time scales. At a frequency of about $0.02\,\tau^{-1}$, corresponding to 20 MHz, the two systems with $D > 0.2\,\sigma^2/\tau$ reach a maximum
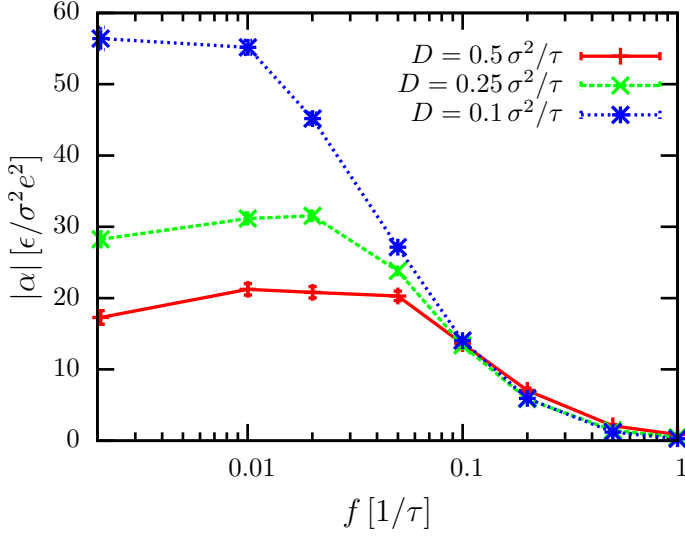
Figure 8.1: Frequency-dependence of the electric polarizability $|\alpha|$ for different ion diffusion constants D. The polyelectrolyte consists of $N = 60$ monomers (PE 1).
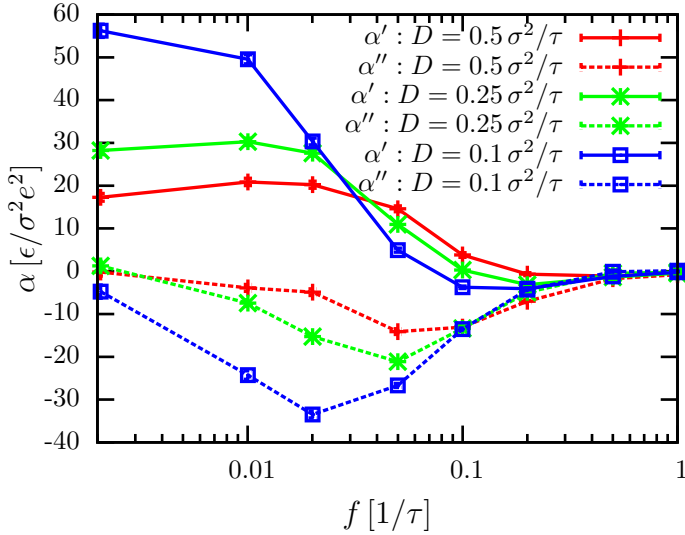

Figure 8.2: Frequency-dependence of the real part α' and imaginary part α'' of the electric polarizability for different ion diffusion constants D. The polyelectrolyte consists of $N = 60$ monomers (PE 1).

in polarizability, because at this point the contribution of diffusion polarization (which is approximately 180° phase-delayed to the electric field) increases stronger with frequency than the deformation polarization and consequentially the total polarization decreases (see also the comparison of co- and counterion polarizability in Figure 8.3).

In Figure 8.2 the real part of the polarizability $\alpha'(\omega)$ and the dielectric loss $\alpha''(\omega)$ are illustrated. The frequency-dependence of $\alpha'(\omega)$ and $\alpha(\omega)$ is very similar, however, it is noteworthy that $\alpha'(\omega)$ becomes negative for high diffusion constants and frequencies $f \approx 0.2\,\tau^{-1}$, showing that the dipole moment points in the opposite direction of the electric field. The reason for this observation is a phase difference $\phi > 90°$ between the high-frequency electric field and the response of the electric double layer. As discussed in the previous chapter, the dielectric loss is non-zero only around the transition frequency $f_{\mathrm{t}} = 0.05\,\tau^{-1}$. The sign of the dielectric loss is negative indicating that the polarizability is phase-delayed relative to the electric
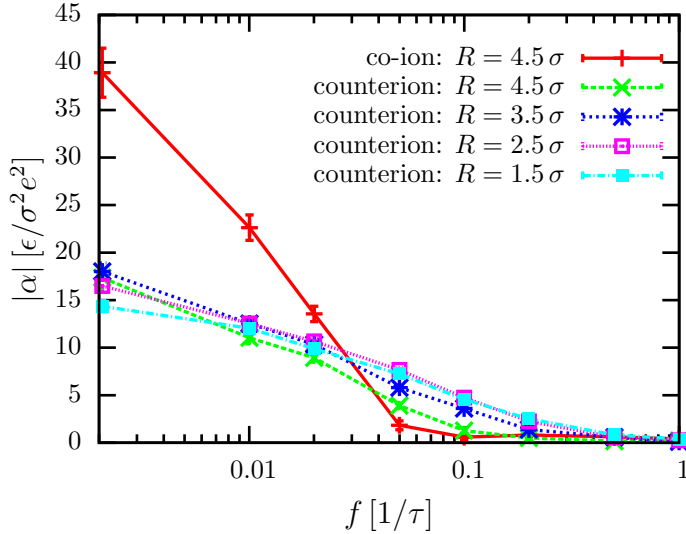
Figure 8.3: Frequency-dependence of the electric polarizability $|\alpha|$. The different curves visualize the total contribution of co-ions and the contribution of counterions in layers with a distance of R to the polyelectrolyte. The polyelectrolyte consists of $N = 60$ monomers (PE 1). The ion diffusion constant is $D = 0.25\sigma^2/\tau$.

field. The dielectric loss has a pronounced minimum at a frequency of around $f \approx 0.02\,\tau^{-1}$. This minimum is strongly dependent on the diffusion constant of the ions, which is not surprising because the minimum corresponds to the relaxation time τ of the polarization.

The results for the polarizability of polyelectrolytes are very similar to the results for charged colloids presented in Chapter 4. In particular, the distinct transition at $f_{\mathrm{t}} \approx 0.05\,\tau^{-1}$ and the maximum at $f \approx 0.02\,\tau^{-1}$ for large ion diffusion constants D can be observed for both polyelectrolytes and colloids in ionic solution. This shows that although the two systems are very different, the physical processes that drive the polarizability are strongly related. In the colloidal dispersion, the relevant length scales are the Debye length and the diameter of the colloid $d = 2R = 6\,\sigma$. The diameter is thus comparable to the radius of gyration of the polyelectrolyte R_g which explains the comparable results. The transition frequency $f_{\mathrm{t}} = 50\,\mathrm{MHz}$ can also be compared to experiments of Bellini *et al.* reporting a transition frequency of $f_{\mathrm{exp}} = 20\,\mathrm{MHz}$.[61] Considering that the model is only qualitatively matched to the experimental conditions, the agreement is very satisfying.

Figure 8.3 shows the contribution of co-ions to the polarizability. The only process that leads to a non-zero co-ion contribution is their diffusion due to concentration gradients on a time scale τ_{d}. And indeed, it can be observed that for frequencies $f > 0.05\,\tau^{-1} > \tau_{\mathrm{d}}$, the co-ion contribution is zero. This analysis therefore supports our previous discussions and shows that the time scale τ_{d} is indeed significantly larger than the deformation time scale τ_{uc}. Investigating the contribution of different counterion layers around the polyelectrolyte shows that there is a high-frequency ($f > 0.1\,\tau^{-1}$) contribution of low-mobility counterions in close vicinity to the polyelectrolyte and a low-frequency ($f < 0.1\,\tau^{-1}$) contribution of loosely bound counterions in the outer regions of the double layer. This has already been observed and extensively discussed for charged, hard rods in various publications.[71–73]
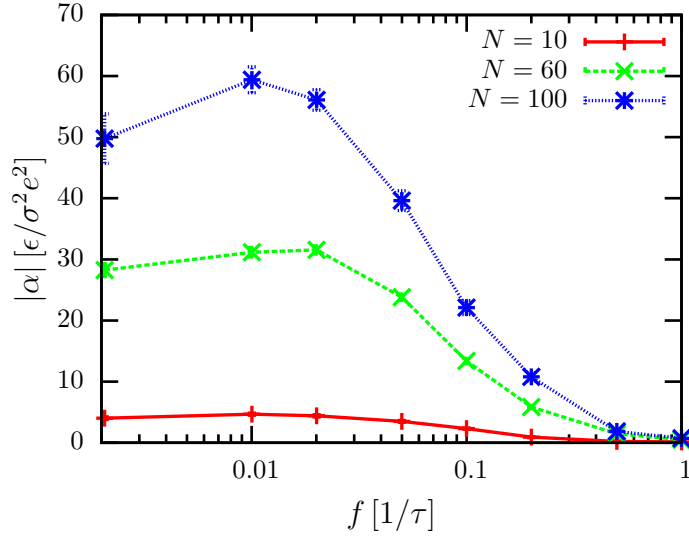
Figure 8.4: Frequency-dependence of the electric polarizability $|\alpha|$ for different chain lengths N of the polyelectrolyte (PE 1). The ion diffusion constant is $D = 0.25\sigma^2/\tau$.

In Figure 8.4 the frequency-dependent polarizability is plotted for polyelectrolytes with different chain lengths N. The figure shows that the size of the polyelectrolyte has an important influence on the amplitude of the polarizability, however, the frequency-dependence is not significantly altered. This is slightly surprising, considering that the radius of gyration is connected to the ion diffusion time scale τ_d. However, due to the strong elongation of the chain, the double layer is non-spherical and therefore the radius of gyration R_g is only a rough estimate for τ_d. It can thus be argued that this time scale does not increase significantly, leading to the observed similarities in the frequency-dependence of the polarizability. The chain length dependence of the low-frequency polarizability will be studied in detail in the next chapter.

The Effect of Solvent Quality on the Electric Polarizability

The precise knowledge of the dielectric properties of polyelectrolytes is especially important in view of the application to dielectrophoresis and the separation of DNA or proteins. In these experiments an external DC field is used to induce a drift of the polyelectrolytes through an array of dielectric traps. After injection of the polyelectrolytes, the amplitude of the AC field in the traps is increased stepwise. In this way, polyelectrolytes can be sorted by the amplitude of their electric polarizability.[45] To interpret the resulting electropherograms (see Figure 9.1) it is necessary to understand the dependence of the electric polarizability on size and conformation of the polyelectrolyte. In our simulation study we investigate polyelectrolytes with various chain lengths in solvents of different quality and thus distinct conformations (see Chapter 7).

Figure 9.2 illustrates that the chain length dependence of the polarizability is given by distinct power laws, $|\alpha| \propto N^{\gamma}$, for all polyelectrolyte models. The first model has

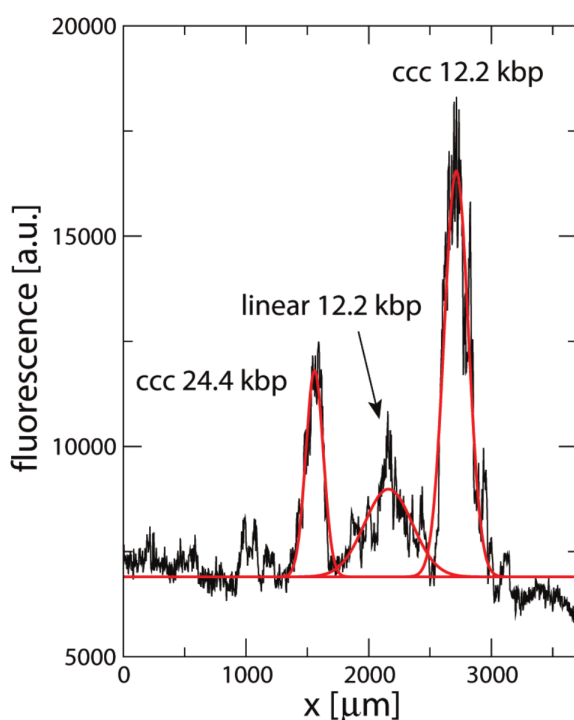**Figure 9.1:** Steady-state electropherogram showing the separation of fluorescently labeled DNA molecules of different size ($12200 - 24400$ basepairs) and conformation (covalently closed circular (ccc) and linear DNA). Picture taken from Ref. 45.
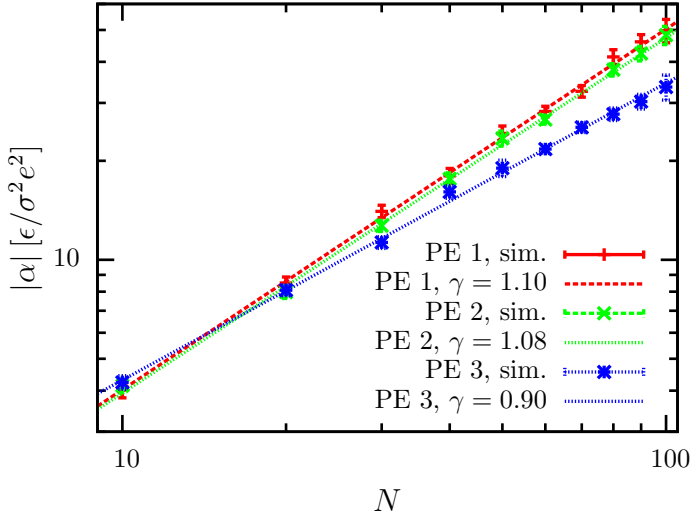
Figure 9.2: Dependence of the electric polarizability $|\alpha|$ on the chain length N of polyelectrolytes. The simulation results are fitted to power laws, $|\alpha| \propto N^{\gamma}$. The frequency of the external field is $f = 0.002\,\tau^{-1}$ and the ion diffusion constant is $D = 0.25\sigma^2/\tau$.

a slightly super-linear power law exponent $\gamma = 1.10 \pm 0.02$. This can be explained by the fact that the polarizability combines contributions from the polarization of condensed counterions and the deformation of the electric double layer. The former is supposed to scale super-linearly with exponents $\gamma = 1 - 3$ due to correlations between locally induced dipoles.[64–66;68] On the other hand, the contribution of the uncondensed ions was calculated to increase linearly with chain length.[67] The scaling exponent $\gamma = 1.1 \pm 0.02$ is therefore consistent with the theories described in the literature. The simulation study allows to investigate this scaling further and study the contribution of counterions in different layers at distances R around the polyelectrolyte.

The results are shown in Figure 9.3. It can be observed that the closest layer, containing the condensed counterions ($\gamma = 1.40 \pm 0.04$), has indeed a significantly larger scaling exponent than the loosely bound counterions ($\gamma = 1.25 \pm 0.07$). Consequentially, for small chains the contribution of the uncondensed counterions dominates the polarizability, while for large chains the polarization of the condensed counterions becomes increasingly important. This explains why the experimental results for polarizability of long DNA chains[59] can be very well described by the theoretical description of Bowers and Prud'homme[68] although the latter does not include any contributions of uncondensed ions. The same observations are valid for the second polyelectrolyte model. Different from the first polyelectrolyte, in this model the solvent quality is poor, but apparently the polarizability is not significantly changed. This is in agreement with the observed similarity between the models in the scaling exponent ν shown in Chapter 7.

The scaling behavior of the third polyelectrolyte model is, however, fundamentally different. Figure 9.2 shows that the scaling is now sub-linear with an exponent $\gamma = 0.90 \pm 0.01$ and therefore dramatically changed compared to the previous models. The simulation results can be understood by investigation of the contributions of uncondensed and condensed co- and counterions (see Figure 9.4). The condensed
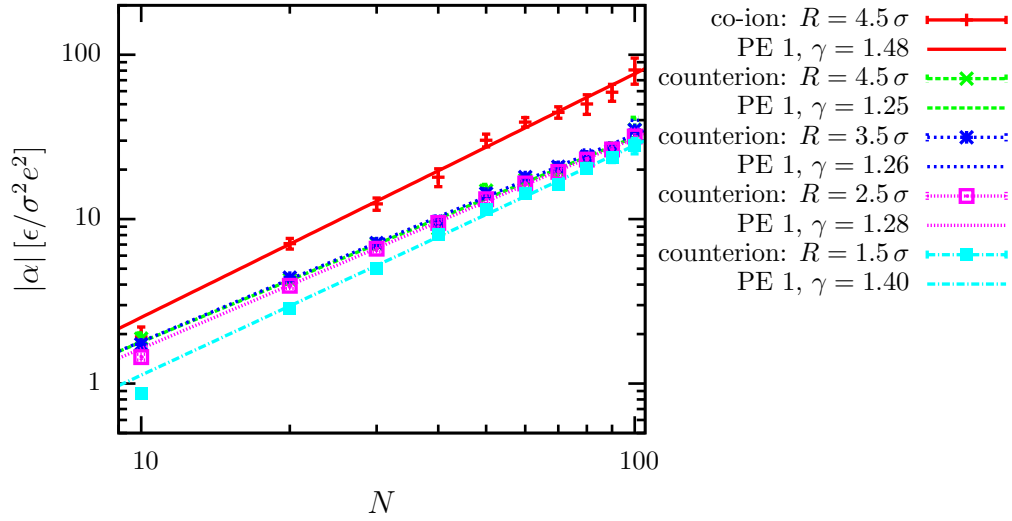
Figure 9.3: Dependence of the electric polarizability $|\alpha|$ on the chain length N of the polyelectrolytes (PE 1). The different curves visualize the total contribution of co-ions and the contribution of counterions in layers with a distance of R to the polyelectrolyte. The simulation results are fitted to power laws, $|\alpha| \propto N^\gamma$ (the data points for $N = 10, 20$ were not included in the fit). The frequency of the external field is $f = 0.002\,\tau^{-1}$ and the ion diffusion constant is $D = 0.25\sigma^2/\tau$.
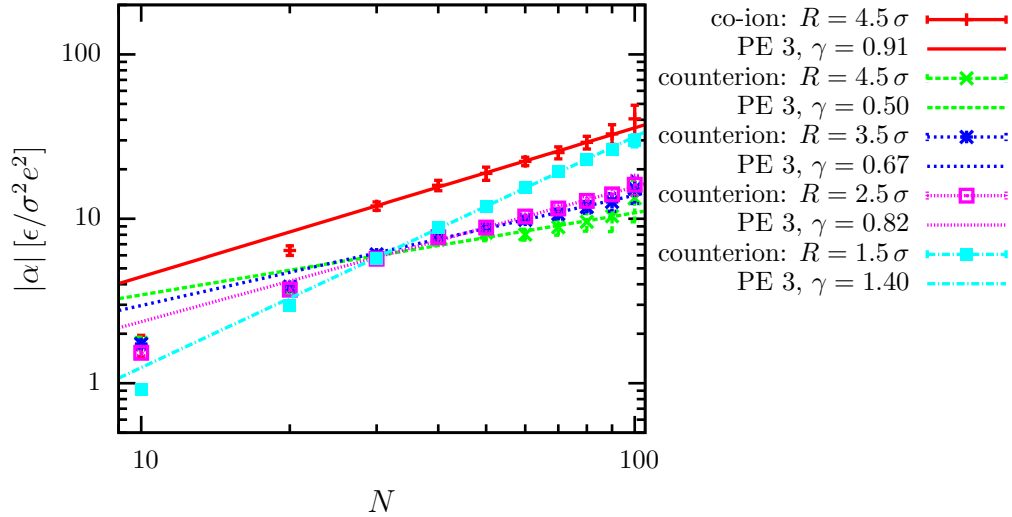
Figure 9.4: Dependence of the electric polarizability $|\alpha|$ on the chain length N of the polyelectrolytes (PE 3). The different curves visualize the total contribution of co-ions and the contribution of counterions in layers with a distance of R to the polyelectrolyte. The simulation results are fitted to power laws, $|\alpha| \propto N^\gamma$ (the data points for $N = 10, 20$ were not included in the fit). The frequency of the external field is $f = 0.002\,\tau^{-1}$ and the ion diffusion constant is $D = 0.25\sigma^2/\tau$.

counterions can still be described by a scaling exponent of $\gamma = 1.40 \pm 0.02$. For our polyelectrolyte model, this is apparently the fundamental exponent for the response of counterions in close vicinity to the polyelectrolyte. However, the contribution of the outer layers now has a significant sub-linear scaling ($\gamma = 0.50 \pm 0.04$) which is further reduced by the low-frequency diffusion of the co-ions. We have therefore shown that, depending on the scaling behavior of the polyelectrolyte, it is possible to observe both super- and sub-linear scaling of the electric polarizability. This might explain why Regtmeier et al.[45] only observed a scaling exponent of $\gamma = 0.4 \pm 0.1$ in their experimental study. In these experiments, they found a Flory exponent of $\nu = 0.45 \pm 0.05$ for the investigated very long DNA chains, which is considerably smaller than the one observed in previous experimental studies of DNA ($\nu = 0.57 \pm 0.01$).[130] Hence their buffer solution apparently was not a good solvent. It should also be mentioned that the polarization presented in Figure 9.2 scales perfectly with the chain length N. This is not obvious because the apparent scaling exponent of the radius of gyration R_g was shown to be chain length dependent (see Chapter 7). This strongly indicates that the chain length is indeed the relevant parameter to quantify the size-dependent polarizability of polyelectrolytes.

The reason for the variety of observed scaling behaviors could be strongly connected to the shape of the electric double layer. The derivation of linear scaling of the low-frequency polarizability is based on the assumption of charged hard rods.[67] Consequentially, the double layer has a tube-like shape with a radius similar to the Debye length λ_D and a length that corresponds to the size of the rod. It is easy to understand that in the limit of small Debye length, the polarization of this double layer scales linearly with rod size. If the conformation of the polyelectrolyte is considerably different from a hard rod, the situation becomes less straightforward. In the case of polyelectrolyte models 1 and 2, the double layer is apparently still tube-like and a linear scaling is observed. However, for the coiled structures of polyelectrolyte model 3, the picture changes drastically. Now, a spherical double layer is recovered which seemingly leads to a very different scaling behavior of the low-frequency polarizability. In an interesting theoretical study by Zhao[70] the different scaling exponents are explained with a size-dependent hydrodynamic draining behavior, ranging from free draining around small chains to non-draining in very long chains. The theory is based on a coil-like DNA model with radius R_g and analyzed with the electrokinetic equations (see Chapter 4). While it is appealing to explain the crossover from super-linear to sub-linear scaling with a single draining parameter f, this does not explain the very different behavior of condensed counterions and uncondensed ions studied in this work. However, in the limit of very long chains corresponding to non-draining ($f = 0$) the theory gives a possible explanation why the contribution of condensed counterions in the experiments of Regtmeier et al.[45] did not dominate the polarizability.

10

Conclusions and Outlook

In the previous chapters we studied the frequency and chain length dependence of the electric polarizability of flexible polyelectrolyte chains in ionic solution. We found that the frequency-dependence is dominated by anomalous dispersion, similar to results reported for charged colloids. The transition-frequency from high polarizability at small frequencies to low polarizability at high frequencies is approximately $f_t = 0.05\,\tau^{-1}\,(50\,\mathrm{MHz})$, which is in good agreement with experiments. Additionally, we could observe a distinct maximum in the polarizability, which goes beyond the Maxwell-Wager polarization model. This non-monotonic behavior is caused by the overlapping of two time scales: the relaxation and deformation time of the double layer, τ_{uc}, and the relaxation time of concentration gradients, τ_d. The flexibility of the polyelectrolyte therefore plays a minor role for the frequency-dependence of the polarizability. On the other hand, the amplitude of the polarizability is strongly affected by the solvent quality and thus the apparent scaling exponent of the polyelectrolyte. It has already been discussed in the literature that the polarization of condensed counterions depends on the correlation of local dipoles and therefore on the flexibility of the chain. However, the contribution of uncondensed ions in the electric double layer was only investigated for charged hard rods. In our analysis we could show that the chain length dependence of this low-frequency polarization is also strongly affected by the conformation of the polyelectrolyte. We rationalized our findings with the transition from tube-like to spherical shape of the double layer. In the tube-like limit, we found a linear dependence, in agreement with the literature about charged hard rods. However, for coiled conformations with a more spherical double layer, the scaling was significantly sub-linear.

The results are important with respect to their applications to the separation and manipulation of proteins or DNA. For example, dielectrophoresis is one possible technique to separate polyelectrolytes by their dielectric properties. The precise understanding of the different polarization mechanisms as discussed in this work is therefore essential for the correct interpretation of experimental results. In future work it will be interesting to study the flexibility-dependence of the scaling exponent $\gamma(\nu)$ in a more quantitative way and derive a scaling theory similar to the results of Bowers and Prud'homme.[68] In view of the application to DNA, it would also be interesting to further improve the coarse-grained model and enable a more quantitative comparison with experimental results.

The analysis also shows how the overlapping of different time scales can lead to complex dynamical behavior. The system of polyelectrolytes or charged colloids in ionic solution would therefore be an interesting but very challenging application of the dynamical coarse-graining techniques that will be proposed in the next part. Such a coarse-grained model of charged, polarizable particles could enable interesting studies in the field of electrohydrodynamics, for example the formation of two-dimensional crystals with a frequency-dependent lattice constant.[31]

Part III

Coarse-Graining
Frequency-Dependent Phenomena
in Colloidal Dispersions

11

Rheology and Generalized Green-Kubo Relations

The work described in this chapter is reproduced from the publication "Computing bulk and shear viscosities from simulations of fluids with dissipative and stochastic interactions", Gerhard Jung and Friederike Schmid, *The Journal of Chemical Physics*, **144**, 204104 (2016).

The analysis of the frequency-dependent polarizability of polyelectrolytes shows, how physical processes on different, overlapping time scales can lead to complex dynamical properties of a soft matter system. In this part of the thesis we go one step further and propose a systematic coarse-graining technique that enables the modeling of such systems. As a first application of the method we study the frequency-dependent hydrodynamic interactions between colloids. The idea is to coarse-grain a microscopic system of colloids in dispersion and to develop a model where the fluid particles are replaced by effective equations of motion. This model is supposed to have the exact same dynamical feature as the underlying microscopic system.

In Chapters 2 and 3, we have already introduced a theoretical description of the hydrodynamic interactions using fluid dynamics. To evaluate the theoretical prediction and compare them to computer simulations, it is necessary to determine precise values for the transport coefficients that characterize the fluid. Therefore, we have introduced the Green-Kubo relations that enable the calculation of shear viscosity η and bulk viscosity ζ by evaluating equilibrium fluctuations of the dissipative stress tensor (see Section 2.1). However, we have also discussed that forces which are not invariant under time reversal symmetry do not fulfill the assumptions made in the derivation of the Green-Kubo relations.[21;23] In this chapter, we thus introduce more general equations that account for dissipative and stochastic forces and can, e.g., be applied to DPD simulations (see Chapter 6 and Part II). In 2006 Ernst and Brito[23] suggested a generic Green-Kubo relation that can be used to derive generalized Green-Kubo formulas, depending on the properties of the Liouville operator $\mathcal{L}$,

$$\mu = \mu_\infty + \frac{V}{k_B T} \int_0^\infty dt \left\langle (I_- e^{t\mathcal{L}} I_+ \right\rangle_0 . \tag{11.1}$$

Here, μ denotes an arbitrary transport coefficient and μ_∞ its instantaneous con-

tribution (e.g. due to stochastic forces). The projected momentum current I is the projection of the dissipative stress tensor onto the dynamical subspace that is perpendicular to the space spanned by the time-dependent hydrodynamic fields (for details, see the following Sections 11.1 and 11.2),

$$I = Q(\sigma - \langle \sigma \rangle_0). \tag{11.2}$$

In other words, the projection operator Q projects onto the irrelevant variables that are neglected when describing the system by hydrodynamic fields, similar to the notation that was introduced in Section 5.2 for the Mori-Zwanzig projection operator formalism. The pseudo-streaming operator $e^{t\mathcal{L}}$ then defines the time-evolution of these projected momentum currents, $I_+(t) = e^{t\mathcal{L}} I_+$. It has to be emphasized that the Liouville operator $\mathcal{L}$ is not necessarily Hermitian. Therefore, the notation was chosen in a way that I_+ refers to a forward-in-time propagation, while I_- is connected to the time-reversed transform $\mathcal{L}^\epsilon$ of the Liouville operator, $I_-(t) = e^{t\mathcal{L}^\epsilon} I_-$. To account for this asymmetry, the dissipative stress tensor has to be separated into three different contributions, σ^C, σ^D and σ^R. Here, the conservative contribution σ^C is related to such forces that are consistent to a Hermitian Liouville operator $\mathcal{L}_C^\epsilon = -\mathcal{L}_C$. The dissipative contribution σ^D includes dissipative, velocity-dependent forces, which implies $\mathcal{L}_D^\epsilon = \mathcal{L}_D$. The random contribution σ^R is related to the stochastic forces that are separated from the Green-Kubo integral as indicated in Eq. (11.1). In MD simulations, the dissipative stress tensor can be evaluated using the Irving-Kirkwood formula[137]

$$\sigma_{\alpha\beta}^{IK} = \left\langle \sigma_{\alpha\beta}^C(t) + \sigma_{\alpha\beta}^D(t) + \sigma_{\alpha\beta}^R(t) \right\rangle, \tag{11.3}$$

$$\sigma_{\alpha\beta}^C(t) = \frac{1}{V} \sum_{i<j} R_{ij\alpha}(t) F_{ij\beta}^C(t) + \frac{1}{V} \sum_i m u_{i\alpha}(t) u_{i\beta}(t), \tag{11.4}$$

$$\sigma_{\alpha\beta}^D(t) = \frac{1}{V} \sum_{i<j} R_{ij\alpha}(t) F_{ij\beta}^D(t), \tag{11.5}$$

$$\sigma_{\alpha\beta}^R(t) = \frac{1}{V} \sum_{i<j} R_{ij\alpha}(t) F_{ij\beta}^R(t), \tag{11.6}$$

with volume V, distance $\boldsymbol{R}_{ij} = \boldsymbol{R}_i - \boldsymbol{R}_j$, conservative force $\boldsymbol{F}_{ij}^C$, dissipative force $\boldsymbol{F}_{ij}^D$ and random force $\boldsymbol{F}_{ij}^R$ between two particles. With these equations it is possible to determine the different contributions to the stress tensor and apply the generic Green-Kubo relations.

In the following, we will study the consequences of the generic formula (11.1) on the Green-Kubo relations for shear viscosity η and bulk viscosity ζ.

11.1 Generalized Green-Kubo relation for the shear viscosity η

The shear viscosity η is related to the off-diagonal component of the dissipative stress tensor, σ_{xz}. The projected momentum current is thus defined as $I_\eta = Q(\sigma_{xz} - \langle \sigma_{xz} \rangle_0)$. However, since the mean value $\langle \sigma_{xz} \rangle_0$ is zero and the off-diagonal components are already in the orthogonal subspace, we get a trivial identity, $I_\eta = \sigma_{xz}$. With these considerations we can write down the generalized Green-Kubo relation for the shear viscosity,

$$
\eta = \eta_\infty + \frac{V}{k_B T} \int_0^\infty dt \left\langle (\sigma_{xz}^C(0) - \sigma_{xz}^D(0)(\sigma_{xz}^C(t) + \sigma_{xz}^D(t)) \right\rangle_0,
$$
$$
\eta_\infty = \frac{V}{k_B T} \frac{\Delta t}{2} \left\langle \sigma_{xz}^{R\,2} \right\rangle_0, \tag{11.7}
$$

where Δt is the time step of the MD simulation in which the stress tensor fluctuations are determined. The main difference to the standard Green-Kubo relation in Eq. (2.13) is the minus-sign in the integral and the separation of the stochastic force contribution. In Figure 11.1 results for the application of this generalized equation are presented. We simulated a DPD fluid (see Section 6.1) without conservative force $\boldsymbol{F}^C$ and parameters $\gamma = 5.0\,\epsilon\tau/\sigma^2$, $\Delta t = 0.01\,\tau$, and $r_{c,DPD} = 1.0\,\sigma$ for various densities ρ. The figure clearly shows that there are significant differences between the shear viscosity determined from non-equilibrium molecular dynamics (NEMD, for details, see Attachment B.1 or Refs. 11; 17) and from the standard Green-Kubo relation (2.13). When applying the generalized Green-Kubo relation, the results agree perfectly. The plot therefore reveals that for high densities and strong dissipative coupling the usage of the generalized Green-Kubo formula is obligatory. Additionally, it can be observed that the theoretical prediction from Marsh *et*
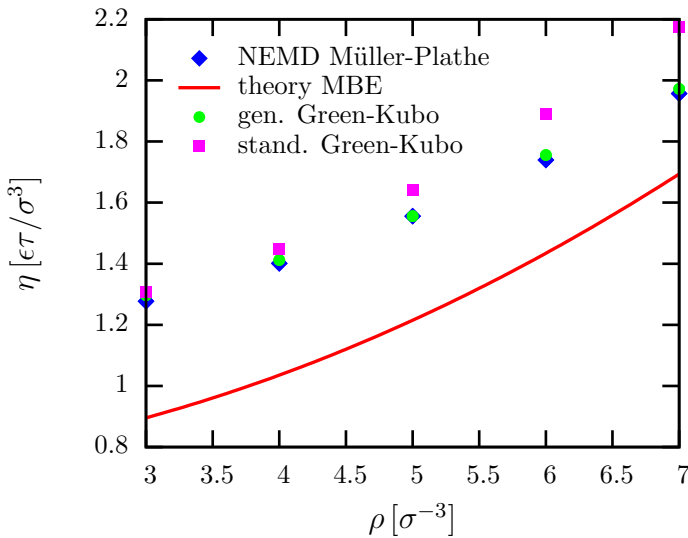

Figure 11.1: Density-dependence of the shear viscosity η of a DPD fluid. The figure compares the results from non-equilibrium molecular dynamics (NEMD)[11] (see also Appendix B), theory (MBE, see Ref. 119) and the Green-Kubo formulas in Eqs. (2.13) and (11.7). The error bars are smaller than the size of the data points. Figure adapted from Ref. 17.

al.[119] drastically underestimates the shear viscosity, as has already been noticed in Ref. 119. The reason for this discrepancy is the approximate determination of the kinetic contribution to the dissipative stress tensor.

11.2 Generalized Green-Kubo relation for the bulk viscosity ζ

The bulk viscosity depends on the trace of the dissipative stress tensor, $\text{Tr}(\boldsymbol{\sigma})$. In contrast to the off-diagonal, we now have to consider a non-vanishing mean value (which is actually related to the pressure in the system), and a non-trivial projection on the orthogonal dynamical subspace.[17;21] This can be understood by analyzing the conservative contribution to the dissipative stress tensor Eq. (11.4). The trace of the kinetic term includes the kinetic energy of the system and is therefore connected to the energy density. Since the energy density is one of the hydrodynamic fields, this contribution is not in the orthogonal subspace. It is therefore necessary to subtract the contributions to the projected momentum current that arise from energy fluctuations, and indeed the final result is[21;23]

$$I_\zeta^{\text{C}}(t) = \frac{1}{3} \sum_\alpha \left[\sigma_{\alpha\alpha}^{\text{C}}(t) - \langle \sigma_{\alpha\alpha}^{\text{C}} \rangle_0 - \frac{1}{V} \frac{\partial p}{\partial e} (\mathcal{H}(t) - \langle \mathcal{H} \rangle_0) \right],$$

$$I_\zeta^{\text{D}}(t) = \frac{1}{3} \sum_\alpha \left[\sigma_{\alpha\alpha}^{\text{D}}(t) - \langle \sigma_{\alpha\alpha}^{\text{D}} \rangle_0 \right], \tag{11.8}$$

with Hamiltonian $\mathcal{H}$, pressure p and average energy density $e = V^{-1} \langle \mathcal{H} \rangle_0$. For an ideal gas (like the DPD fluid without conservative forces introduced in the previous section) it is easy to evaluate the thermodynamic relation,

$$\frac{\partial p}{\partial e} = \frac{2}{3}. \tag{11.9}$$

With these considerations, the generalized Green-Kubo relation for the bulk viscosity is

$$\zeta = \zeta_\infty + \frac{V}{k_{\text{B}}T} \int_0^\infty dt \left\langle (I_\zeta^{\text{C}}(0) - I_\zeta^{\text{D}}(0))(I_\zeta^{\text{C}}(t) + I_\zeta^{\text{D}}(t)) \right\rangle_0,$$

$$\zeta_\infty = \frac{V}{k_{\text{B}}T} \frac{\Delta t}{18} \left\langle [\sum_\alpha \sigma_{\alpha\alpha}^{\text{R}}]^2 \right\rangle_0. \tag{11.10}$$

We applied this generalized Green-Kubo formula to the same system used in the previous section. The results are displayed in Figure 11.2. It can be observed that the viscosities determined from NEMD simulations[17] (see Attachment B.2) and the generalized Green-Kubo relation match very well. Applying the standard formula would give very inconsistent results, therefore, we did not include these
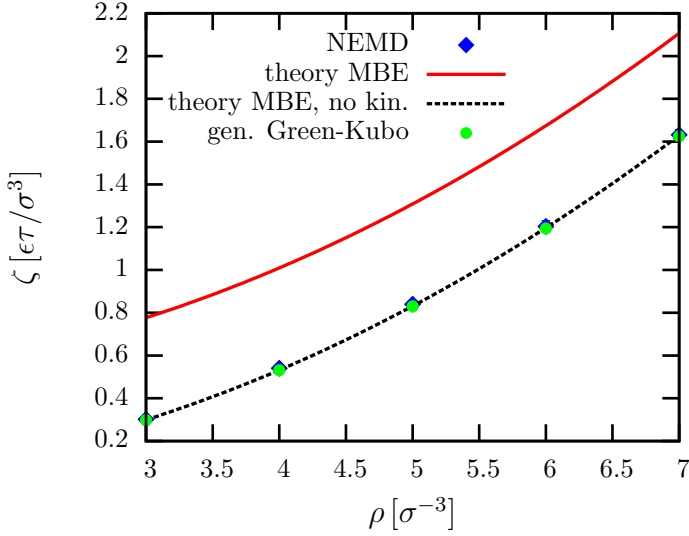
Figure 11.2: Density-dependence of the bulk viscosity ζ of a DPD fluid. The figure compares the results from NEMD[17] (see also Appendix B), theory (MBE, see Ref. 119, plotted with and without the kinetic contribution) and the Green-Kubo formula in Eq. (11.10). The error bars are smaller than the size of the data points. Figure adapted from Ref. 17.

into the figure. Very interestingly, the theoretical prediction for the bulk viscosity is also different from the simulation results. However, the discrepancy between theory and simulations can be resolved by neglecting the kinetic contribution in the theoretical prediction. We explain this observation as follows: The kinetic contribution in the theoretical prediction for the bulk viscosity ζ in fact corresponds to the contribution of energy fluctuations to the pressure p. In formula (11.8) for the projected momentum current the corresponding term had to be subtracted. Likewise, it should also be subtracted in the Chapman-Enskog expansion that is used to derived the theoretical prediction.[119]

The presented results show that we have indeed found the correct generalized Green-Kubo relations to account for dissipative and stochastic forces. With these equations we are now able to determine consistent transport coefficients from NEMD and Green-Kubo relations. Furthermore, we can utilize the results to derive theoretical predictions for the frequency-dependent hydrodynamic interactions of colloids in a specific fluid (see Figure 3.2). In the next chapter, we will introduce a novel technique to determine these hydrodynamic interactions from computer simulations in order to be able to compare theory and simulations.

12

Iterative Reconstruction of Memory Kernels

A systematic coarse-graining procedure based on the generalized Langevin equation (see Eq. (5.16)) requires two important input functions. The first is the mean conservative force-field, $\boldsymbol{F}^{\mathrm{C}}(t)$, which includes information about structural or thermodynamic properties of the system. In the field of static coarse-graining several techniques have been proposed to reconstruct such a force-field from a microscopic system (see Section 5.1). The second input function is the memory kernel, $\boldsymbol{K}(t)$, that defines the dynamical features of the coarse-grained model. Several numerical methods have been proposed in the literature that can be used to determine memory kernels from microscopic systems.[90–95] One of these, the inverse Volterra technique, was introduced in Chapter 5. Another interesting method is the backward orthogonal dynamics technique.[93] Very different from the approaches of the other methods this technique aims at reconstructing directly the stochastic force $\partial \boldsymbol{F}(t)$ and not the memory kernel $\boldsymbol{K}(t)$. This could be very interesting for future applications in non-equilibrium systems, because it might enable the investigation of generalized fluctuation-dissipation theorems. In Ref. 83 we have derived a second order scheme for this reconstruction method. Despite this improvement, the orthogonal backwards dynamics technique and also the other methods are not applicable to many-body systems and suffer from major discretization errors if the resolution of the reconstructed dynamical correlation functions is low (see Section 5.3). In this chapter we therefore propose a technique that circumvents these problems and allows for flexible and robust determination of memory kernels.

The main idea behind our novel reconstruction scheme is to use an iterative algorithm to invert the generalized Langevin equation, similar to the iterative Boltzmann inversion (IBI) known from static coarse-graining.[79] To start the iteration a coarse-grained simulation is performed with a given memory kernel. The deviation of dynamical correlation functions determined in this simulation from those of the microscopic system will then be used to calculate a small correction to the memory kernel and so forth. If the iteration converges, the result is a memory kernel that

	IBI	IMRF	IMRV
Unknown quantity X	pair potential $V(r)$	memory kernel $K(t)$	
Matched observable Y	RDF $g(r)$	$\langle F(t)F(0)\rangle$	$\langle V(t)V(0)\rangle$
Mapping function $\phi(Y)$	$-\frac{1}{\beta}\ln(Y)$	βY	$-\beta M^2 \frac{Y(t+\Delta t)-2Y(t)+Y(t-\Delta t)}{\Delta t^2}$
Mapping function 2 $\phi_2(Y)$	$-$	$-$	$-\beta M^2 \frac{Y(t+\Delta t)-Y(t)}{\Delta t^2}$
Initial guess X_0	$\phi(Y_{\text{MD}})$		
$X = X_0$ valid in limit	$\rho \to 0$	$M \to \infty$	
Basic iteration step	$X_{i+1} = X_i + \Delta\phi_i$ with $\Delta\phi_i = \phi(Y_{\text{MD}}) - \phi(Y_i)$		
Optimized iteration step	$X_{i+1} = X_i + \alpha\,\Delta\phi_i$	$X_{i+1} = X_i + h_i(t)\,\Delta\phi_i$ (Eq. ())	

Table 12.1: Comparison of the iterative Boltzmann inversion (IBI) to the iterative memory reconstruction (IMRF, IMRV). Table adapted and extended from Ref. 83.

precisely reproduces the same dynamical correlation functions as determined from the microscopic system.

The most straightforward dynamical correlation function that can be utilized to reconstruct the memory kernel is the force auto-correlation function (FACF), $\langle F(t)F(0)\rangle$. This has two reasons: in the infinite mass limit, the FACF corresponds to the memory kernel (see Eqs. (5.20) and (5.22)) and the force fluctuations $\langle F(0)^2\rangle$ are related to the memory kernel at $t = 0$ (see the fluctuation-dissipation theorem, Eq. (5.17)),

$$\lim_{M\to\infty} \langle F(t)F(0)\rangle = \langle \partial F(t)\partial F(0)\rangle = k_{\text{B}}TK(t), \tag{12.1}$$

$$\langle F(0)^2\rangle = \langle \partial F(0)^2\rangle = k_{\text{B}}TK(0). \tag{12.2}$$

These considerations show the strong similarity between the IBI technique and the iterative reconstruction of memory kernels that is proposed in this thesis, as summarized in Table 12.1. In the following, we will call this technique the force iterative memory reconstruction (IMRF). The iteration is initialized with the original FACF and uses the difference between the FACFs of the coarse-grained simulation and the MD reference directly as a correction for the memory kernel in the next iteration step.

In practical applications, the convergence of the iteration procedure described in Table 12.1 is still poor. When applying a global correction we observed that differences between the FACFs did not disappear, but were only shifted to larger times t. Introducing a constant prefactor $\alpha < 1$ to the iteration step (as is done in IBI) was not sufficient to achieve a well-behaved convergence. Therefore, the simple solution to this problem is to introduce a "correction" time $t_{\text{cor}} = n_{\text{cor}}\Delta t$ that localizes the time window in which the correction is applied (see Eq. (12.4)). This approach leads to the iteration prescription

$$K_{i+1}(t) = K_i(t) + h_i(t)\big(\phi(Y_{\text{MD}}) - \phi(Y_i)\big), \tag{12.3}$$

with

$$
h_i(t) = \begin{cases} 1 & t/t_{\mathrm{cor}} \leq \frac{i}{2} \\ 1 - t/t_{\mathrm{cor}} + i/2 & \frac{i}{2} < t/t_{\mathrm{cor}} < \frac{i}{2} + 1 \\ 0 & t/t_{\mathrm{cor}} \geq \frac{i}{2} + 1 \end{cases} , \tag{12.4}
$$

mapping variable Y and mapping function $\phi(Y)$ as defined in Table 12.1. While the specific choice of $h_i(t)$ for $t/t_{\mathrm{cor}} \in [i/2, i/2+1]$ is arbitrary, it has to be nonnegative and continuous to prevent discontinuities in the memory kernel. The optimal choice of t_{cor} is strongly system dependent and should be determined individually. For small t_{cor}, the algorithm will always converge, the necessary number of iterations can, however, be large. Therefore, we suggest to start with large correction times and optimize until no "shifting" can be observed anymore.

Another important aspect is the choice of the fine-grained correlation function used as input for the iteration. The integration procedure that will be derived in Chapter 13 integrates the velocity with an error of the order of $\mathcal{O}(\Delta t^3)$. However, the force can only be calculated by finite differences,

$$
F(t) = M \frac{V(t + \Delta t) - V(t)}{\Delta t}, \tag{12.5}
$$

with an error in $\mathcal{O}(\Delta t)$. This leads to significant deviations in the FACF at larger time steps even though the velocity auto-correlation function $\langle V(t)V(0) \rangle$ (VACF) is reproduced very accurately. Therefore, we also propose a procedure that uses the VACF as matched observable (see Table 12.1, right column), motivated by the identity,

$$
\langle F(t)F(0) \rangle = -M^2 \frac{\partial^2}{\partial t^2} \langle V(t)V(0) \rangle . \tag{12.6}
$$

This method will be called the velocity iterative memory reconstruction (IMRV). The mapping function $\phi(Y)$ shown in the table is only one possible option. The mapping can for example also utilize the first derivative of the VACF to correct the memory kernel. This is sometimes necessary, because the second derivative can obviously not correct a linear-in-time increasing difference between the VACFs (see "Mapping function 2" in Table 12.1). In the following chapter, we will apply this alternative mapping for the IMRV because it indeed leads to a better convergence of the algorithm (see Section 14.2).

An exemplary application of the IMRV scheme is shown in Figure 12.1. The reconstructed memory kernel describes the hydrodynamic backflow of a single nanocolloid and is equivalent to the memory kernel derived with the inverse Volterra technique in Section 5.3. The numerical integrator for the GLE that is used to determine the coarse-grained time-correlation functions will be developed in the next chapter. The figure shows a well-behaved convergence that improves stepwise. The final GLE simulations using the IMRV show no significant deviations from the
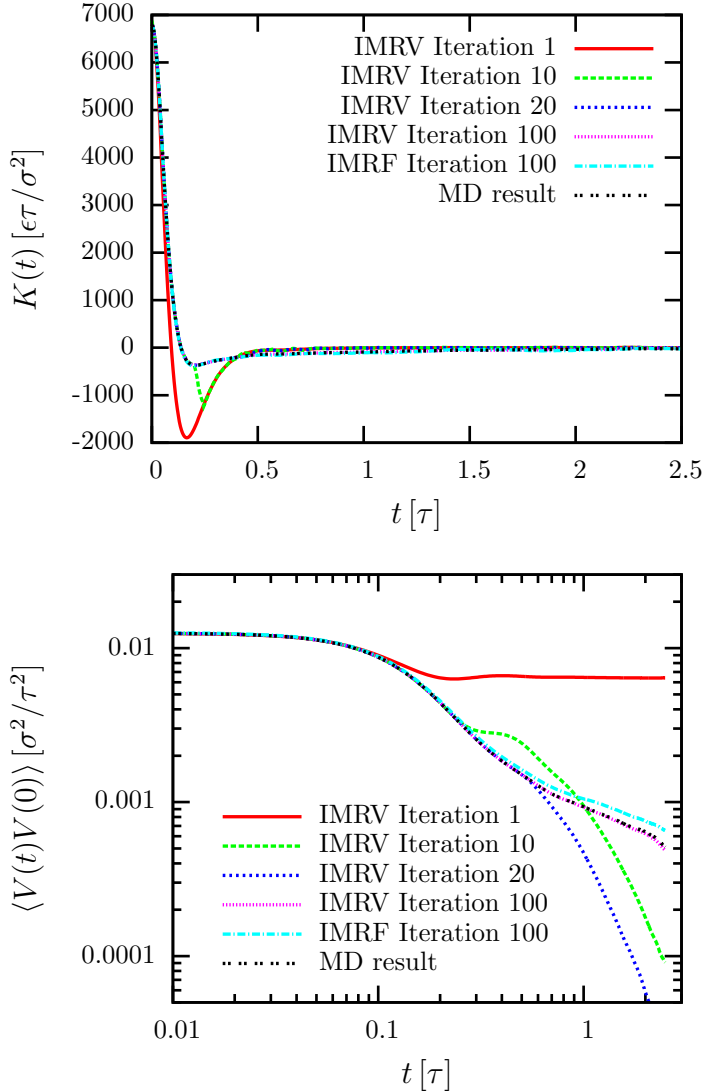
Figure 12.1: Exemplary iterative memory reconstruction. The memory kernel describes the hydrodynamic backflow of a single nanocolloid in dispersion. Results from the force and velocity iterative memory reconstruction (IMRF,IMRV) are compared to the MD results, reconstructed with the inverse Volterra technique.[92] The reconstruction time step is $\Delta t = 0.005\,\tau$ and $t_{\mathrm{cor}} = 0.05\,\tau$.

The upper figure shows the reconstructed memory kernel for different iteration steps.

The lower figure visualizes the velocity correlation function used to correct the memory kernel in each iteration step. The final IMRV result lies exactly on top of the MD reference simulation.

results using the inverse Volterra technique. Furthermore, one can see that the IMRF gives quite accurate results as well. This was expected, since the underlying MD time-correlation functions have a high resolution and small statistical errors.

In the following, we will analyze the applicability of the proposed reconstruction techniques for GLE simulations with larger time steps. The IMRV method optimizes the memory kernel in such a way that the velocity auto-correlation function is correctly reproduced. This can be observed in Figure 12.2. Independent of the time step, the final results of the iteration always match with the MD reference simulation. For time steps $\Delta t_{\mathrm{GLE}} < 0.1\,\tau$ this observation is also valid for the inverse Volterra technique. However, for larger time steps, significant differences between the coarse-grained and the reference simulations can be observed. This example illustrates the strength of the iterative memory reconstruction. If the iteration converges, the final result will always have exactly the same dynamical properties as the underlying microscopic system. In the practical application of these methods in Chapter 14 it will be shown that this property indeed enables the determination
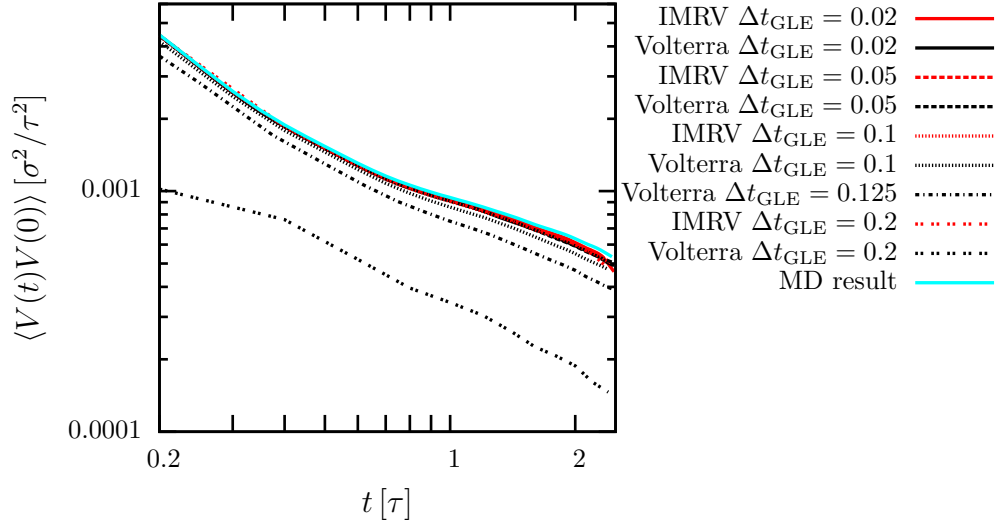
Figure 12.2: Velocity auto-correlation functions determined from GLE simulations with different time steps Δt_{GLE}. Results from the velocity iterative memory reconstruction (IMRV) are compared to the inverse Volterra technique. Except for the curve "Volterra $\Delta t_{\mathrm{GLE}} = 0.2$" all lines lie almost exactly on top of each other.

of distance-dependent self- and pair-memory kernels. There, many-body effects come into play and the inverse Volterra technique can no longer be applied.

In the next chapter, an integrator will be derived that can be used to perform coarse-grained simulations based on the generalized Langevin equation. Together with the iterative memory reconstruction presented in this chapter, we then have a powerful toolkit for dynamic coarse-grained modeling.

13

Derivation of Generalized Brownian Dynamics

In recent years several algorithms have been proposed to include non-Markovian dynamics into coarse-grained models.[108;109;138–142] Most of them are restricted to non-interacting particles without pair-memory kernels[138;139;141;142] or two-particle systems.[140] The publications of Li *et al.*[108;109] present the only technique that includes pair-memory effects into coarse-grained systems of arbitrary size. This technique is based on the assumption that the non-Markovian coarse-grained model is Galilean-invariant. This approach works well for the star-polymer melt that is investigated in Ref. 108, but the construction of implicit solvent models is not possible because the interaction of the colloids with the fluid breaks the Galilean-invariance of the system. The approximation of purely pairwise forces is thus not valid for the coarse-grained system with colloidal particles only (see also the discussion in Section 6.3). In Section 13.1, we will therefore derive a discretization of the generalized Langevin equation that allows for the integration of coarse-grained models with both self- and pair-memory kernels, called the "generalized Brownian dynamics" technique. Afterwards, we will introduce the Fourier transform technique proposed in Ref. 143 that is used to calculate time-correlated random numbers which is necessary for the determination of the stochastic force contribution.

13.1 Discretization of the generalized Langevin equation

The derivation of the generalized Brownian dynamics technique is based on the N-particle generalized Langevin equation (5.16) restricted to one- and two-body interactions,

$$M\dot{\boldsymbol{V}}_i(t) = \sum_{j\neq i} \boldsymbol{F}^{\mathrm{C}}(\boldsymbol{R}_{ij}(t)) - \int_0^t \mathrm{d}s \sum_j \boldsymbol{K}^{\mathrm{self}}(\boldsymbol{R}_{ij}(t), t-s)\boldsymbol{V}_i(s)$$

$$- \sum_{j\neq i} \int_0^t \mathrm{d}s\, \boldsymbol{K}^{\mathrm{p}}(\boldsymbol{R}_{ij}(t), t-s)\boldsymbol{V}_j(s) + \partial\boldsymbol{F}_i(t). \tag{13.1}$$

Here, $\boldsymbol{R}_{ij}(t) = \boldsymbol{R}_i(t) - \boldsymbol{R}_j(t)$ is the distance vector between the particles i and j, with position $\boldsymbol{R}_i(t)$ and velocity $\boldsymbol{V}_i(t)$. The 3×3-dimensional distance-dependent

memory kernel $\boldsymbol{K}(\boldsymbol{R}_{ij}(t), t-s)$ is composed of a self-memory kernel $\boldsymbol{K}^{\mathrm{self}}$, describing the self-diffusion of the particles, and a pair-memory function $\boldsymbol{K}^{\mathrm{p}}$ that defines the non-Markovian dissipative interaction between two particles. In Ref. 5 we have shown that the hydrodynamic self-interaction is influenced by nearby particles. In a general description it is therefore necessary to consider a distance-dependent self-memory kernel $\boldsymbol{K}^{\mathrm{self}}(\boldsymbol{R}_{ij}(t), t-s)$. In this work, we make the particular choice that $\boldsymbol{K}^{\mathrm{self}}(\boldsymbol{R}_{ij}(t), t-s) = \boldsymbol{K}^{\mathrm{s}}(t-s)\delta_{ij} + \Delta\boldsymbol{K}^{\mathrm{s}}(\boldsymbol{R}_{ij}(t), t-s)$, where the first term corresponds to the single-particle self-memory kernel and the second term accounts for the distance-dependent corrections due to nearby particles. In many applications it might be possible to assume $\Delta\boldsymbol{K}^{\mathrm{s}}(\boldsymbol{R}_{ij}(t), t-s) \approx 0$. For the above formulation of the generalized Langevin equation, the fluctuation-dissipation theorem is

$$\langle \partial \boldsymbol{F}_i(t)\partial \boldsymbol{F}_j(t')\rangle = k_{\mathrm{B}}T\boldsymbol{K}^{\mathrm{p}}(\boldsymbol{R}_{ij}(t), t-t'), \tag{13.2}$$

$$\langle \partial \boldsymbol{F}_i(t)\partial \boldsymbol{F}_i(t')\rangle = k_{\mathrm{B}}T\left(\boldsymbol{K}^{\mathrm{s}}(t-t') + \sum_{j\neq i} \Delta\boldsymbol{K}^{\mathrm{s}}(\boldsymbol{R}_{ij}(t), t-t')\right).$$

It has to be noted that the distance-dependence of the memory-kernel breaks the stationarity of the stochastic force, because the positions of the particles are obviously not time-invariant. However, it is not clear at which point in time the distance needs to be evaluated. In the present work we make the assumption that the distance of the colloid is approximately constant on the time scale on which the memory decays. We therefore chose t as the relevant time for the distance-dependence of the memory kernel in Eq. 13.2.

As a first step to find a numerical integrator for Eq. (13.1) it is necessary to introduce a discretized memory kernel. Therefore, the continuous memory kernel $\boldsymbol{K}(R_{ij}(t), t-s)$ is replaced by a discretized memory sequence $\boldsymbol{K}_m(R_{ij}(t))$. After inserting this approach into the GLE, the final results for the GLE and the fluctuation-dissipation theorem are (see Attachment C for details)

$$M\dot{\boldsymbol{V}}_i(t) = \sum_{j\neq i} \boldsymbol{F}^{\mathrm{C}}(\boldsymbol{R}_{ij}(t)) - \sum_{m=0}^{T-1}\left(\boldsymbol{K}_m^{\mathrm{s}} + \sum_{j\neq i} \Delta\boldsymbol{K}_m^{\mathrm{s}}(\boldsymbol{R}_{ij}(t))\right)\boldsymbol{V}_i(t-m\Delta t)$$

$$- \sum_{j\neq i}\sum_{m=0}^{T-1} \boldsymbol{K}_m^{\mathrm{p}}(\boldsymbol{R}_{ij}(t))\boldsymbol{V}_j(t-m\Delta t) + \partial\boldsymbol{F}_i(t), \tag{13.3}$$

$$\langle \partial\boldsymbol{F}_i(t)\partial\boldsymbol{F}_j(t')\rangle = k_{\mathrm{B}}T\sum_{m=0}^{T-1} a_m\boldsymbol{K}_m^{\mathrm{p}}(\boldsymbol{R}_{ij}(t))\delta(t-t'-m\Delta t), \tag{13.4}$$

$$\langle \partial\boldsymbol{F}_i(t)\partial\boldsymbol{F}_i(t')\rangle = k_{\mathrm{B}}T\sum_{m=0}^{T-1} a_m\left(\boldsymbol{K}_m^{\mathrm{s}} + \sum_{j\neq i} \Delta\boldsymbol{K}_m^{\mathrm{s}}(\boldsymbol{R}_{ij}(t))\right)\delta(t-t'-m\Delta t),$$

with the discretization time step Δt of the GLE and the weight factor $a_m = 2$ for $m = 0$ and $a_m = 1$, otherwise. For computational reasons we introduce a cutoff T of the memory sequence, thus the memory of the system is included on a time scale $\tau_{\mathrm{mem}} = T\Delta t$. An important alternative to the discretization of

the memory kernel is to introduce auxiliary variables to the generalized Langevin equation. These additional degrees of freedom mimic the memory of the system and recover Markovian equations of motion. This formalism was successfully applied to non-interacting particles,[139;141] two-particle microrheology[140;144] and the non-Markovian DPD method.[109] The inclusion of auto- and cross-correlations into the system, however, complicates the situation and makes it difficult to derive a similar formalism. A detailed discussion on the auxiliary variable expansion can be found in Attachment D.

Starting from Eqs. (13.3)-(13.4) we derive a numerical integrator for the generalized Langevin equation by following the scheme introduced by Grønbech-Jensen and Farago.[145] An application of this scheme to the single-particle GLE can be found in Ref. 83. Here, we show the extension to the full multiparticle GLE. The first step is to integrate the GLE from $t_n = n\Delta t$ to $t_{n+1} = t_n + \Delta t$. For the time-discretized velocity and position of particle i we use the notation $\boldsymbol{V}_{i,n} = \boldsymbol{V}_i(n\Delta t)$ and $\boldsymbol{R}_{i,n} = \boldsymbol{R}_i(n\Delta t)$, respectively. The integration leads to the following equations of motion,

$$M(\boldsymbol{V}_{i,n+1} - \boldsymbol{V}_{i,n}) = -\boldsymbol{K}_0^{\mathrm{s}}\left[\boldsymbol{R}_{i,n+1} - \boldsymbol{R}_{i,n}\right] + \Delta t\left(\boldsymbol{F}_{i,n}^{\mathrm{D}} + \boldsymbol{F}_{i,n}^{\mathrm{R}}\right) + \sum_{j\neq i}\int_{t_n}^{t_n+\Delta t} \mathrm{d}t\, \boldsymbol{F}^{\mathrm{C}}(\boldsymbol{R}_{ij}(t)),$$

(13.5)

with the non-Markovian dissipative force $\boldsymbol{F}_{i,n}^{\mathrm{D}}$ and stochastic force $\boldsymbol{F}_{i,n}^{\mathrm{R}}$ given by

$$\Delta t\boldsymbol{F}_{i,n}^{\mathrm{D}} = -\sum_{j\neq i}\sum_{m=0}^{T-1}\int_{t_n}^{t_n+\Delta t}\mathrm{d}t\left[\Delta\boldsymbol{K}_m^{\mathrm{s}}(\boldsymbol{R}_{ij}(t))\boldsymbol{V}_i(t-m\Delta t) + \boldsymbol{K}_m^{\mathrm{p}}(\boldsymbol{R}_{ij}(t))\boldsymbol{V}_j(t-m\Delta t)\right]$$

$$-\sum_{m=1}^{T-1}\boldsymbol{K}_m^{\mathrm{s}}\left[\boldsymbol{R}_{i,n-m+1} - \boldsymbol{R}_{i,n-m}\right],$$

(13.6)

$$(\Delta t)^2\langle\boldsymbol{F}_{i,n+m}^{\mathrm{R}}\boldsymbol{F}_{j,n}^{\mathrm{R}}\rangle = k_{\mathrm{B}}Ta_m\int_{t_{n+m}}^{t_{n+m}+\Delta t}\mathrm{d}t\,\boldsymbol{K}_m^{\mathrm{p}}(\boldsymbol{R}_{ij}(t)),$$

(13.7)

$$(\Delta t)^2\langle\boldsymbol{F}_{i,n+m}^{\mathrm{R}}\boldsymbol{F}_{i,n}^{\mathrm{R}}\rangle = k_{\mathrm{B}}Ta_m\left(\boldsymbol{K}_m^{\mathrm{s}}\Delta t + \sum_{j\neq i}\int_{t_{n+m}}^{t_{n+m}+\Delta t}\mathrm{d}t\Delta\boldsymbol{K}_m^{\mathrm{s}}(\boldsymbol{R}_{ij}(t))\right).$$

Except for the discretization of the memory kernel, no approximations were made in the derivation of the above equation. However, to find an explicit integration scheme, it is now necessary to make the following assumptions:

- The pair-memory kernel $\boldsymbol{K}_m^{\mathrm{p}}(\boldsymbol{R}_{ij}(t))$ and distance-dependent self-memory kernel $\Delta\boldsymbol{K}^{\mathrm{s}}(\boldsymbol{R}_{ij}(t))$ do not change significantly during one time step,

$$\boldsymbol{K}_m^{\mathrm{p}}(\boldsymbol{R}_{ij}(t)) = \boldsymbol{K}_m^{\mathrm{p}}(\boldsymbol{R}_{ij,n}) \qquad \forall t \in [t_n, t_n + \Delta t], \qquad (13.8)$$

$$\Delta\boldsymbol{K}_m^{\mathrm{s}}(\boldsymbol{R}_{ij}(t)) = \Delta\boldsymbol{K}_m^{\mathrm{s}}(\boldsymbol{R}_{ij,n}) \qquad \forall t \in [t_n, t_n + \Delta t]. \qquad (13.9)$$

- The integration of the position, $\dot{\boldsymbol{R}}_i = \boldsymbol{V}_i$, can be approximated by [145;146]

$$\boldsymbol{R}_{i,n+1} - \boldsymbol{R}_{i,n} = \frac{\Delta t}{2}\left(\boldsymbol{V}_{i,n+1} + \boldsymbol{V}_{i,n}\right) + \mathcal{O}(\Delta t^3). \tag{13.10}$$

- Similar to Ref. 145 the integral of the conservative force $\boldsymbol{F}^{\mathrm{C}}(\boldsymbol{R}_{ij}(t))$ will be approximated such that positions and velocities are correct to second order in Δt.

On the basis of these approximations the generalized Brownian dynamics integrator can be derived,

$$\boldsymbol{R}_{i,n+1} = \boldsymbol{R}_{i,n} + b\Delta t \boldsymbol{V}_{i,n} + \frac{b\Delta t^2}{2M}\left(\boldsymbol{F}^{\mathrm{C}}(\boldsymbol{R}_{ij,n}) + \boldsymbol{F}^{\mathrm{D}}_{i,n} + \boldsymbol{F}^{\mathrm{R}}_{i,n}\right), \tag{13.11}$$

$$\boldsymbol{V}_{i,n+1} = a\boldsymbol{V}_{i,n} + \frac{\Delta t}{2M}\left(a\boldsymbol{F}^{\mathrm{C}}(\boldsymbol{R}_{ij,n}) + \boldsymbol{F}^{\mathrm{C}}(\boldsymbol{R}_{ij,n+1})\right) + \frac{b\Delta t}{M}\left(\boldsymbol{F}^{\mathrm{D}}_{i,n} + \boldsymbol{F}^{\mathrm{R}}_{i,n}\right),$$

with,

$$\Delta t \boldsymbol{F}^{\mathrm{D}}_{i,n} = -\sum_{j\neq i}\left[\boldsymbol{K}^{\mathrm{p}}_0(\boldsymbol{R}_{ij,n})\boldsymbol{V}_{j,n} + \Delta \boldsymbol{K}^{\mathrm{s}}_0(\boldsymbol{R}_{ij,n})\boldsymbol{V}_{i,n}\right]\Delta t \tag{13.12}$$

$$- \sum_{m=1}^{N-1}\boldsymbol{K}^{\mathrm{s}}_m\left[\boldsymbol{R}_{i,n-m+1} - \boldsymbol{R}_{i,n-m}\right] - \sum_{j\neq i}\sum_{m=1}^{N-1}\boldsymbol{K}^{\mathrm{p}}_m(\boldsymbol{R}_{ij,n})\left[\boldsymbol{R}_{j,n-m+1} - \boldsymbol{R}_{j,n-m}\right]$$

$$- \sum_{j\neq i}\sum_{m=1}^{N-1}\Delta \boldsymbol{K}^{\mathrm{s}}_m(\boldsymbol{R}_{ij,n})\left[\boldsymbol{R}_{i,n-m+1} - \boldsymbol{R}_{i,n-m}\right],$$

$$(\Delta t)^2\left\langle \boldsymbol{F}^{\mathrm{R}}_{i,n+m}\boldsymbol{F}^{\mathrm{R}}_{j,n}\right\rangle = k_{\mathrm{B}}Ta_m\boldsymbol{K}^{\mathrm{p}}_m(\boldsymbol{R}_{ij,n+m})\Delta t,$$

$$(\Delta t)^2\left\langle \boldsymbol{F}^{\mathrm{R}}_{i,n+m}\boldsymbol{F}^{\mathrm{R}}_{i,n}\right\rangle = k_{\mathrm{B}}Ta_m\left(\boldsymbol{K}^{\mathrm{s}}_m + \sum_{j\neq i}\Delta \boldsymbol{K}^{\mathrm{s}}_m(\boldsymbol{R}_{ij,n+m})\right)\Delta t, \tag{13.13}$$

$$a \equiv \frac{1 - \frac{K^{\mathrm{s}}_0\Delta t}{2M}}{1 + \frac{K^{\mathrm{s}}_0\Delta t}{2M}} \qquad \text{and} \qquad b \equiv \frac{1}{1 + \frac{K^{\mathrm{s}}_0\Delta t}{2M}}. \tag{13.14}$$

Up to this point, the memory kernels $\boldsymbol{K}^{\mathrm{s}}_m$, $\Delta \boldsymbol{K}^{\mathrm{s}}_m(\boldsymbol{R}_{ij,n+m})$ and $\boldsymbol{K}^{\mathrm{p}}_m(\boldsymbol{R}_{ij,n+m})$ have not been specified. However, two important constraints have to be considered:

- *Positive definiteness*: The auto- and cross-correlations of the $3N$-dimensional stochastic force vector $\boldsymbol{F}^{\mathrm{R}}_{i,n}$ can be described by a $3N \times 3N$-dimensional correlation matrix (see also Eq. (13.23)) which has to be *positive definite*. Since this matrix depends on the positions of the particles it is, in principle, necessary to prove that the input memory kernels lead to a positive definite correlation matrix for all possible particle configurations (similar to comparable proofs of the positive definiteness of the Rotne-Prager tensor used in Brownian dynamics [147]). In practice, proving the general positive definiteness will be obviously very difficult, therefore, we always checked for positive definiteness in our simulations.

- *Instantaneous contribution*: The instantaneous contributions of the memory kernels, $\boldsymbol{K}_0^{\mathrm{p}}(\boldsymbol{R}_{ij,n})$ and $\Delta\boldsymbol{K}_0^{\mathrm{s}}(\boldsymbol{R}_{ij,n})$, are integrated differently than the other memory kernels, which is necessary in order to obtain an explicit integration scheme (see Eq. (13.12)). This will have an impact on the precision of the method if the instantaneous contribution is large. Therefore, it has to be ensured that $\boldsymbol{K}_0^{\mathrm{p}}(\boldsymbol{R}_{ij,n}) \approx \Delta\boldsymbol{K}_0^{\mathrm{s}}(\boldsymbol{R}_{ij,n}) \ll \boldsymbol{K}_0^{\mathrm{s}}$. Otherwise, an implicit integration scheme has to be derived, which can be solved by matrix inversion (this inversion could be efficiently realized using the Lanczos algorithm,[148–150] see Section 13.2.2).

In most applications, the interactions between two particles will be separated into contributions parallel and orthogonal to the line-of-centers between the particles, as discussed in Section 6.3. The memory kernels are therefore decomposed in the following way,

$$\boldsymbol{K}(R_{ij}(t),t') \approx K^{\parallel}(R_{ij}(t),t')\boldsymbol{e}_{ij}\boldsymbol{e}_{ij}^T + K^{\perp}(R_{ij}(t),t')(1 - \boldsymbol{e}_{ij}\boldsymbol{e}_{ij}^T), \quad (13.15)$$

$$\partial\boldsymbol{F}(t) = \partial\boldsymbol{F}^{\parallel}(t) + \partial\boldsymbol{F}^{\perp}(t) = [\boldsymbol{e}_{ij} \cdot \partial\boldsymbol{F}(t)]\,\boldsymbol{e}_{ij} + (\mathbb{1} - \boldsymbol{e}_{ij}\boldsymbol{e}_{ij}^T)\partial\boldsymbol{F}(t), \quad (13.16)$$

with $\boldsymbol{e}_{ij} = \boldsymbol{R}_{ij}(t)/R_{ij}(t)$. For simplicity, only the parallel component for the distance-deponent memory kernels $\boldsymbol{K}^{\mathrm{p}}(R_{ij}(t),t')$ and $\Delta\boldsymbol{K}^{\mathrm{s}}(R_{ij}(t),t')$ is considered in this thesis. In Ref. 5 we have shown *via* theory and simulations that the orthogonal component is indeed much smaller than the parallel component. Additionally, the single-particle self-memory kernel $K_{\alpha\beta}^{\mathrm{s}}(t) = K^{\mathrm{s}}(t)\delta_{\alpha\beta}$ is assumed to be isotropic.

To perform generalized Brownian dynamics simulations, the remaining challenge is to calculate the correlated random force $\boldsymbol{F}_{i,n}^R$ following the fluctuation-dissipation theorem Eq. (13.13).

13.2 Calculating time- and cross-correlated random numbers

In this section, we will first introduce the Fourier transform technique to determine time-correlated random numbers. This method was proposed by Barrat *et al.*[143] and applied in several publications.[83;108;109] In the second subsection, the technique is generalized to include cross-correlations between the random numbers, which then enables the inclusion of pair-memory kernels.

13.2.1 The Fourier transform technique

This section is reproduced from Appendix A of the publication "Iterative reconstruction of memory kernels", Gerhard Jung, Martin Hanke and Friederike Schmid, *Journal of Chemical Theory and Computation*, **13**, 2481 (2017).

The goal is to generate time-correlated Gaussian distributed random numbers F_n, that fulfill the correlation function

$$\langle F_{n+m}F_n \rangle = K_m, \tag{13.17}$$

with the discretized memory sequence K_m for $m = 0, ..., T - 1$, where T denotes the number of time steps for which the memory is considered. First, we introduce the real parameter α_s for $s = -T + 1, ..., T - 1$, defined by

$$K_m \equiv \sum_{s=-T+1}^{T-1} \alpha_s \alpha_{s+m}, \tag{13.18}$$

with $\alpha_{s+m} = \alpha_{s+m-2T+1}$ if $s + m \geq T$. It can now be shown that for a sequence of uncorrelated Gaussian distributed random numbers W_n, the relation

$$F_n = \sum_{s=-T+1}^{T-1} \alpha_s W_{n+s} \tag{13.19}$$

generates random numbers with the target correlation function. The challenge therefore lies in the determination of the parameter α_s. This can be achieved by applying the discrete Fourier transform (DFT) to the memory sequence,

$$\hat{K}_\omega = \sum_{m=-T+1}^{T-1} K_m e^{-i\omega m \frac{2\pi}{2T-1}}, \tag{13.20}$$

with $K_{-m} = K_m$. We will now define

$$\hat{\alpha}_\omega = \sqrt{\hat{K}_\omega}, \tag{13.21}$$

and consequentially determine the parameter α_s by inverse DFT,

$$\alpha_s = \frac{1}{2T-1} \sum_{\omega=-T+1}^{T-1} \hat{\alpha}_\omega e^{i\omega s \frac{2\pi}{2T-1}}. \tag{13.22}$$

It is straightforward to show that the definitions in Eqs. (13.18) and (13.21) are consistent. We close with one important comment: In practical applications, a small number of coefficients $\hat{K}_\omega$ was slightly below zero. While this is theoretically impossible, because the modes connected to the negative values $\hat{K}_\omega$ would be instable, the problem can occur due to discretization errors if the memory sequence K_m has "edges". The solution used in this thesis is to set all values $\hat{K}_\omega < 0$ to zero. Although this leads to very small deviations from the FDT ($\approx 0.01\%$), the difference did not have any physical consequences.

13.2.2 Generalized Fourier transform technique

Different than in the previous subsection, the stochastic forces will now also be cross-correlated. This can be described by considering random numbers $F_{i,n}$ for every particle $i = 1, ..., N$ and time step n. The generalized correlation function that has to be fulfilled is

$$\langle F_{i,n+m} F_{j,n} \rangle = K_{ij,m}. \tag{13.23}$$

Here, every entry (i, j) of the $N \times N$-dimensional matrix $\mathcal{K}_m$ is a discretized self- or pair-memory kernel. We then introduce the real and symmetric $N \times N$-dimensional matrices $\mathcal{A}_s$ for $s = -T + 1, ..., T - 1$, defined by

$$\mathcal{K}_m \equiv \sum_{s=-T+1}^{T-1} \mathcal{A}_s \mathcal{A}_{s+m}, \tag{13.24}$$

where $\mathcal{A}_{s+m} = \mathcal{A}_{s+m-2T+1}$ if $s + m \geq T$. The correlated random numbers $\mathcal{F}_n$ can now be determined by multiplying these matrices with a sequence of uncorrelated Gaussian distributed random numbers $\mathcal{W}_n$,

$$\mathcal{F}_n = \sum_{s=-T+1}^{T-1} \mathcal{A}_s \mathcal{W}_{n+s}. \tag{13.25}$$

Similar to the previous section, the difficulty is to find an algorithm that efficiently determines the matrices $\mathcal{A}_s$. The solution proposed in this thesis is combining the Fourier transform technique and the Lanczos algorithm[148–150] to efficiently determine the matrix square root. To derive the final algorithm, we first Fourier transform Eq. (13.24) by utilizing the convolution theorem,

$$\hat{\mathcal{K}}_\omega = \hat{\mathcal{A}}_\omega \hat{\mathcal{A}}_\omega \tag{13.26}$$

$$\Rightarrow \hat{\mathcal{A}}_\omega = \sqrt{\hat{\mathcal{K}}_\omega}, \tag{13.27}$$

with the Fourier transforms of the memory matrix $\hat{\mathcal{K}}_\omega$, and the convolution matrix $\hat{\mathcal{A}}_\omega$, according to Eq. (13.20). This result can now be applied on the Fourier transform of Eq. (13.25),

$$\hat{\mathcal{F}}_\omega = \sqrt{\hat{\mathcal{K}}_\omega} \hat{\mathcal{W}}_\omega. \tag{13.28}$$

Here, $\hat{\mathcal{F}}_\omega$ and $\hat{\mathcal{W}}_\omega$ are the Fourier transforms of the correlated and uncorrelated noise vector, respectively. This equation shows that is not necessary to calculate the full square root matrix within cubic time, but only to determine the square root matrix multiplied by a vector. This operation can be performed within linear time using the Lanczos algorithm[148–150] if it is assumed that the particle interaction has a cutoff r_c. This linear time complexity is obviously the best possible scaling that can be achieved for the given problem. The main idea behind the Lanczos algorithm is to determine the eigenvalues of a given matrix by projection on Krylow subspaces. In

---

Algorithm 1 Generating correlated random numbers $F_{i,n}$ following the distribution $\langle F_{i,n+m}F_{j,n}\rangle = K_{ij,m}$

1: **Inputs:**

      $K_{ij,m}$ for $m = 0, ..., T-1$ with $K_{ij,m} = K_{ij,-m}$

      $W_{i,n}$ with $\langle W_{i,n+m}W_{j,n}\rangle = \delta_{m0}\delta_{ij}$

2: **Initialize:**

      compute $\hat{K}_{ij,\omega} = \sum_{m=-T+1}^{T-1} K_{ij,m}\exp(-\mathrm{i}m\omega\frac{2\pi}{2T-1})$

      compute $\hat{W}_{i,\omega} = \sum_{m=-T+1}^{T-1} W_{i,n+m}\exp(-\mathrm{i}m\omega\frac{2\pi}{2T-1})$

3: **for** $\omega = 0$ to $T-1$ **do**

4:     set $v_i^0 = 0$, $\beta^0 = 0$, $v_i^1 = \hat{W}_{i,\omega}/\|\hat{\boldsymbol{W}}_\omega\|$, $k = 1$, $\Delta = 1$

5:     compute $\alpha^1 = v_i^1 \hat{K}_{ij,\omega}v_j^1$

6:     **while** $\Delta > tol$ **do**

7:         compute $r_i^{k+1} = \hat{K}_{ij,\omega}v_j^k - \alpha^k v_i^k - \beta^{k-1}v_i^{k-1}$

8:         set $\beta^k = \|\boldsymbol{r}^{k+1}\|$

9:         set $v_i^{k+1} = r_i^{k+1}/\beta^k$

10:        compute $\alpha^{k+1} = v_i^{k+1}\hat{K}_{ij,\omega}v_j^{k+1}$

11:        define $V_{ip}^{k+1} = v_i^p$, $p = 1, ..., k+1$

12:        construct tridiagonal H_{pq}^{k+1} with diagonal elements equal to $(\alpha_1, ..., \alpha_{k+1})$ and super- and sub-diagonal elements equal to $(\beta_1, ..., \beta_k)$

13:        compute $\boldsymbol{x}^{k+1} = \|\hat{\boldsymbol{W}}_\omega\|\boldsymbol{V}^{k+1}\sqrt{\boldsymbol{H}^{k+1}}\boldsymbol{e}^0$, with $e_1^0 = 1$ and $e_q^0 = 0$, $q = 2, ..., k+1$

14:        set $\Delta = \|x^{k+1} - x^k\|$

15:        set $k = k+1$

16:     **end while**

17:     set $\hat{F}_{i,\omega} = x_i^k$

18: **end for**

19: compute $F_{i,n} = \frac{1}{T}\left(\hat{F}_{i,0} + 2\sum_{\omega=1}^{T-1}\hat{F}_{i,\omega}\right)$

---

our case, the projection is performed on symmetric, tridiagonal matrices. For these tridiagonal matrices there are, however, simple and fast techniques to determine their square root.[151] Therefore, the Lanczos algorithm can also be used for the approximate determination of the square root matrix.

The pseudo code to determine auto- and cross-correlated random numbers using the methods described above is displayed in Algorithm 1. For practical applications several comments about the algorithm have to be made:

- If there is a clear separation between the typical diffusion times of the coarse-grained particles and the time scale of the memory, Eq. 13.13 can be simplified to

$$\langle \boldsymbol{F}_{i,n+m}^{\mathrm{R}}\boldsymbol{F}_{j,n}^{\mathrm{R}}\rangle = k_{\mathrm{B}}Ta_m\boldsymbol{K}_m^{\mathrm{p}}(R_{ij,n})/\Delta t. \tag{13.29}$$

This enables the precalculation of the Fourier transform of the memory kernels (step 2).

- In step 19, we only evaluate the correlated random numbers $F_{i,n}$ and not the full inverse Fourier transform of $\hat{F}_{i,\omega}$. Considering the time scale separation from the previous comment it could also be possible to introduce a time-window T_{FT} for which the correlated random numbers $F_{i,n+m}$ for $m = 0, ..., T_{\mathrm{FT}} - 1$ are determined. This would lead to a speed up of approximately T_{FT}.

- The bottleneck of this method is the matrix-vector multiplication (steps 5,7,10). The results of steps 5 and 10 are therefore saved and reused in step 7.

- In our implementation, the most efficient way to perform the matrix-vector multiplication is by looping over the neighbor lists in every iteration step. Using sparse-matrix multiplication leads to a very time consuming overhead.

- The square root of the matrix $\boldsymbol{H}^{k+1}$ in step 13 can be evaluated easily by realizing that $\boldsymbol{H}^{k+1}$ is a real, symmetric and tridiagonal matrix (see Ref. 151).

- If the system can be described by the self-memory kernel only, it is possible to use the algorithm presented in Section 13.2.1. Therefore, the parameters for the noise calculation can be precalculated before the simulation run, which significantly increases the efficiency (see Ref. 83).

In Fig. 13.1 the time-correlation functions of the stochastic force determined for an exemplary system are shown. The system consists of four particles sitting in the edges of a square with edge length $7\,\sigma$. The input memory kernel will be derived in Chapter 14. The exit condition was set to $tol = 0.0001$ (see Algorithm 1). The figure clearly shows that the time-correlation functions of the random force perfectly match the input memory kernels. The presented simulation includes both distance-dependent self-memory kernels and projections, due to the two-dimensionality of the system; these results are therefore highly non-trivial. For example, the memory
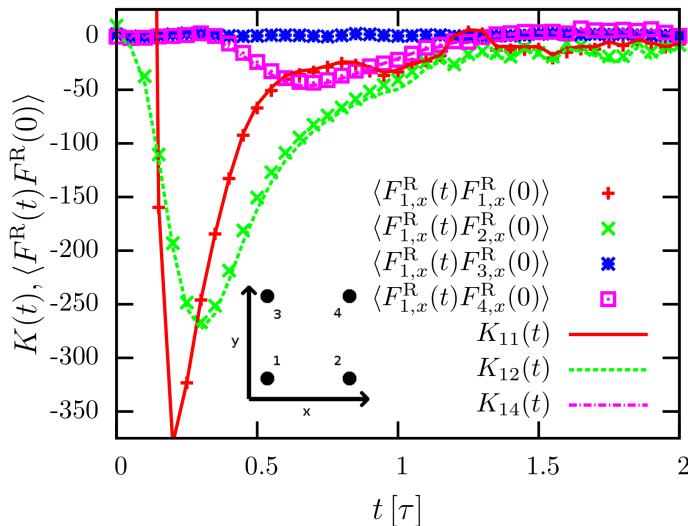

Figure 13.1: Auto- and cross-correlation functions of the stochastic force $F^{\mathrm{R}}(t)$ produced using Algorithm 1. The figure shows the simulated time-correlation functions (data points) along with the input memory kernels (lines). The simulated system consists of four particles sitting at the edges of a square with edge length $7\,\sigma$ (see black sketch).

kernel $K_{14}(t)$ is given by,

$$K_{14}(t) = 0.5K(R = 9.8\,\sigma, t), \tag{13.30}$$

because particle 1 and 4 have a distance $R = 9.8\,\sigma$ and the projection on the x-axis includes a factor of 0.5 (see Eq. (13.15) and sketch in Figure 13.1).

This analysis shows that the algorithm presented in this section precisely calculates stochastic forces with the desired correlation functions. Therefore, we finally have developed a systematic method to integrate the generalized Langevin equation with pair-memory kernels. In the next chapter, this generalized Brownian dynamics technique will be applied to investigate the frequency-dependent hydrodynamic interactions between nanocolloids in dispersion.

Generalized Brownian Dynamics Applied to Nanocolloids

The dynamics of colloids in dispersion are strongly influenced by their hydrodynamic interactions. In Chapters 3, 5 and 12 we have already extensively discussed the self-interaction of colloids, which is dominated by hydrodynamic backflow. Additionally, the flow field that is induced by the movement of each colloid will lead to frequency-dependent hydrodynamic pair-interactions between different colloids. These pair-interactions play an important role for many processes in soft matter physics on very different length and time scales.[27;152;153] As a consequence, various methods have been proposed to include them into coarse-grained models.[105;114;116;123–125] The most efficient ones are implicit solvent models, in which the solvent particles are replaced by effective equations of motion for the dissolved particles.[123–125] However, in the literature it is always assumed that there exists a time scale separation between the relaxation of the particles and the dynamics of the solvent, i.e., hydrodynamic interactions are mediated instantaneously. In Ref. 5 we have already shown that this approximation is not valid for nanocolloids and that the hydrodynamic interactions are characterized by significant memory effects in two-particle systems (see also Chapter 3). In this thesis we use the methods proposed in the previous chapters to determine and implement these pair-memory effects into an implicit solvent model based on the multiparticle generalized Langevin equation. This means that we set up a coarse-grained system of N freely diffusing particles that are supposed to have the exact same dynamics as the nanocolloids in the underlying microscopic system.

In the first section of this chapter, we derive the distance-dependent memory kernels that describe the hydrodynamic interaction of nanocolloids under the assumption that many-body effects do not play a role. This can be done very efficiently using a trick introduced in Ref. 5. With this approach, the two-particle GLE can be decomposed into two GLEs without pair-interactions and modified dynamics. Afterwards, we use the determined memory kernels as input to perform generalized Brownian dynamics (GBD) simulations in combination with the IMRV to account for many-body effects. In the third section, the transferability of the determined memory kernels is investigated. This already gives some insights into the applicability of the GBD technique. Finally, we make some important remarks on the efficiency of the technique as well as on the inclusion of long-range interactions and long-time tails to the non-Markovian coarse-grained model that is constructed in this chapter.

14.1 Constructing non-Markovian coarse-grained models in the highly dilute limit

In this section we will utilize the auto- and cross-correlation functions determined from multiparticle MD simulations to determine the self- and pair-memory kernels in the highly dilute limit. To do so, we consider the generalized Langevin equation (13.1) for two particles within a constant distance R in the absence of a conservative force, $\mathbf{F}^{\mathrm{C}}(t) = 0$. We therefore assume that the hydrodynamic interactions are purely additive and many-body effects do not have an impact on the dynamical correlation functions. Under these assumptions, the equation of motion for particle 1 is

$$M\dot{V}_1(t) = - \int_0^t \mathrm{d}s \big(K^{\mathrm{s}}(t-s) + \Delta K^{\mathrm{s}}(R, t-s) \big) V_1(s) - \int_0^t \mathrm{d}s K^{\mathrm{p}}(R, t-s) V_2(s) + \partial F_1(t).$$
(14.1)

Since we only consider the contributions parallel to the line-of-centers between the two particles, this problem is effectively one-dimensional. By multiplying Eq. (14.1) with $V_1(0)$ and taking the time-average, this equation can be transformed into a noise-free differential equation for the velocity auto- and cross-correlation functions,

$$M\dot{C}_{11}(R, t) = - \int_0^t \mathrm{d}s \big(K^{\mathrm{s}}(t-s) + \Delta K^{\mathrm{s}}(R, t-s) \big) C_{11}(R, s) - \int_0^t \mathrm{d}s K^{\mathrm{p}}(R, t-s) C_{21}(R, s),$$
(14.2)

with $C_{ij}(R, t) = \langle V_i(t) V_j(0) \rangle_{R_{12}=R}$. An analogous equation can be derived by multiplication of Eq. (14.1) with $V_2(0)$. Under the justified assumption that $C_{11}(R, t) = C_{22}(R, t)$ and $C_{12}(R, t) = C_{21}(R, t)$, we can combine these two equations and derive decoupled GLEs with modified dynamics,

$$M\dot{C}_{\pm}(R, t) = - \int_0^t \mathrm{d}s K_{\pm}(R, t - s) C_{\pm}(R, s).$$
(14.3)

Here, we introduce the additive and subtractive velocity correlation functions $C_{\pm}(R, t) = C_{11}(R, t) \pm C_{12}(R, t)$ and memory kernels $K_{\pm}(R, t) = K^{\mathrm{s}}(t) + \Delta K^{\mathrm{s}}(R, t) \pm K^{\mathrm{p}}(R, t)$, respectively. This equation motivates the following coarse-graining procedure to derive a first approximation for the distance-dependent self- and pair-memory kernels:

- Perform a molecular dynamics (MD) simulation of freely diffusing particles and determine the velocity auto- and cross-correlation functions,

$$C^{\mathrm{a}}(R, t) = \frac{1}{2N(N-1)} \sum_{i,j \neq i} \langle V_i(t) V_i(0) + V_j(t) V_j(0) \rangle_{R_{ij}(t)=R}, \qquad (14.4)$$

$$C^{\mathrm{c}}(R, t) = \frac{1}{2N(N-1)} \sum_{i,j \neq i} \langle V_i(t) V_j(0) + V_j(t) V_i(0) \rangle_{R_{ij}(t)=R}. \qquad (14.5)$$

These functions describe the velocity auto- and cross-correlations of particle i under the assumption that there exists a particle j in distance R. In these definitions it is assumed that the distance does not change significantly on the time scale on which the velocity correlation functions decay. The correlation functions are binned with a spatial discretization ΔR, which is equivalent to the binning of the memory kernels (see also next paragraph).

- Determine the additive and subtractive velocity correlation functions $C_{\pm}(R,t)$ and utilize the iterative memory reconstruction to derive the memory kernels $K_{\pm}(R,t)$. This reconstruction is very efficient, since it does not require to consider cross-correlations between the particles.

- Calculate the self- and pair-memory kernels,

$$K^{\mathrm{s}}(t) + \Delta K^{\mathrm{s}}(R,t) = \frac{K_+(R,t) + K_-(R,t)}{2}, \tag{14.6}$$

$$K^{\mathrm{p}}(R,t) = \frac{K_+(R,t) - K_-(R,t)}{2}, \tag{14.7}$$

and determine the distance-dependent correction $\Delta K^{\mathrm{s}}(R,t)$ by subtracting the known single-particle memory $K^{\mathrm{s}}(t)$ (see Chapter 12).

Step 2 can also be performed with the inverse Volterra technique[92] (as is done in Ref. 5). However, for the simulations considered in this thesis, the results of the inverse Volterra technique are much less accurate than the results obtained with the IMRV method. The reason for this observation are accumulated errors in the inverse Volterra technique for large correlation times that can be traced back to the significant statistical errors of the MD cross-correlation functions. This shows that the IMRV method is indeed more robust than the other non-iterative techniques.

Figure 14.1 illustrates the iterative memory reconstruction for the additive and subtractive memory kernels. The underlying MD simulation model consists of 125 nanocolloids with box size $L = 107.728\,\sigma$, corresponding to a number density $\rho = 0.0001\,\sigma^{-3}$ and thus a volume fraction of $1\,\%$ (see also Chapter 3). The time step of the GLE simulations is $\Delta t = 0.05\,\tau$. The cutoff of the memory sequence is $T = 50$, which leads to the memory time scale $\tau_{\mathrm{mem}} = 2.5\,\tau$. The spatial discretization is $\Delta R = 0.2\,\sigma$, with a cutoff $r_{\mathrm{c}} = 15\,\sigma$. Determining the mean velocity $v = \sqrt{M^{-1}} \approx 0.1\,\sigma/\tau$ for $k_{\mathrm{B}}T = 1\,\epsilon$ reveals that the particles roughly diffuse over a distance ΔR on a time scale τ_{mem}. It can thus be assumed that the distance-dependent memory kernels change only slightly on this time scale. Therefore, the assumptions made for the discretization of the GLE in the last chapter are fulfilled. This also enables, amongst others, the precalculation of the Fourier transform of the memory kernels (see Algorithm 1). If not stated differently, the same system properties are used for all simulations in the next sections. Figure 14.1 clearly shows that the final results for the memory kernels perfectly reproduce the target velocity correlation functions (bottom panel).
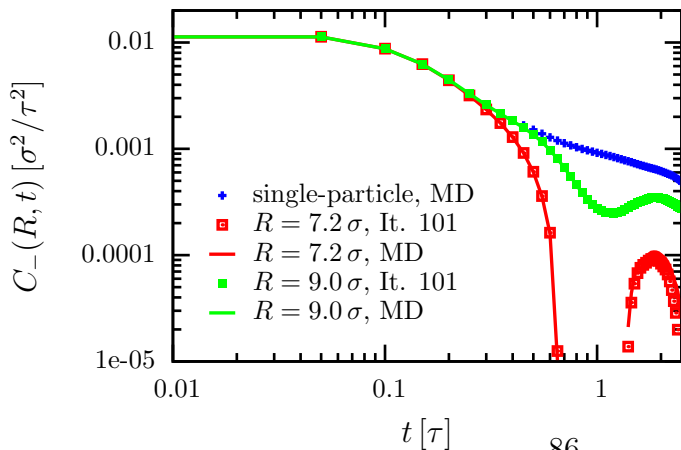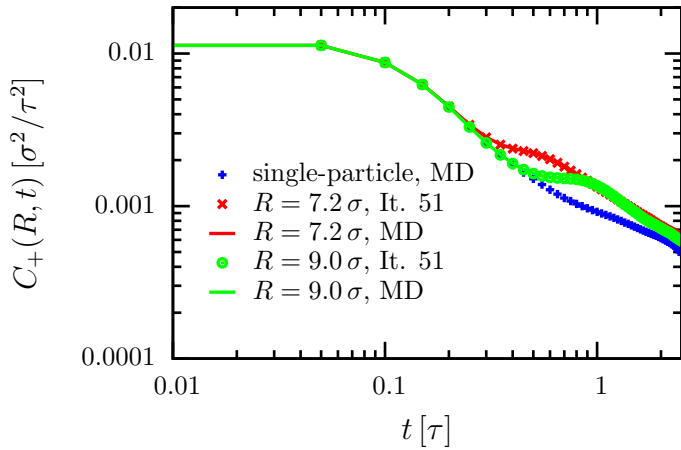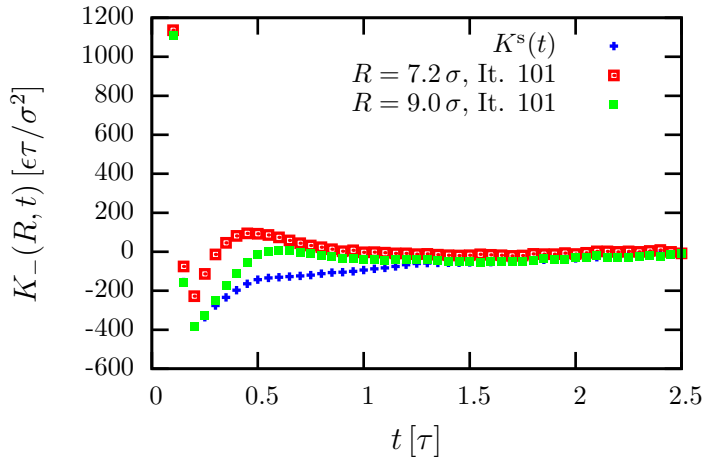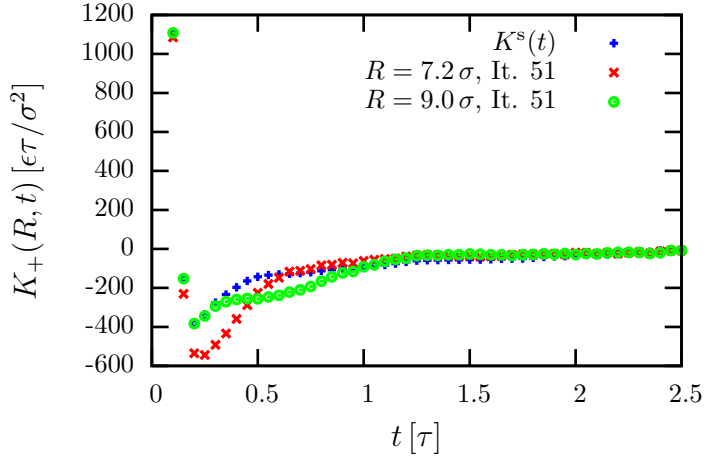
Figure 14.1: Iterative memory reconstruction of the additive and subtractive memory kernels. The reconstruction is shown for the distances $R = 7.2\,\sigma$ and $R = 9\,\sigma$. All reconstructions are initialized with the memory kernel $K^{\mathrm{s}}(t)$ that was determined in Chapter 12. The reconstruction time step is $\Delta t = 0.05\,\tau$ and the correction times are $t_{\mathrm{cor}}^{+} = 0.1\,\tau$ and $t_{\mathrm{cor}}^{-} = 0.05\,\tau$.

The two upper figures show the reconstructed memory kernels for different iteration steps, compared to the single-particle self-memory kernel (see Chapter 12).

The two lower figures visualize the velocity correlation functions used to correct the memory kernels in each iteration step, compared to the single-particle auto-correlation function. The final results lie exactly on top of the MD reference simulations. The negative values in the curve "$C_{-}(R,t) : R = 7.2\,\sigma$, It. 101" are not shown.

Figure 14.2 visualizes many-body effects in the hydrodynamic interactions by comparison between the generalized Brownian dynamics simulation using the memory kernels derived in this section and the original MD simulation. While the velocity cross-correlation function shows a good agreement, there are significant deviations between the velocity auto-correlation function observed in GBD and MD simulations. Here, the figure shows that the velocity decorrelation is substantially overestimated in GBD for both distances R. This can be explained as follows: The disturbance of the flow field caused by the movement of nearby colloids leads to a strong decorrelation of the velocity, because the backflow effect is reduced. In the two-body reconstruction performed in this section, the decorrelation is attributed to one neighboring colloid in the distance R only, instead of the set of all nearby colloids. This leads to an overestimation of the distance-dependent self-memory correction $\Delta K^{\mathrm{s}}(R,t)$ and thus to the observed discrepancies between the coarse-grained model and the microscopic system.

To account for these many-body effects it is inevitable to perform generalized Brownian dynamics simulations and use the iterative memory reconstruction to correct the differences between the GBD and MD results.
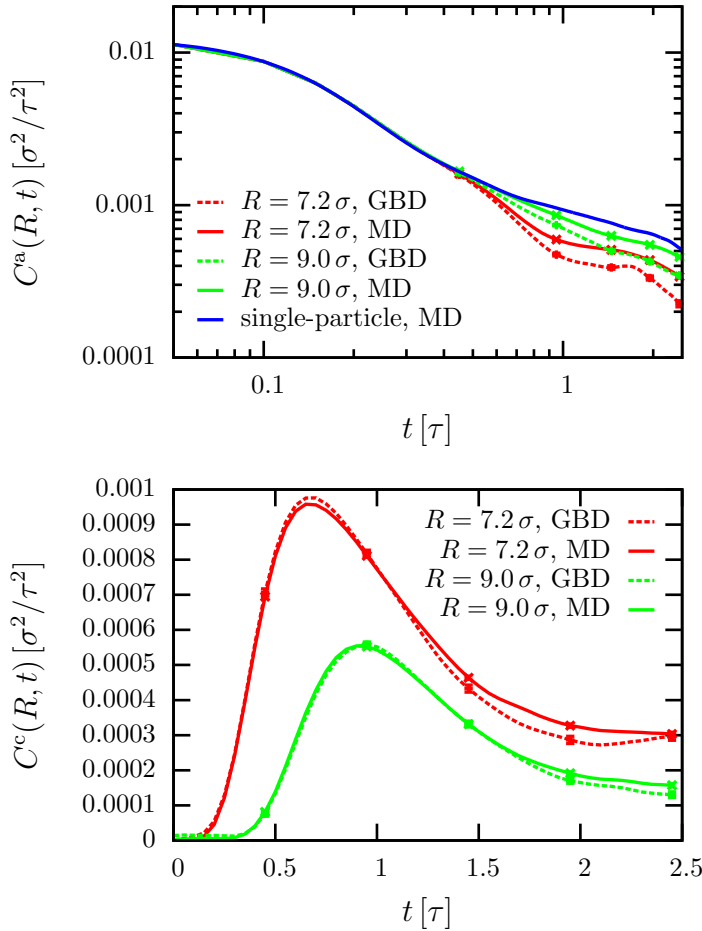
Figure 14.2: Generalized Brownian dynamics (GBD) simulations of nanocolloids in dispersion. The input memory kernels are determined in Section 13.1. The figures show results for the velocity auto- (upper figure) and cross- (lower figure) correlation functions for distances $R = 7.2\,\sigma$ and $R = 9.0\,\sigma$, compared to molecular dynamics (MD) simulations. To visualize the statistical errors, five data points with y-error bars are included in the curves.

14.2 Accounting for many-body effects in non-Markovian coarse-grained models

In this section the IMRV is applied to reconstruct the frequency-dependent hydrodynamic interactions between freely diffusing nanocolloids in many-body systems. The reconstruction of $C^{\mathrm{a}}(R,t)$ and $C^{\mathrm{c}}(R,t)$ is performed in parallel for all distances R, however, the corrections in every iteration step are determined separately, without considering correlations between different distances. Similar to the observation discussed in the last section, this will lead to an overshooting in the corrected memory kernels. Therefore, a regularization parameter α is included as prefactor to the mapping function $\phi_2(Y)$ (see Tab. 12.1). Additionally, we use the first derivative of the velocity correlation functions as correction to the memory kernels, to avoid the emergence of a linear-in-time increasing difference between the GBD and MD correlation functions, as discussed in Chapter 12. The mapping function for the IMRV is thus

$$\phi_2'(Y) = -\alpha\beta M^2 \frac{Y(t+\Delta t) - Y(t)}{\Delta t^2}, \tag{14.8}$$

with $\alpha \approx 0.3$, $\beta = 1/k_{\mathrm{B}}T$ and the respective velocity correlation function Y. Additionally we need to point out that we focus in the present work on the hydrodynamic regime in which at least a few solvent particles are located between the surfaces of the colloids, i.e., we disregard lubrication forces in the GBD simulations. This is done by including a lower cutoff $r_{\mathrm{c,min}} = 6.8\,\sigma$ to the memory kernels. For distances $R < 6.8\,\sigma$, the memory kernels are thus replaced by the ones at $R = r_{\mathrm{c,min}}$. The exclusion of lubrication forces has two reasons: The statistical errors of the correlation functions for small distances are very large because the number of neighbors N_{neigh} at a distance R of a colloid obviously scales quadratically with R. Additionally, the radial distribution function is strongly decreasing for $R < 6.8\,\sigma$, therefore, the quality of the reproduced memory kernels would be poor. The lubrication forces also lead to very strong cross-correlations between the particles that are difficult to handle within the assumptions made in this thesis, like, for example, that the memory kernels are approximately constant on the memory time scale τ_{mem}.

The iterative procedure is illustrated in Figure 14.3. The reconstruction time step is $\Delta t = 0.05\,\tau$ and $t_{\mathrm{cor}} = 0.05\,\tau$. Iterations $101-200$ correspond to an iterative reconstruction initialized with the final memory kernels of the first reconstruction (It. $0-100$). The figure shows that the auto- and cross-correlation functions converge. As mentioned in the last section, the cross-correlation functions already agree very well even without the inclusion of many-body contributions. The only significant deviations between the different iteration steps can thus be observed for $R = 7.2\,\sigma$ and $t > 1.0\,\tau$. The picture changes when analyzing the iterative reconstruction for the distance-dependent auto-correlation function. Here, the
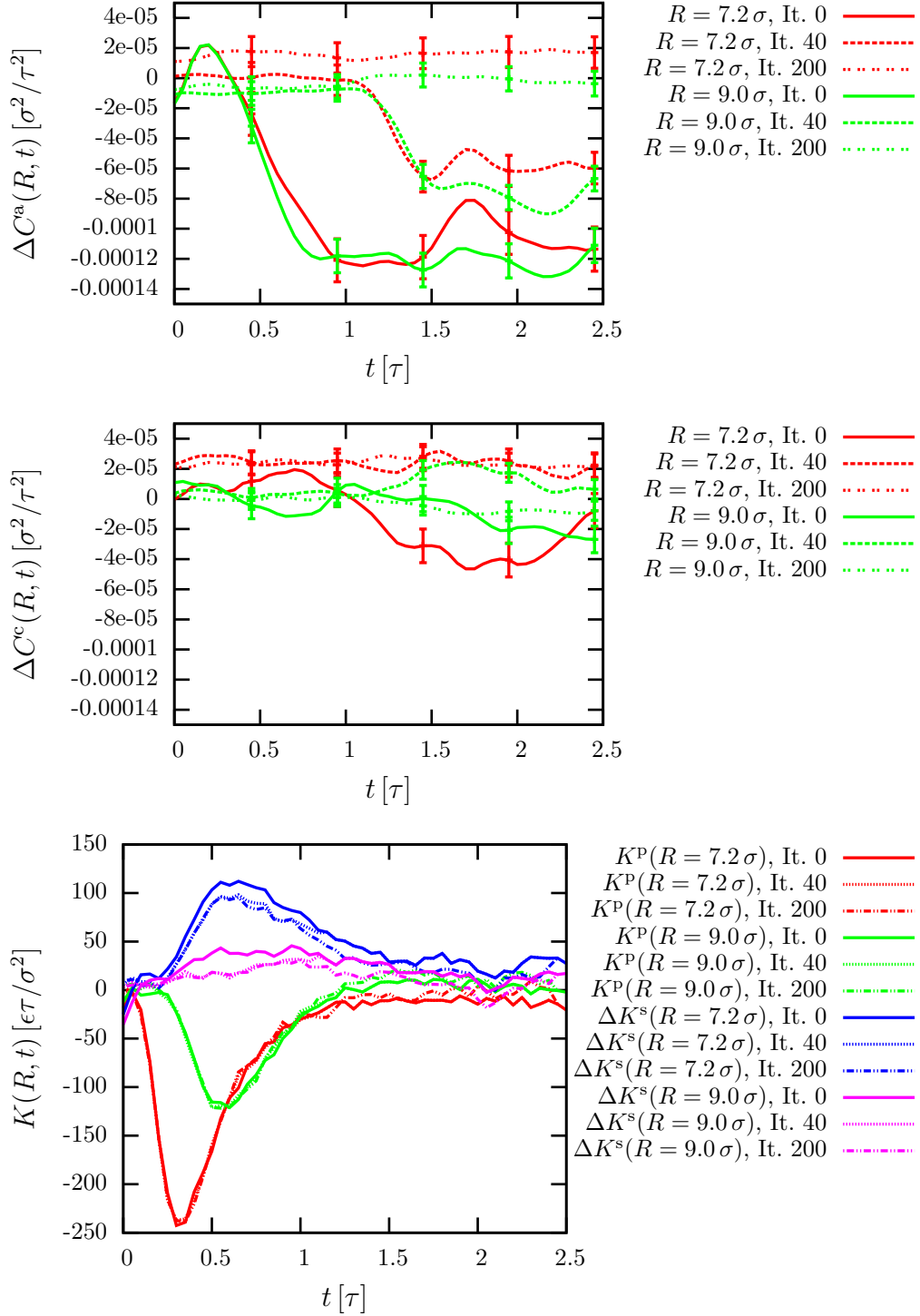
Figure 14.3: IMRV applied to the nanocolloidal dispersion to derive the hydrodynamic self- and pair-memory kernels. Simulation results for different iteration steps are shown for particle distances $R = 7.2\,\sigma$ and $R = 9\,\sigma$. The upper and middle figure illustrate the difference between the velocity auto- (upper) and cross- (middle) correlation function determined from GBD and MD simulations ($\Delta C(t) = C_{\text{GBD}}(t) - C_{\text{MD}}(t)$). To visualize the statistical errors, five data points with y-error bars are included in the curves. The lower figure shows the self- and pair-memory kernels.

former discrepancies between GBD and MD simulations almost completely vanish and a good agreement between the correlation functions can be achieved, especially for larger distances. Therefore, we have reconstructed distance-dependent memory kernels for non-Markovian coarse-grained models that almost perfectly describe the short-range hydrodynamic interactions of freely diffusing nanocolloids in dispersion. It is worth emphasizing that the difference between the coarse-grained model and the original MD simulation can easily become larger than the statistical error of the correlation functions. This is due to the fact that we do not use the absolute value of this difference to correct the memory kernel, but the first derivative (see Eq. 14.8). As a consequence, the statistical errors of the determined correlation functions accumulate with increasing correlation time t and thus increase with the square root of the correlation time, $\Delta C(t) \propto \sqrt{t}$. The straightforward way to minimize this discrepancy is performing longer coarse-grained simulations and thus reduce the statistical error.

The reconstructed memory kernels are illustrated in the lower panel of Figure 14.3. It can be observed that the final memory kernels calculated in this section significantly differ from the results of the previous section (see curves labeled "It. 0" in Figure 14.3). Especially the overestimation of the distance-dependent self-memory kernel was corrected, i.e., $\Delta K^{\mathrm{s}}(R, t)$ was reduced. However, despite the reduction of $\Delta K^{\mathrm{s}}(R, t)$, this distance-dependent correction to the single-particle self-memory kernel still considerably differs from zero, which retrospectively justifies its introduction in Chapter 13.

Figure 14.4 shows the auto- and cross-correlation functions determined from GBD simulations using these reconstructed memory kernels for various distances R. The results confirm all observations made in the previous paragraph. In particular, the discrepancies in the velocity auto-correlation function are removed and a perfect agreement between GBD and MD simulations is achieved. The only differences can be observed for small distances $R < 8.0\,\sigma$. However, the statistical error of these small-distance correlation functions is relatively large. These uncertainties in the determination of the correlation function will thus reduce the quality of the reproduced memory kernels.

The final results for the hydrodynamic self- and pair-memory kernels are presented in Figure 14.5 and compared to results from fluid dynamics (see Chapter 3). The agreement between theory and simulations for the pair-memory kernel $K^{\mathrm{p}}(R = 9.0\,\sigma, t)$ is very good. For smaller distances, significant deviations can be observed, which are caused by the approximate nature of the theory in the case of $R \approx 2R_{\mathrm{c}}$, with the radius of the colloid R_{c}, as discussed in Ref. 5. The situation is different for the distance-dependent correction to the self-memory kernel, $\Delta K^{\mathrm{s}}(R, t)$. The figure shows that this correction is substantially underestimated by the theory for all distances R. This could have three reasons: Firstly, this contribution is strongly affected by the boundary-conditions of the colloids, because it depends on the precise
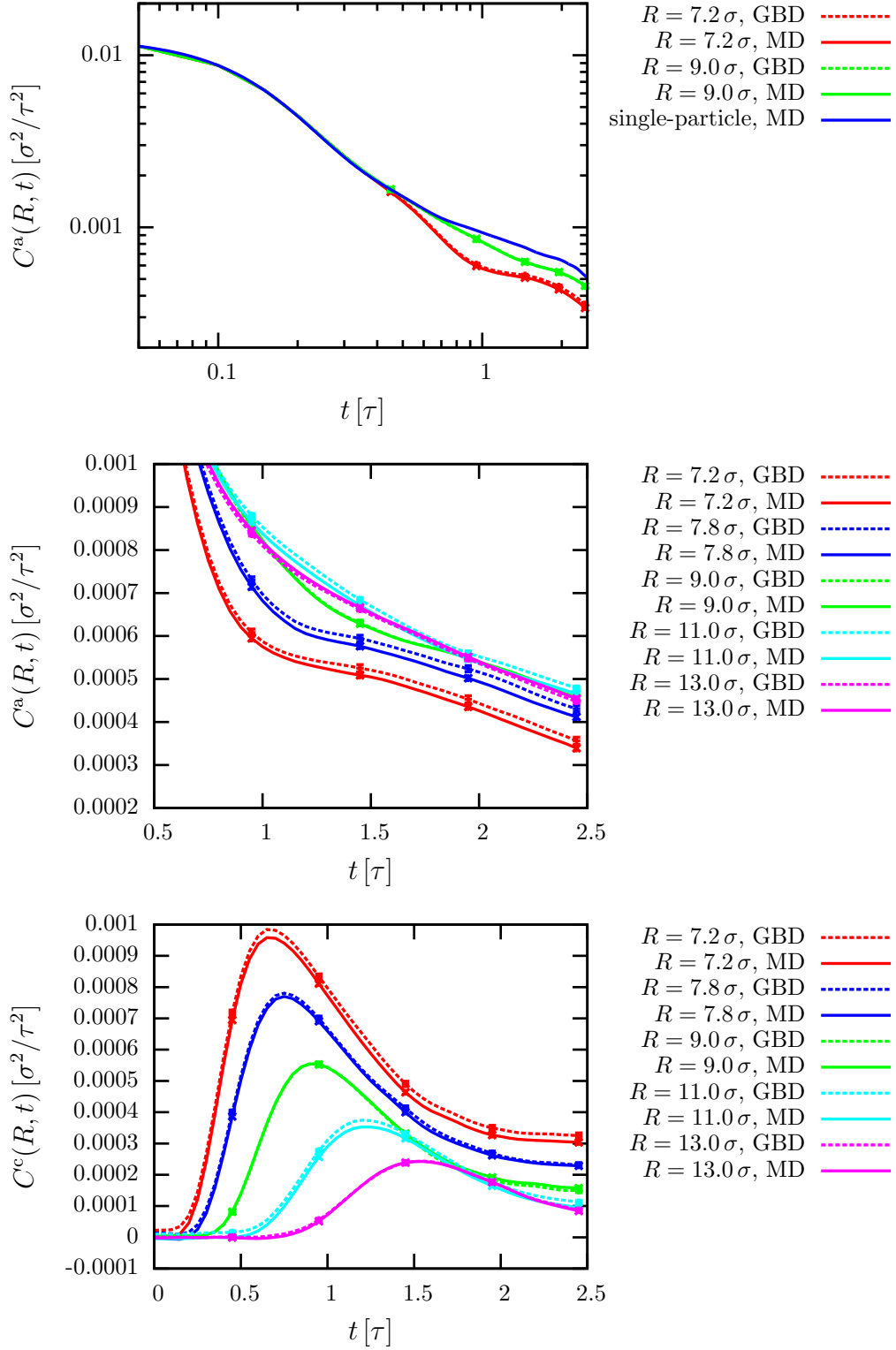
Figure 14.4: Hydrodynamic auto- and cross-correlation functions of nanocolloids in dispersion for different particle distances R. The presented results relate to the non-Markovian coarse-grained model derived in Section 14.2 simulated with generalized Brownian dynamics (GBD) and compared to results from molecular dynamics (MD). The upper and middle figure illustrate the velocity auto-correlation function in double-logarithmic (upper) and zoomed linear (lower) representation. The lower figure shows the velocity cross-correlation function. To visualize the statistical errors, five data points with y-error bars are included in the curves.
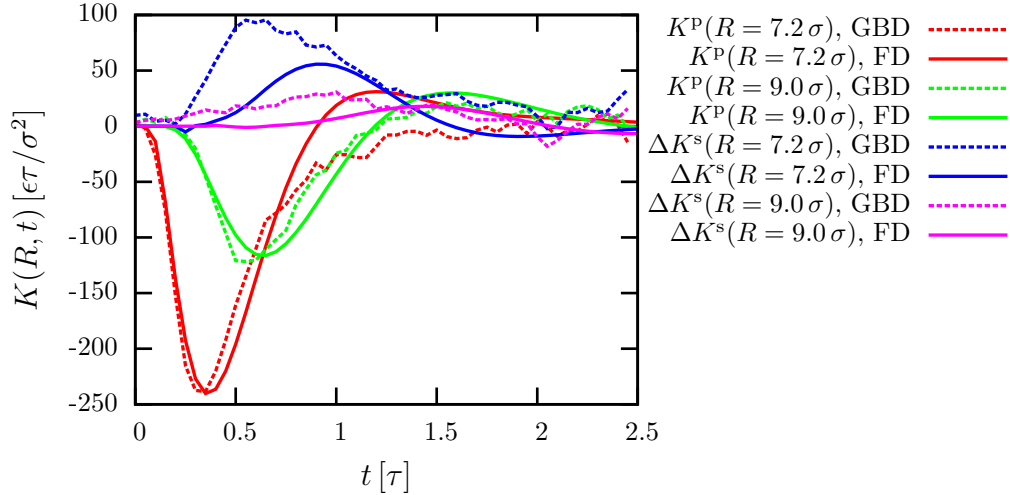
91

Figure 14.5: Hydrodynamic self- and pair-memory kernels of nanocolloids in dispersion for different particle distances R. The figure shows the distance-dependent self- and pair-memory kernels of the non-Markovian coarse-grained model derived in Section 14.2, compared to results from fluid dynamics (FD, see Chapter 3).

reflection of the sound wave that transmits the hydrodynamic interaction between two colloids. Since this reflection cannot be modeled in full detail in hydrodynamic theory, we expect deviations between theory and simulations. Secondly, the high-frequency response of the hydrodynamic interactions is influenced by the particle character of the fluid in MD simulations that cannot be described by continuum fluid dynamics. Thirdly, as discussed in this section, the distance-dependent correction $\Delta K^{\mathrm{s}}(R,t)$ is affected by many-body contributions that are not integrated in the theory.

In this section we have shown that the generalized Brownian dynamics technique can be used to construct non-Markovian coarse-grained models that have exactly the same dynamical properties as the underlying microscopic model. An important property for the applicability of these coarse-grained models is their transferability, which will be investigated in the next section.

14.3   Transferability of memory kernels

To study the transferability of the non-Markovian coarse-grained model describing the frequency-dependent hydrodynamic interactions of nanocolloids, we investigate the dependence of the dynamical correlation functions on the nanocolloid density ρ. We therefore perform GBD simulations with the self- and pair-memory kernels derived in the previous section for various densities ρ. The results are presented in Figure 14.6. The density-dependence of the velocity correlation functions in the microscopic system is small and thus not shown in the plot. The figure illustrates that the reduction of the density in the GBD simulations has only a small effect
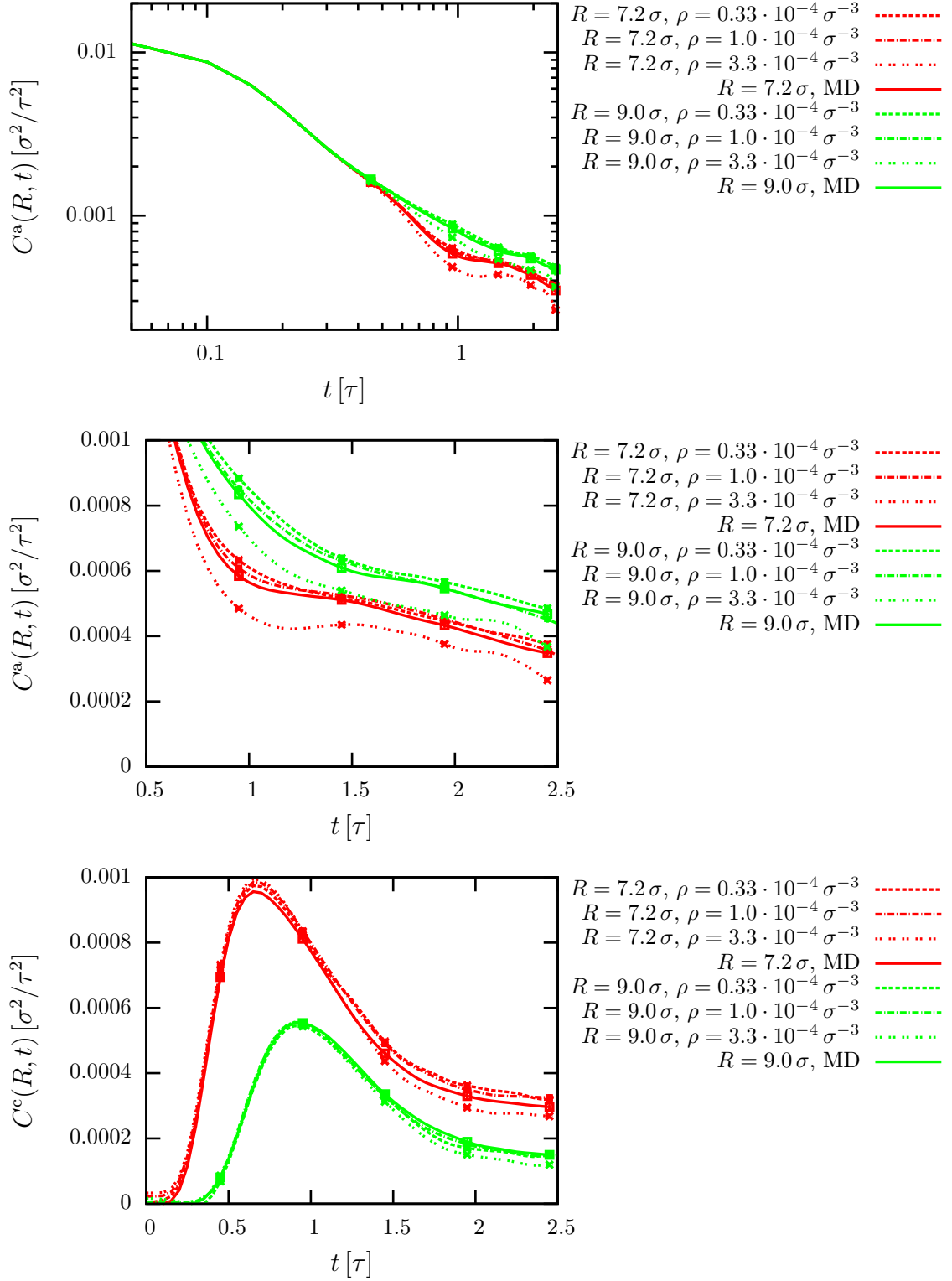
Figure 14.6: Hydrodynamic auto- and cross-correlation functions of nanocolloids in dispersion for different particle distances R. The presented results use the memory kernels derived in Section 14.2 to perform generalized Brownian dynamics (GBD) simulations for various nanocolloid densities ρ. The upper and lower figure illustrate the velocity auto- (upper) and cross- (lower) correlation function determined from GBD and molecular dynamics (MD) simulations. The density-dependence of the MD results is small and thus only one representative curve for $\rho = 10^{-4}\,\sigma^{-3}$ is shown. To visualize the statistical errors, five data points with y-error bars are included in the curves.

on the velocity correlation functions. This is a very important result, because it justifies the approach used in Chapter 13. On the other hand, the figure also shows that the approach has its limitations. When substantially increasing the density, significant differences in the correlation functions emerge. The reason for this is the approximate nature of the self-memory kernel,

$$K_i^{\text{self}}(\{\boldsymbol{R}_i\}, t) = K^{\text{s}}(t) + \sum_j \Delta K^{\text{s}}(\boldsymbol{R}_{ij}, t), \tag{14.9}$$

as defined in Chapter 13. The consequence of this definition is that the contribution of all particles within the cutoff r_{c} are added up to yield the density-dependent self-diffusion of particle i. If there are many colloids within the neighborhood of particle i, this leads to an unrealistic strong decorrelation as visualized in the figure. Therefore, the observed discrepancy is caused by many-body effects that go beyond the many-body corrections applied in Section 14.2. The transferability of the proposed technique is therefore limited to densities $\rho < 5.0 \cdot 10^{-4}\,\sigma^{-3}$. For even higher densities $\rho \gtrsim 10^{-3}\,\sigma^{-3}$, an increasing amount of interaction matrices is not positive-definite (see Section 13.1), which could lead to inconsistent results, since the fluctuation-dissipation theorem is not fulfilled. However, it should be emphasized that the cross-correlations considered in this thesis are very strong due to the small bulk viscosity and high sound velocity of the Lennard-Jones fluid (see Appendix A). In most applications, we thus expect that this upper density should not be the limiting factor of the GBD method.

The above analysis demonstrates that the non-Markovian coarse-grained models integrated with the generalized Brownian dynamics technique are indeed applicable to a large range of nanocolloid densities ρ. The memory kernels derived in this chapter thus indeed describe the fundamental hydrodynamic self- and pair-interactions between the nanocolloids. This is a crucial conclusion: using the iterative memory reconstruction one can construct coarse-grained models with the correct dynamical properties, without necessarily capturing the underlying physical features of the system. This can for example occur if the set of relevant dynamical variables chosen for the derivation of the generalized Langevin equation was not optimal (see also Section 5.2).

14.4   Final remarks

As a first remark, we present the benchmarks of the GBD simulations (see Tab. 14.1). The table shows that the speedup of the non-Markovian coarse-grained model is obviously strongly dependent on the density of the simulated system. This makes sense because MD systems with higher densities contain fewer solvent particles. Additionally, the number of neighbors in the GBD simulations is increased. Therefore, the speedup of the systems considered in this thesis ranges

Simulation technique	$\rho \, [\sigma^{-3}]$		
	$0.33 \cdot 10^{-4}$	$1.0 \cdot 10^{-4}$	$3.3 \cdot 10^{-4}$
MD	$61000 \pm 2000\,\mathrm{s}$	$19500 \pm 750\,\mathrm{s}$	$6400 \pm 100\,\mathrm{s}$
GBD	$60 \pm 1\,\mathrm{s}$	$63 \pm 1\,\mathrm{s}$	$145 \pm 1\,\mathrm{s}$
CG MD	$0.35 \pm 0.01\,\mathrm{s}$	$0.56 \pm 0.01\,\mathrm{s}$	$1.19 \pm 0.02\,\mathrm{s}$

Table 14.1: Benchmarks of the generalized Brownian dynamics (GBD) technique compared to molecular dynamics (MD) simulations for different nanocolloid densities ρ. The coarse-grained (CG) MD results refer to simulations using only the mean force $F^{\mathrm{C}}(R)$, determined in Chapter 5. The simulations correspond to 125 nanocolloids integrated for 10^4 time steps, with time step $\Delta t_{\mathrm{MD}} = 0.001\,\tau$ and $\Delta t_{\mathrm{GBD,CG\text{-}MD}} = 0.05\,\tau$. The benchmarks were run on the Mogon I cluster (`https://mogonwiki.zdv.uni-mainz.de/dokuwiki/nodes`) using 1 core on an "AMD Opteron 6272" CPU.

from $S_{\mathrm{u}} = 1017\Delta t_{\mathrm{GLE}}/\Delta t_{\mathrm{MD}} = 5.1 \cdot 10^4$ (for $\rho = 0.33 \cdot 10^{-4}\,\sigma^{-3} \,\widehat{=}\, 0.33\,\%$ volume fraction), to $S_{\mathrm{u}} = 44\Delta t_{\mathrm{GLE}}/\Delta t_{\mathrm{MD}} = 0.2 \cdot 10^4$ (for $\rho = 3.3 \cdot 10^{-4}\,\sigma^{-3} \,\widehat{=}\, 3.3\,\%$ volume fraction). The most meaningful benchmark perhaps is the comparison between the GBD simulations and a corresponding coarse-grained model integrated without memory kernels (labeled as CG MD in Tab. 14.1). Here, a constant slowdown of $S_{\mathrm{d}} = 150$ can be observed. This slowdown is thus the consequence of the inclusion of corrected dynamics using the generalized Langevin equation.

Since hydrodynamic interactions are long-range and governed by long-time tails, it is obviously not possible to model them in full detail with the methods derived in this thesis. The only technique known in the literature to deal with the long-range nature of hydrodynamic (or Coulomb) interactions is Ewald summation,[120] which determines the long-range contributions in reciprocal space. Due to the non-Markovian nature of the memory kernels, this technique cannot be straightforwardly adapted to the generalized Langevin equation. We therefore expect that the main applications of the methods proposed in this thesis will be connected to short-range interactions like frequency-dependent dipole interactions (see also Part II) or potentially active particles with non-instantaneous local reorientations. However, the short-range hydrodynamic interactions between nanocolloids are a perfect model system for the exemplary application of the proposed techniques, since they exhibit pronounced memory effects that can be analyzed by theory and simulations. In order to consider the long-range nature of hydrodynamic interactions it is possible to combine the generalized and the standard Brownian dynamics technique. The former is applied for the frequency-dependent short-range interactions, $R < r_{\mathrm{c}}$, between the particles to model the high-frequency response of the colloids. The latter includes long-range interactions, $R > r_{\mathrm{c}}$, using Ewald summation to ensure consistency with the long-range nature of the microscopic interactions. It might even be possible to combine Ewald summation and GBD under the assumption $\boldsymbol{K}(R > r_{\mathrm{c}}, t) = \boldsymbol{K}(R = r_{\mathrm{c}}, t)\Phi(R)$. This, however, goes beyond the scope of this work.

Another important remark concerns the long-time tails of the velocity correlation functions. For computational reasons it is necessary to cutoff the memory kernel after a time τ_{mem} (see Chapter 13). This will, however, always lead to deviations between the GBD and MD simulations on time scales larger than the memory time scale, $t > \tau_{\mathrm{mem}}$ (see Appendix E). One possibility to circumvent this problem is the introduction of an auxiliary variable expansion that is discussed in Appendix D. In this expansion, the memory kernels are basically approximated by exponential functions. While it is obviously still not possible to represent the long-time tails in full detail, this expansion would at least guarantee some kind of continuity in the correlation functions.

An important impact of the short-range pair memory effects derived in this chapter compared to instantaneous friction constants is the precise modeling of the sound wave that mediates the interaction between two colloids. In standard Brownian dynamics simulations, two approaching colloids would just feel an increase of the friction force that decelerates the particles. The correlation between the particles would, however, decrease rapidly, similar to the decorrelation shown in Figure E.1 for $t > \tau_{\mathrm{mem}}$. In contrast, the pair-memory kernel leads to a time-delayed interaction due to the finite propagation velocity of the sound wave. Subsequently, the sound wave leads to a long-time correlation between the velocities of the particles, which has positive sign and thus indicates that the particles move into the same direction. One consequence of this memory effect is that two particles are less likely to approach each other. Additionally, the propagated sound wave will be reflected and interacts with other colloids which leads to more realistic collective dynamics.

With the coarse-graining techniques developed in this chapter we are now able to systematically investigate these memory effects and include them into non-Markovian coarse-grained models. The methods proposed in this thesis therefore open up new ways for dynamical coarse-graining and for understanding dynamical processes in soft matter physics.

15

Conclusions and Outlook

In the main part of this thesis we introduced two fundamentally new techniques for dynamic coarse-graining. Firstly, we proposed the iterative reconstruction of memory kernels (IMR). The purpose of this method is solving the inverse problem of calculating the memory kernel that generates a given time-correlation function. The IMR is inspired by the iterative Boltzmann inversion, an algorithm to approach a similar inverse problem known from the field of static coarse-graining. The strength of our reconstruction in comparison to previously proposed techniques is its applicability to many-body simulations and its inherent ability of constructing coarse-grained models that have precisely the same dynamical features as the underlying microscopic system. Secondly, we developed the generalized Brownian dynamics (GBD) technique to integrate these non-Markovian coarse-grained models. GBD is based on a discretization of the generalized Langevin equation including distance-dependent self- and pair-memory kernels. This allows for a precise definition of the detailed dynamical properties of a coarse-grained model by specifically tuning the frequency-dependent self- and pair-interactions of the particles. We presented a combined application of both techniques to derive the short-range frequency-dependent hydrodynamic interactions of nanocolloids in dispersion. The self-interactions of these nanocolloids is governed by the hydrodynamic backflow effect, i.e., the movement of the colloids induces fluid vortices that affect their dynamics at later times. On the other hand, the hydrodynamic pair-interactions between different colloids are dominated by sound waves that are generated by one colloid and transmitted by the fluid to interact with another colloid. The reconstructed non-Markovian coarse-grained model is able to precisely reproduce these very different dissipative interactions. Additionally, the model was shown to be very efficient with a speedup of up to $S_{\mathrm{u}} = 10^4$ and transferable to various nanocolloid densities ρ.

Like every scientific work this thesis poses as many new challenges as it has solved. Although we have very well understood the iterative reconstruction technique from an application-oriented view, it is not fully clear why and under which circumstances the iteration converges. In particular, the necessity of introducing a time-dependent regularization is not clear. Since this regularization strongly affects the performance of the algorithm, we plan to collaborate with mathematicians to get better insight into the method and thus further increase the efficiency of the reconstruction. Another open problem is the construction of an auxiliary variable system that

describes the same generalized Langevin equation as considered in this thesis. One possible technique known from numerical analysis is the construction of hidden Markov models. This approach might be more promising than the *a posteriori* fitting procedures used in the literature to construct Markov models, since the latter is not generalizable to distance-dependent self- and pair-memory kernels. In general, the construction of non-equilibrium coarse-grained models first requires a deeper understanding of the Mori-Zwanzig formalism in non-equilibrium situations. One fundamental principle of this work was for example the fluctuation-dissipation theorem, which is not valid anymore in systems out of equilibrium.

The above list of possible future research, in combination with the considerations made in the previous chapter, shows that the field of dynamic coarse-graining is still in the early stages of development. However, there are already many possible applications for non-Markovian coarse-grained modeling in the emerging fields of active particles and dynamic self-organization. More generally, the methods presented in this thesis could be important for systems that are strongly defined by their dynamical properties. This includes in particular the field of non-equilibrium soft matter physics. We therefore suspect that in the near future an increasing effort will be put into dynamic coarse-graining. Without any doubt many exciting new techniques and applications will emerge and we thus hope that the presented methods will be useful in future research.

A

About Reduced Units and Mapping to Realistic Systems

All physical quantities in this thesis are given in reduced Lennard-Jones units. This unit system consists of four independent units, which are the units of energy ϵ, length σ, time τ and charge e. Since the coarse-grained models do not have a direct connection to an atomistic system, there is no *a priori* conversion between the reduced unit system and SI units. It is, however, possible to map the simulations onto a specific microscopic system and in this way estimate the values of the reduced units. In the following, this mapping will be performed individually for the polyelectrolyte in ionic solution and the colloidal suspension.

A.1 Reduced units of the polyelectrolyte in ionic solution

The polyelectrolyte in ionic solution has several important quantities that should be similar to the experimental system. The viscosity η of the DPD fluid describes the hydrodynamic interactions in the fluid and therefore the convection of the ions. The Debye length λ_D determines the relevant length scale on which the electrostatic interactions are screened. Additionally, we want to ensure room temperature. These considerations lead to the following mapping from the reduced units system to SI units:

- The viscosity η of the DPD fluid corresponds to $1\,\mathrm{mPa \cdot s}$ (the viscosity of water).

- The Debye screening length $\lambda_D = 1.78\,\sigma$ corresponds to $3\,\mathrm{nm}$ (the approximate screening length of the ionic solution used in Ref. 45).

- The charge e corresponds to the elementary charge $e = 1.6 \cdot 10^{-19}\,C$.

- The temperature $T = \epsilon/k_\mathrm{B}$ corresponds to $295\,\mathrm{K}$.

Red. units	SI units (see Sec. A.1)
σ	$1.69 \cdot 10^{-9}\,\mathrm{m}$
ϵ	$4.05 \cdot 10^{-21}\,\mathrm{J}$
τ	$9.2 \cdot 10^{-10}\,s$
e	$1.6 \cdot 10^{-19}\,C$

Table A.1: Mapping of reduced LJ units to SI units for the polyelectrolyte in ionic solution studied in this thesis.

	DNA model	Real DNA[45;59]
Basepairs [bp]	50-500	120-164000
Charge per basepair $[e]$	0.1	2

Table A.2: Comparison of our model DNA to experimental values of real DNA. The mapping was performed according to Tab. A.1

The results of the mapping can be found in Tab. A.1. It can be observed that the time scale τ corresponds to about $1\,\mathrm{ns}$ and the length scale σ is approximately $1.7\,\mathrm{nm}$. The mapping therefore shows that we are indeed performing coarse-grained simulations, since one DPD particle represents several fluid molecules.

The conversion from reduced to SI units now allows us to compare the DNA model used in our simulations to real DNA (see Tab. A.2). First, it can be noticed that one coarse-grained bead in the polyelectrolyte corresponds to about 5 basepairs ($d_{\mathrm{bp}} \approx 0.34\,\mathrm{nm}$). The system considered in this thesis thus contains DNA with about $50 - 500$ basepairs which is much smaller than the standardly investigated DNA samples in experiments. This length and time scale separation between simulations and experiments is a typical problem in soft matter physics. The charges on the DNA are also differently distributed and the total charge of the model DNA is much smaller than the one of real DNA. Due to the coarse-grained nature of the model, it is not possible to obtain a 1:1 correspondence between the model and the microscopic system. The largest impact of this difference is the change of the Manning parameter $\gamma_0 = \lambda_{\mathrm{B}}/l_{\mathrm{c}}$,[133;154–157] where l_{c} is the distance between neighboring charged monomers. This parameter gives a rough approximation of the amount of counterions that will condense on the polyelectrolyte. For values $\gamma_0 < 1$, very few counterions are expected to condense while larger values indicate a strong condensation. The Manning parameter for the DNA is $\gamma_{0,\mathrm{DNA}} = 4.2$, and for the model used in this thesis it is $\gamma_{0,\mathrm{PE}} = 0.5$. The two-state categorization into condensed and "free" counterions is, however, much debated for ionic solutions with a significant salt concentration.[133;158;159] In the present work we therefore use the term "condensed counterions" to denote low-mobility counterions in close vicinity to the polyelectrolyte (Stern layer), without strictly referring to Manning-type condensation.

Red. units	SI units	Dysthe et al.[160]
σ	$0.29 \cdot 10^{-9}\,\mathrm{m}$	$0.29 \cdot 10^{-9}\,\mathrm{m}$
ϵ	$4.0 \cdot 10^{-21}\,\mathrm{J}$	$5.5 \cdot 10^{-21}\,\mathrm{J}$
τ	$8.0 \cdot 10^{-13}\,s$	-

Table A.3: Mapping of the reduced units describing the colloidal suspension studied in this thesis to water. The results are compared to the triple point mapping performed in Ref. 160. Table adapted from Ref. 5.

	LJ fluid	Water ($30\,°\mathrm{C}$)
Shear viscosity η $[\epsilon\tau/\sigma^3]$	2.11	6.23
Bulk viscosity ζ $[\epsilon\tau/\sigma^3]$	0.88	18.69
Speed of sound c_0 $[\sigma/\tau]$	5.63	4.05

Table A.4: Transport coefficients and speed of sound of the colloidal suspension compared to water at room temperature. The mapping of units was performed according to Tab. A.3. Table adapted from Ref. 5.

A.2 Reduced units of the colloidal suspension

To study the hydrodynamic interactions between colloids, we model a colloidal suspension using spherical hard-core particles in a LJ fluid. To compare the simulation results to experimental systems, we map the LJ fluid to water. The following assignments are performed:

- The mass m of a LJ particle corresponds to $18\,u$ (the mass of a water molecule).

- The mass density of the LJ fluid corresponds to $1000\,\mathrm{kg/m^3}$ (the density of water).

- The temperature $T = \epsilon/k_\mathrm{B}$ corresponds to $300\,\mathrm{K}$.

The results of this mapping are presented in Tab. A.3. Compared to the conversion derived in the previous section, the degree of coarse-graining is much smaller in this system. The length scale σ is related to the mean distance between two water molecules and the time scale τ corresponds to just one picosecond. Applying this mapping to compare the transport coefficients in the LJ fluid to water reveals that the systems are indeed qualitatively comparable (see Tab. A.4). The speed of sound that determines the propagation of the longitudinal waves and therefore the time scale of the hydrodynamic interactions is actually very similar in the two systems. The most significant difference can be observed for the bulk viscosity ζ. However, this value just determines the damping of the sound waves and has therefore only a qualitative influence on the results presented in Chapter 14.

B

Non-Equilibrium Molecular Dynamics (NEMD)

In this chapter, the non-equilibrium molecular dynamics (NEMD) technique is discussed. Contrary to the Green-Kubo relations that are applied in equilibrium (see Chapters 2 and 11) in the NEMD method a non-equilibrium steady-state is created. This enables the direct calculation of the transport coefficients, e.g., by measuring the steady-state momentum flux in the system. The advantage compared to Green-Kubo relations is that these methods are not restricted to the linear response regime and therefore enable the study of non-linear phenomena like shear thinning or thickening, i.e., the shear-rate dependence of the shear viscosity η. Several techniques have been proposed to utilize NEMD for the determination of the shear viscosity.[9–13] In Section B.1, the momentum interchange method, proposed by Müller-Plathe,[11] will be explained. In this technique the simulation box is divided into different slabs that can interchange the momentum of their respective particles. In this way, a linear shear-flow is created very efficiently.

The determination of the bulk viscosity ζ *via* NEMD is, however, more difficult. This can be explained by the fact that the bulk viscosity is related to the deformation of the volume of a fluid element and thus to a change of the local thermodynamic state of the system. The only available NEMD calculations of the bulk viscosity use either cyclic compression[18] or the relaxation of an instantaneous distortion.[161;162] The methods used in these studies cannot be applied to systems with stochastic dynamics – either because they are explicitly designed for Hamiltonian systems,[18;162] or, in the case of Ref. 161, because they cannot be used to determine the instantaneous contribution of the random force to the viscosity. In addition to the above mentioned calculations, there have been extensive NEMD studies of the elongational viscosity using the so called SLLOD[a] equations of motion.[164] This boundary-driven NEMD method does not rely on Hamiltonian dynamics and it should be possible to generalize it to include dissipative and stochastic forces. However, it is necessary to choose a

---

[a]The abbreviation SLLOD comes from the close relationship to Doll's equations of motion, introduced by Hoover in Ref. 163.

vanishing strain rate in order to minimize the change of volume. In Section B.2, we will therefore propose two new techniques to create a steady-state compressible flow and determine the bulk viscosity ζ. One, denoted "particle transfer method", creates a divergent flow field by manually displacing particles. This method is most efficient for systems with particles interacting *via* soft potentials. The other technique, denoted "force-driven method", makes use of a spatially varying body force and a non-zero center-of-mass velocity and can be used in a wider range of molecular dynamics simulations.

B.1   NEMD simulations creating shear flow

If a shear flow $\partial_z u_x$ emerges in a fluid, it will be damped due to shear viscosity η. This damping can be described by a momentum flux

$$j_z(p_x) = -\eta \frac{\partial u_x}{\partial z}, \tag{B.1}$$

which transports momentum p_x in $-z$-direction. To maintain the shear flow it is thus necessary to counteract the damping by enforcing a similar momentum flux in $+z$-direction. The idea of the momentum interchange method[11] is to produce this counter flux by swapping the momentum of particles with a certain rate. This is done in three steps (see Figure B.1, right panel):

1. Choose the particle with the highest velocity in $+x$-direction in the middle slab.

2. Choose the particle with the highest velocity in $-x$-direction in the top slab.

3. Swap the momentum of these two particles.

The shear rate $\dot{\gamma} = \partial_z u_x$ will depend on the rate of these momentum interchange steps and the velocity profile will be linear in good approximation if the interchange rate is not too large (see Figure B.1, left panel). By calculating the momentum flux

$$j_z(p_x) = \frac{P_x}{2TA} = \frac{\sum_{\{i\}} m \Delta v_i}{2TA}, \tag{B.2}$$

with P_x the total momentum exchange during the simulation, simulation time T and area $A = L_x L_y$, the shear viscosity can be determined using Eq. B.1.
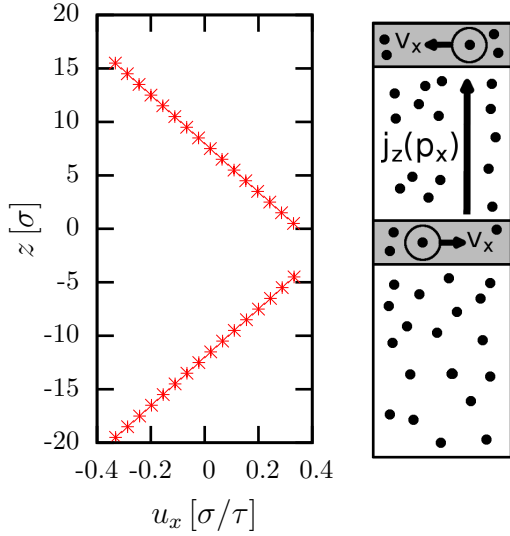
Figure B.1: Momentum interchange method to generate steady-state shear flow. Right panel illustrates the idea of the method. Left panel shows the emerging shear profile of a DPD fluid with density $\rho = 4\,\sigma^{-3}$. Figure adapted from Ref. 17.

B.2   NEMD simulations creating compressible flow

Unfortunately, the momentum interchange method cannot be used to create a steady-state *divergent* flow, with gradient $\partial_x u_x$. This is because the transported momentum p_x and the direction of flux $j_x(p_x)$ are no longer orthogonal. In fact, the directions of particle and momentum transport are parallel and therefore a transport of *particles* is necessary to maintain the steady-state. This can be achieved in two different ways: either by manually displacing particles or by imposing a global flow. Our two methods of generating steady-state divergent flow are based on these two types of mass transport.

The methods can be motivated theoretically by solving the mass and momentum continuity equations with appropriate source terms (see also Chapter 2). The local conservation of mass on a continuum level with source term is

$$\partial_t \rho + \nabla \cdot (\rho \boldsymbol{u}) = Q_\rho(\boldsymbol{r}), \tag{B.3}$$

with density $\rho(\boldsymbol{r}, t)$, velocity field $\boldsymbol{u}(\boldsymbol{r}, t)$ and mass source term $Q_\rho(\boldsymbol{r})$. Similarly one can write down the local conservation of momentum,

$$\partial_t(\rho \boldsymbol{u}) + \nabla(\rho \boldsymbol{u} \otimes \boldsymbol{u}) + \nabla \boldsymbol{\sigma} = Q_\rho(\boldsymbol{r}) \boldsymbol{u} + \boldsymbol{f}(\boldsymbol{r}), \tag{B.4}$$

with the external force field $\boldsymbol{f}(\boldsymbol{r})$ and the constitutive relation[2]

$$\boldsymbol{\sigma}(\boldsymbol{r}, t) = p\boldsymbol{I} + \left(\frac{2}{3}\eta - \zeta\right) \nabla \cdot \boldsymbol{u}\boldsymbol{I} - \eta\left(\nabla \boldsymbol{u} + \nabla \boldsymbol{u}^T\right). \tag{B.5}$$

To this point, these equations are similar to the conservation laws introduced in Chapter 2 with the inclusion of mass and momentum source terms. These sources can be chosen freely and allow us to manipulate the flow and density profiles. However, to conserve global mass and momentum both the mass source term $Q_\rho(\boldsymbol{r})$

and the force field $\boldsymbol{f}(\boldsymbol{r})$ must fulfill the relations

$$\int_V Q_\rho(\boldsymbol{r})\mathrm{d}\boldsymbol{r} = 0, \tag{B.6}$$

$$\int_V \boldsymbol{u}(\boldsymbol{r})Q_\rho(\boldsymbol{r})\mathrm{d}\boldsymbol{r} + \int_V \boldsymbol{f}(\boldsymbol{r})\mathrm{d}\boldsymbol{r} = 0. \tag{B.7}$$

In the following, we assume that the fluid is barotropic, i.e., there exists a unique relation $p = P(\rho)$. We are interested in stationary solutions $\partial_t\rho = 0$ and $\partial_t(\rho\boldsymbol{u}) = 0$, where $\boldsymbol{u} = u\boldsymbol{e}_x$ exhibits a gradient in x-direction and profiles are constant in all other directions. Assuming that higher order derivatives of the flow field can be neglected, we obtain the following equations,

$$Q_\rho(x) = \partial_x(\rho u), \tag{B.8}$$

$$f(x) = -Q_\rho(x)u + P'(\rho)\partial_x\rho + \partial_x(\rho u^2). \tag{B.9}$$

B.2.1 Particle transfer method

In the particle transfer method, we aim at creating a velocity gradient while keeping the density profile constant, $\rho(x) = \bar{\rho}$. This leads to,

$$Q_\rho(x) = \bar{\rho}u'(x), \tag{B.10}$$

$$f(x) = \bar{\rho}\,u\,u'(x). \tag{B.11}$$

To get a linear profile $u(x) = \epsilon\,|x|$, one therefore has to choose a mass source term,

$$Q_\rho(x) = \bar{\rho}\,\epsilon\,\mathrm{sign}(x), \tag{B.12}$$

and a force field $f(x) = \bar{\rho}x\epsilon^2 \approx 0$ which vanishes at order $\mathcal{O}(\epsilon)$. These source terms can be realized by transferring particles between two halves of the box at a certain rate (see Fig. B.2). The algorithm is very simple:

1. Choose a random particle in the right half of the simulation box.

2. Place it at a random position in the left half of the simulation box.

This algorithm conserves momentum and – in the special case of vanishing conservative forces – also energy. As shown in Fig. B.2, the resulting velocity profile is approximately linear and the density profile almost constant, in perfect agreement with the above described theoretical prediction. Therefore, this algorithm is perfectly suitable to study the bulk viscosity ζ of fluids that are interacting only via soft potentials, like the DPD fluid studied in Chapter 11 (see also results in Fig. 11.2). However, the particle transfer method can become problematic in the presence of hard-core potentials, like the widely used Lennard-Jones potential, because particle insertion in dense fluids is difficult and usually associated with large energy penalties.
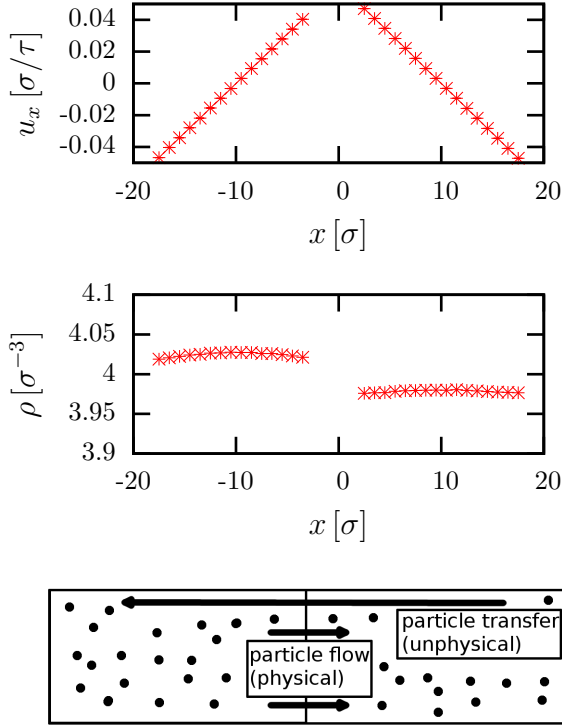
Figure B.2: Particle transfer method to generate steady-state divergent flow. Bottom panel illustrates the idea of the method. Upper panels show the emerging velocity profile (top) and density profile (middle) of a DPD fluid with density $\rho = 4\,\sigma^{-3}$. Figure adapted from Ref. 17.

B.2.2 Force-driven method

In the force-driven method there is no particle transfer and hence no mass source term, $Q_\rho(\boldsymbol{r}) = 0$. This directly leads to $\rho u = $ const. A velocity gradient is invariably associated with a density gradient and can only exist if the mean velocity $\bar{u}$ is nonzero. The force density is now

$$f(x) = -\frac{\rho}{u}(P'(\rho) - u^2)\, u'(x). \tag{B.13}$$

To create a linear profile $u(x) = \bar{u} + \epsilon\,|x|$, one therefore has to apply an external force

$$f(x) = -\epsilon\, C\, \mathrm{sign}(x) + \mathcal{O}(\epsilon^2), \tag{B.14}$$

where the constant C is given by $C = (P'(\bar\rho)\,\bar\rho/\bar{u} - \bar\rho\,\bar{u})$. These equations explain how to create a linear velocity profile in the absence of a mass source term: One has to create a steady-state particle flow in the presence of periodic boundary conditions by imposing a non-zero center-of-mass velocity. To create a divergent flow field, one has to combine this global background flow with an external force acting on all particles, which changes sign between the two halves of the box (see Fig. B.3). This method has the advantage that one does not have to manually change the position of particles. It can thus be used in combination with hard-core potentials. It is also physically more "realistic" since it only requires an external force and a non-zero flow velocity. Therefore, the basic idea might be applicable in experiments.
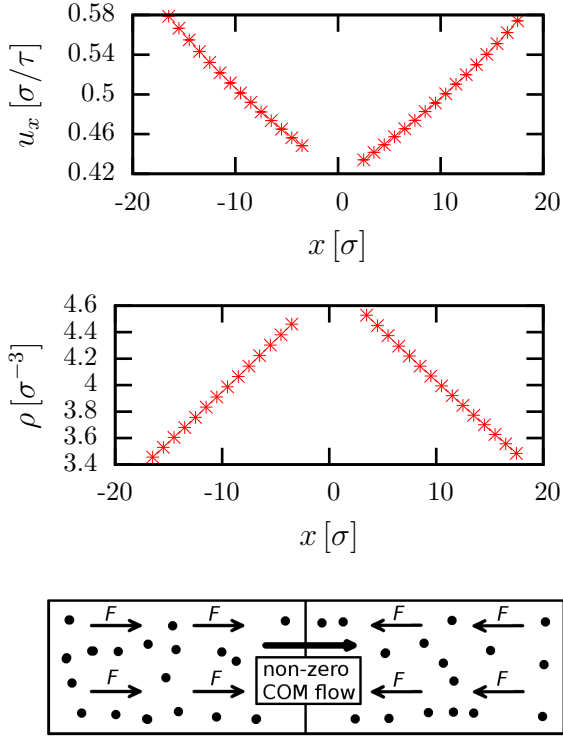
Figure B.3: Force-driven method to generate a steady-state divergent flow. Bottom panel illustrates the idea of the method, including the generation of a non-zero center-of-mass (COM) flow. Upper panels show the emerging velocity profile (top) and density profile (middle) of a DPD fluid with density $\rho = 4\,\sigma^{-3}$. Figure adapted from Ref. 17.

The main disadvantage of this technique is that the gradient in the flow field is unavoidably associated with a density gradient. This is a problem because the bulk viscosity strongly depends on the density. One can reduce the problem by applying a very small force. However, very long simulations are then necessary to obtain sufficiently good statistics and the method would be restricted to the linear response regime. The solution proposed in this thesis is to calculate a bulk viscosity ζ for every bin in the simulation box and associate it to the density in the respective box. In this way one obtains many data points for various densities that can be used to determine not only the bulk viscosity for a constant density but also the density-dependence.

C

The Discretized Fluctuation-Dissipation Theorem

This chapter is reproduced from the publication "Iterative reconstruction of memory kernels", Gerhard Jung, Martin Hanke and Friederike Schmid, *Journal of Chemical Theory and Computation*, **13**, 2481 (2017)

In this chapter, we derive the discrete version of the fluctuation-dissipation theorem for a generalized Langevin equation with discretized memory kernel (see Eq. 13.3),

$$M\dot{\boldsymbol{V}}(t) = -\sum_{m=0}^{T-1} \boldsymbol{K}_m \boldsymbol{V}(t - m\Delta t) + \partial \boldsymbol{F}(t), \tag{C.1}$$

with an arbitrary $3N \times 3N$-dimensional memory sequence $\boldsymbol{K}_m$ for $m = 0, ..., T-1$ and a finite time step Δt. To derive the fluctuation-dissipation theorem we first identify the frequency-dependent response $\hat{\boldsymbol{\gamma}}(\omega)$ of the discretized memory kernel by Fourier transform of Eq. C.1,

$$\hat{\boldsymbol{V}}(\omega) = [\mathrm{i}\omega M \boldsymbol{I} + \hat{\boldsymbol{\gamma}}(\omega)]^{-1} \partial \hat{\boldsymbol{F}}(\omega), \tag{C.2}$$

$$\text{with } \hat{\boldsymbol{\gamma}}(\omega) = \sum_{m=0}^{T-1} \boldsymbol{K}_m e^{-\mathrm{i}wm\Delta t}. \tag{C.3}$$

Here, $\hat{\boldsymbol{V}}(\omega)$ denotes the Fourier transform of the velocity,

$$\hat{\boldsymbol{V}}(\omega) = \int_{-\infty}^{\infty} \mathrm{d}t e^{-\mathrm{i}wt} \boldsymbol{V}(t), \tag{C.4}$$

and similarly $\partial \hat{\boldsymbol{F}}(\omega)$ the Fourier transform of the random force. Following the derivation of Hauge and Martin-Löf[165] of the fluctuation-dissipation theorem for continuous memory kernels, we can identify the power-spectrum $\hat{C}_{\partial \boldsymbol{F}}(\omega)$ of the random force, defined as the Fourier transform of the random force correlation function,

$$\hat{\boldsymbol{C}}_{\partial \boldsymbol{F}}(\omega) = 2k_B T \Re\{\hat{\boldsymbol{\gamma}}(\omega)\} = 2k_B T \sum_{m=0}^{T-1} \boldsymbol{K}_m \cos(wm\Delta t), \tag{C.5}$$

with the real part $\Re\{\hat{\boldsymbol{\gamma}}(\omega)\}$ of the response function. By inverse Fourier transform

we finally find the fluctuation-dissipation theorem,

$$\langle \partial \boldsymbol{F}(t) \partial \boldsymbol{F}(t') \rangle = k_B T \sum_{m=0}^{T-1} a_m \boldsymbol{K}_m \delta(t - t' - m\Delta t), \tag{C.6}$$

with the weight factor $a_0 = 2$ and $a_m = 1$ for $m \neq 0$. The most important implication of this equation is the factor of 2 that enters the instantaneous contribution of the correlation function. This factor is also present in the fluctuation-dissipation theorem for the Langevin equation without memory. The presented results can be directly applied to the specific generalized Langevin equation considered in Section 13.1.

D

About the Auxiliary Variable Expansion

In the literature, the most popular approach to include non-Markovian dynamics into coarse-grained models is the auxiliary variable expansion.[109;139–141;144] The idea behind this approach is to add additional, auxiliary variables to the system with Markovian dynamics. These variables couple to the dynamical variables in the original coarse-grained system and thus mimic the non-Markovian dynamics, although the equations of motion are purely Markovian. The auxiliary variables are determined by fitting (complex) exponentials to the memory kernel. However, it was not possible to adapt this procedure to the coarse-grained models considered in this thesis, including self- and pair-memory kernels. For future reference, we want to shortly sketch the problems that occur in this context.

To integrate the N-particle generalized Langevin equation (13.1) we start with the following approach,

$$\begin{pmatrix} \dot{\boldsymbol{V}}(t) \\ \dot{\boldsymbol{s}}(t) \end{pmatrix} = \begin{pmatrix} \boldsymbol{F}^{\mathrm{C}}(t) \\ 0 \end{pmatrix} - \begin{pmatrix} \boldsymbol{0} & \boldsymbol{A}^{vs} \\ \boldsymbol{A}^{sv} & \boldsymbol{A}^{ss} \end{pmatrix} \begin{pmatrix} \boldsymbol{V}(t) \\ \boldsymbol{s}(t) \end{pmatrix} + \begin{pmatrix} \boldsymbol{0} & \boldsymbol{0} \\ \boldsymbol{0} & \boldsymbol{B} \end{pmatrix} \begin{pmatrix} \boldsymbol{0} \\ \zeta(t) \end{pmatrix}, \qquad \text{(D.1)}$$

with the auxiliary variables $\boldsymbol{s}(t)$, the coupling matrices $\boldsymbol{A}^{vs}$, $\boldsymbol{A}^{sv}$ and the dissipative matrices $\boldsymbol{A}^{ss}$. We also introduce uncorrelated Gaussian white noise $\zeta(t)$ with zero mean and unit variance. If the matrices $\boldsymbol{A}^{ss}$ are diagonal, the matrices $\boldsymbol{B}$ are defined by the fluctuation-dissipation theorem $\boldsymbol{B}\boldsymbol{B}^{\mathrm{T}} = \boldsymbol{A}^{ss} + \boldsymbol{A}^{ss\mathrm{T}}$. The $2KN$-dimensional vector $\boldsymbol{s}(t)$ consists of K uncoupled auxiliary variables $\boldsymbol{s}_k(t)$. In the following, the subscript $k = 0, ..., K-1$ will be used to refer to submatrices that relate to the auxiliary variable $\boldsymbol{s}_k(t)$. Solving the linear equations (D.1) for the auxiliary variables,

$$\boldsymbol{s}_k(t) = \sum_{k=0}^{K-1} \int_0^t \mathrm{d}t' e^{-(t-t')\boldsymbol{A}_k^{ss}} \left(\boldsymbol{A}_k^{sv} \boldsymbol{V}(t') + \boldsymbol{B}_k \zeta_k(t') \right), \qquad \text{(D.2)}$$

and inserting this result back into the original approach shows that Eq. (D.1) indeed corresponds to a generalized Langevin equation,

$$M\dot{\boldsymbol{V}}(t) = \boldsymbol{F}^{\mathrm{C}}(t) - \sum_{k=0}^{K-1} \left(\int_0^t \mathrm{d}s \boldsymbol{K}_k(t-s)\boldsymbol{V}(t) + \partial \boldsymbol{F}_k(t) \right). \qquad \text{(D.3)}$$

Here, the memory kernel is

$$\boldsymbol{K}_k(t) = -M\boldsymbol{A}_k^{vs}e^{-t\boldsymbol{A}_k^{ss}}\boldsymbol{A}_k^{sv}, \tag{D.4}$$

and the correlation function of the random force is given by

$$\langle \partial\boldsymbol{F}_k(t)\partial\boldsymbol{F}_k(t')\rangle = k_{\mathrm{B}}TM^2\boldsymbol{A}_k^{vs}e^{-(t-t')\boldsymbol{A}_k^{ss}}\boldsymbol{A}_k^{vsT}. \tag{D.5}$$

To fulfill the fluctuation-dissipation theorem we therefore have to define $\mathbf{A}_k^{vs} = -M^{-1}\mathbf{A}_k^{svT}$. To simplify the notation we will also choose

$$\mathbf{A}_k^{ss} = \begin{pmatrix} \mathbf{A}_k^{\prime ss} & 0 & 0 \\ 0 & ... & 0 \\ 0 & 0 & \mathbf{A}_k^{\prime ss} \end{pmatrix} \quad \text{with} \quad \mathbf{A}_k^{\prime ss} = \begin{pmatrix} q_k & r_k \\ -r_k & q_k \end{pmatrix}, \tag{D.6}$$

and introduce the reduced $N \times N$-dimensional coupling matrices $\boldsymbol{A}_k^{\prime sv}$,

$$A_{k,ij}^{sv} = A_{k,(2i)j}^{\prime sv} \text{ for even } i, \tag{D.7}$$

$$A_{k,ij}^{sv} = 0 \qquad \text{for odd } i. \tag{D.8}$$

This finally leads to

$$\mathbf{K}_k(t) = \mathbf{A}_k^{\prime svT}\mathbf{A}_k^{\prime sv}e^{-q_kt}\cos(r_kt) = \mathbf{P}_ke^{-q_kt}\cos(r_kt). \tag{D.9}$$

The coupling matrices $\boldsymbol{A}_k^{\prime sv}$ thus have to be determined by Cholesky-decomposition from the matrices $\boldsymbol{P}_k$ that contain the amplitudes of the complex exponential functions that are fitted to the self- and pair-memory kernels. In simulations, however, we observed that the inclusion of self- and pair-memory kernels often leads to fitting matrices $\boldsymbol{P}^k$ that are not positive definite, which makes the determination of $\boldsymbol{A}_k^{\prime sv}$ impossible. This observation is also intuitively accessible: When fitting the exponential functions to the distance-dependent memory kernels, the distance-dependence of the fitting parameters can be very complicated and discontinuous. In a system with three particles, it will therefore occur that for an auxiliary variable k one of the particles is strongly correlated with the others, while the others are anti-correlated with each other. This problem can be reduced by strongly restricting the fitting parameters. However, for large systems it was not possible to find a suitable auxiliary variable expansion.

If it is possible to replace the GLE (13.1) by Markovian equations of motion with additional degrees of freedom, the construction of these Markov models has to be based on more sophisticated methods than an *a posteriori* fitting of memory kernels, as derived in this chapter. One possible idea could be the construction of hidden Markov models that are directly based on the microscopic dynamics,[166] which could be an interesting project for future research.

About the Long-Time Behavior of Non-Markovian Models

In Section 14.3 we have already analyzed the transferability of the non-Markovian coarse-grained model derived in Chapter 14 to various nanocolloid densities ρ . Here, we study the long-time behavior of the correlation functions. The results are shown
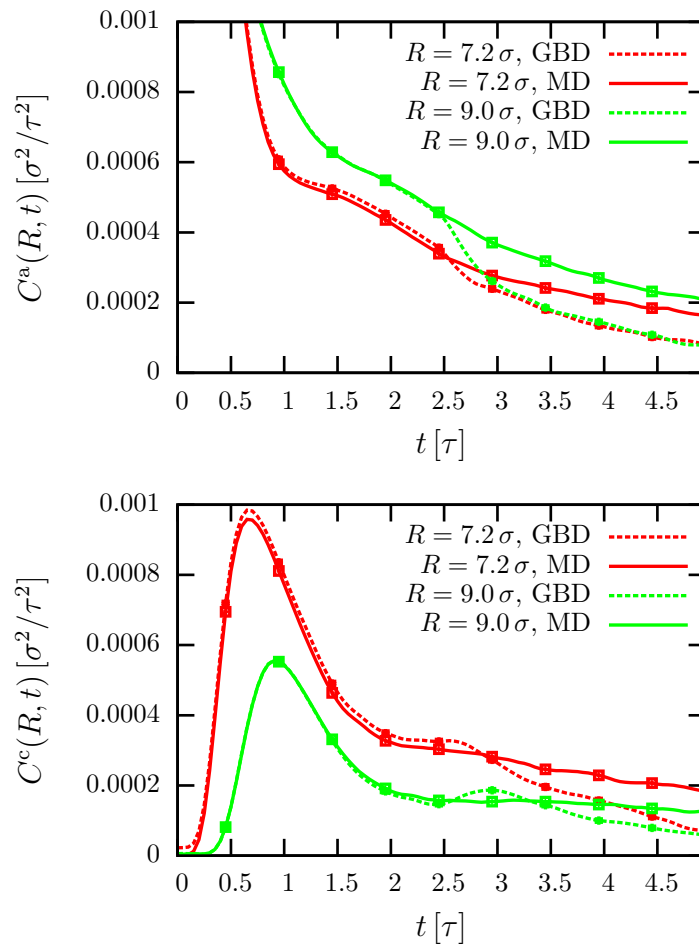

Figure E.1: Hydrodynamic auto- and cross-correlation functions of nanocolloids in dispersion for different particle distances R. The generalized Brownian dynamics (GBD) simulations use the memory kernels derived in Section 14.2. The upper and lower figure illustrate the velocity auto- (upper) and cross- (lower) correlation function determined from GBD and molecular dynamics (MD) simulations. To visualize the statistical errors, ten data points with y-error bars are included in the curves.

in Figure E.1. For times larger than the memory time scale, $t > \tau_{\mathrm{mem}} = T \Delta t_{\mathrm{GLE}}$ a significant decrease of both correlation functions can be observed. This is expected, because the cutoff of the memory interrupts the backflow effect that leads to a strong correlation of the particles. In the microscopic system, this backflow effect leads to the long-time tails in the velocity correlation functions,[40] which thus cannot be reproduced in the non-Markovian model. The only way to prevent this decline in the correlation functions is by increasing the memory cutoff T. This will, however, reduce the efficiency of the method, since the total computation time scales linearly with the cutoff T. For the effective application of the GBD technique it is thus important to analyze on which time scale the memory ought to be considered.

Bibliography

[1] Navier, C. L. M. H. Mémoire sur les lois du mouvement des fluides. *Mémoires de l'Académie Royale des Sciences de l'Institut de France* **1823**, *6*.

[2] Stokes, G. G. On the theories of the internal friction in fluids in motion, and of the equilibrium and motion of elastic solids. *Trans. Cambridge Phil. Soc.* **1845**, *8*, 287.

[3] https://mdx2.plm.automation.siemens.com/cfdImage/external-aerodynamic-analysis-renault-r28-1. *April 12th 2018*

[4] http://x3training.com/how-aero-is-your-aero/. *April 12th 2018*

[5] Jung, G.; Schmid, F. Frequency-dependent hydrodynamic interaction between two solid spheres. *Physics of Fluids* **2017**, *29*, 126101.

[6] http://www.claymath.org/millennium-problems/navier%E2%80%93stokes-equation. *April 12th 2018*

[7] Mazur, P.; Bedeaux, D. A generalization of Faxén's theorem to nonsteady motion of a sphere through an incompressible fluid in arbitrary flow. *Physica* **1974**, *76*, 235–246.

[8] Green, G. An Essay on the Application of Mathematical Analysis to the Theories of Electricity and Magnetism. *Nottingham, England: T. Wheelhouse* **1828**, 10.

[9] Lees, a. W.; Edwards, S. F. The computer study of transport processes under extreme conditions. *Journal of Physics C: Solid State Physics* **1972**, *5*, 1921–1928.

[10] Ashurst, W. T.; Hoover, W. G. Argon Shear Viscosity via a Lennard-Jones Potential with Equilibrium and Nonequilibrium Molecular Dynamics. *Physical Review Letters* **1973**, *31*, 206–208.

[11] Müller-Plathe, F. Reversing the perturbation in nonequilibrium molecular dynamics: An easy way to calculate the shear viscosity of fluids. *Physical Review E* **1999**, *59*, 4894–4898.

[12] Backer, J. A.; Lowe, C. P.; Hoefsloot, H. C. J.; Iedema, P. D. Poiseuille flow to measure the viscosity of particle model fluids. *The Journal of Chemical Physics* **2005**, *122*, 154503.

[13] Zhou, J.; Smiatek, J.; Asmolov, E. S.; Vinogradova, O. I.; Schmid, F. Application of Tunable-Slip Boundary Conditions in Particle-Based Simulations. *Springer HPC '14* **2014**, 19.

[14] Green, M. S. Markoff Random Processes and the Statistical Mechanics of Time-Dependent Phenomena. II. Irreversible Processes in Fluids. *The Journal of Chemical Physics* **1954**, *22*, 398–413.

[15] Kubo, R. Statistical-Mechanical Theory of Irreversible Processes. I. General Theory and Simple Applications to Magnetic and Conduction Problems. *Journal of the Physical Society of Japan* **1957**, *12*, 570–586.

[16] Helfand, E. Transport Coefficients from Dissipation in a Canonical Ensemble. *Physical Review* **1960**, *119*, 1–9.

[17] Jung, G.; Schmid, F. Computing bulk and shear viscosities from simulations of fluids with dissipative and stochastic interactions. *The Journal of Chemical Physics* **2016**, *144*, 204104.

[18] Hoover, W. G.; Evans, D. J.; Hickman, R. B.; Ladd, A. J. C.; Ashurst, W. T.; Moran, B. Lennard-Jones triple-point bulk and shear viscosities. Green-Kubo theory, Hamiltonian mechanics, and nonequilibrium molecular dynamics. *Physical Review A* **1980**, *22*, 1690–1697.

[19] Goldhirsch, I.; van Noije, T. P. Green-Kubo relations for granular fluids. *Physical Review E - Statistical Physics, Plasmas, Fluids, and Related Interdisciplinary Topics* **2000**, *61*, 3241–3244.

[20] Wesp, C.; El, A.; Reining, F.; Xu, Z.; Bouras, I.; Greiner, C. Calculation of shear viscosity using Green-Kubo relations within a parton cascade. *Physical Review C* **2011**, *84*, 054911.

[21] Ernst, M. H.; Dorfman, J. R. Nonanalytic dispersion relations for classical fluids. *Journal of Statistical Physics* **1975**, *12*, 311–359.

[22] Evans, D. J.; Morriss, G. P. *Statistical Mechanics of Nonequilibrium Liquids. Chapter 4. The Green Kubo Relations.*; 1990 Academic Press Limited, 1990.

[23] Ernst, M. H.; Brito, R. Generalized Green-Kubo formulas for fluids with impulsive, dissipative, stochastic, and conservative interactions. *Physical Review E - Statistical, Nonlinear, and Soft Matter Physics* **2005**, *72*, 1–11.

[24] Moyses, H.; Palacci, J.; Sacanna, S.; Grier, D. G. Trochoidal trajectories of self-propelled Janus particles in a diverging laser beam. *Soft Matter* **2016**, *12*, 6357–6364.

[25] Gong, T.; Shen, J.; Hu, Z.; Marquez, M.; Cheng, Z. Nucleation Rate Measurement of Colloidal Crystallization Using Microfluidic Emulsion Droplets. *Langmuir* **2007**, *23*, 2919–2923.

[26] Palberg, T. Crystallization kinetics of repulsive colloidal spheres. *Journal of Physics: Condensed Matter* **1999**, *11*, R323–R360.

[27] Vermant, J.; Solomon, M. J. Flow-induced structure in colloidal suspensions. *Journal of Physics: Condensed Matter* **2005**, *17*, R187–R216.

[28] Zahn, K.; Lenke, R.; Maret, G. Two-Stage Melting of Paramagnetic Colloidal Crystals in Two Dimensions. *Physical Review Letters* **1999**, *82*, 2721–2724.

[29] Thorneywork, A. L.; Abbott, J. L.; Aarts, D. G.; Dullens, R. P. Two-Dimensional Melting of Colloidal Hard Spheres. *Physical Review Letters* **2017**, *118*, 158001.

[30] De Jong, W. H.; Borm, P. J. a. Drug delivery and nanoparticles:applications and hazards. *International Journal of Nanomedicine* **2008**, *3*, 133–149.

[31] Ristenpart, W. D.; Aksay, I. A.; Saville, D. A. Electrically Guided Assembly of Planar Superlattices in Binary Colloidal Suspensions. *Physical Review Letters* **2003**, *90*, 4.

[32] Thutupalli, S.; Seemann, R.; Herminghaus, S. Swarming behavior of simple model squirmers. *New Journal of Physics* **2011**, *13*, 073021.

[33] Cohen, J. A.; Golestanian, R. Emergent Cometlike Swarming of Optically Driven Thermally Active Colloids. *Physical Review Letters* **2014**, *112*, 068302.

[34] Yethiraj, A.; van Blaaderen, A. A colloidal model system with an interaction tunable from hard sphere to soft and dipolar. *Nature* **2003**, *421*, 513–517.

[35] Reiss, H.; Frisch, H. L.; Lebowitz, J. L. Statistical Mechanics of Rigid Spheres. *The Journal of Chemical Physics* **1959**, *31*, 369–380.

[36] Alder, B. J.; Wainwright, T. E. Phase Transition for a Hard Sphere System. *The Journal of Chemical Physics* **1957**, *27*, 1208–1209.

[37] Bernard, E. P.; Krauth, W. Two-Step Melting in Two Dimensions: First-Order Liquid-Hexatic Transition. *Physical Review Letters* **2011**, *107*, 155704.

[38] Wang, Y.; Wang, Y.; Zheng, X.; Ducrot, É.; Yodh, J. S.; Weck, M.; Pine, D. J. Crystallization of DNA-coated colloids. *Nature Communications* **2015**, *6*, 7253.

[39] Boniello, G.; Malinge, J.; Tribet, C.; Marie, E.; Zanchi, D. Reversible and dynamical control of aggregation and soft adhesion of T-responsive polymer-coated colloids. *Colloids and Surfaces A: Physicochemical and Engineering Aspects* **2017**, *532*, 510–515.

[40] Alder, B. J.; Wainwright, T. E. Decay of the Velocity Autocorrelation Function. *Physical Review A* **1970**, *1*, 18–21.

[41] Happel, J.; Brenner, H. *Low Reynolds number hydrodynamics : with special applications to particulate media*; Prentice-Hall, Englewood Cliffs, NJ, 1963.

[42] Dhont, J. K. G. *An introduction to dynamics of colloids*; Elsevier, 1996.

[43] Ardekani, A. M.; Rangel, R. H. Unsteady motion of two solid spheres in Stokes flow. *Physics of Fluids* **2006**, *18*, 103306.

[44] Salonen, E.; Terama, E.; Vattulainen, I.; Karttunen, M. Dielectrophoresis of nanocolloids: A molecular dynamics study. *European Physical Journal E* **2005**, *18*, 133–142.

[45] Regtmeier, J.; Eichhorn, R.; Bogunovic, L.; Ros, A.; Anselmetti, D. Dielectrophoretic Trapping and Polarizability of DNA: The Role of Spatial Conformation. *Analytical Chemistry* **2010**, *82*, 7141–7149.

[46] Maxwell, J. C. *Lehrbuch der Electricität und des Magnetismus*; 1883; p 592.

[47] Wagner, K. W. Erklärung der dielektrischen Nachwirkungsvorgänge auf Grund Maxwellscher Vorstellungen. *Archiv für Elektrotechnik* **1914**, *2*, 371–387.

[48] Saville, D. A.; Bellini, T.; Degiorgio, V.; Mantegazza, F. Extended Maxwell-Wagner theory for the electric birefringence of charged colloids. *Journal of Chemical Physics* **2000**, *113*, 6974–6983.

[49] Zhou, J.; Schmitz, R.; Dünweg, B.; Schmid, F. Dynamic and dielectric response of charged colloids in electrolyte solutions to external electric fields. *The Journal of Chemical Physics* **2013**, *139*, 024901.

[50] https://en.wikipedia.org/wiki/Zeta_potential. *April 12th 2018*

[51] O'Brien, R. W.; White, L. R. Electrophoretic mobility of a spherical colloidal particle. *Journal of the Chemical Society, Faraday Transactions 2* **1978**, *74*, 1607.

[52] Hill, R. J.; Saville, D. A.; Russel, W. B. High-frequency dielectric relaxation of spherical colloidal particles. *Physical Chemistry Chemical Physics* **2003**, *5*, 911–915.

[53] Schmitz, R.; Dünweg, B. Numerical electrokinetics. *Journal of Physics: Condensed Matter* **2012**, *24*, 464111.

[54] O'Konski, C. T. Electric properties of macromolecules. V. theory of ionic polarization in polyelectrlytes. *The Journal of Physical Chemistry* **1960**, *64*, 605–619.

[55] Mittal, M.; Lele, P. P.; Kaler, E. W.; Furst, E. M. Polarization and interactions of colloidal particles in ac electric fields. *The Journal of Chemical Physics* **2008**, *129*, 064513.

[56] Morgan, S. O. Two Types of Dielectric Polarization. *Transactions of The Electrochemical Society* **1934**, *65*, 109.

[57] Hogan, M.; Dattagupta, N.; Crothers, D. M. Transient electric dichroism of rod-like DNA molecules. *Proceedings of the National Academy of Sciences* **1978**, *75*, 195–199.

[58] Rau, D. C.; Bloomfield, V. A. Transient electric birefringence of T7 viral DNA. *Biopolymers* **1979**, *18*, 2783–2805.

[59] Elias, J. G.; Eden, D. Transient electric birefringence study of the persistence length and electrical polarizability of restriction fragments of DNA. *Macromolecules* **1981**, *14*, 410–419.

[60] Ito, K.; Yagi, A.; Ookubo, N.; Hayakawa, R. Crossover behavior in high-frequency dielectric relaxation of linear polyions in dilute and semidilute solutions. *Macromolecules* **1990**, *23*, 857–862.

[61] Bellini, T.; Mantegazza, F.; Degiorgio, V.; Avallone, R.; Saville, D. A. Electric Polarizability of Polyelectrolytes: Maxwell-Wagner and Electrokinetic Relaxation. *Physical Review Letters* **1999**, *82*, 5160–5163.

[62] Bordi, F.; Cametti, C.; Colby, R. H. Dielectric spectroscopy and conductivity of polyelectrolyte solutions. *Journal of Physics: Condensed Matter* **2004**, *16*, R1423–R1463.

[63] Katsumoto, Y.; Omori, S.; Yamamoto, D.; Yasuda, A.; Asami, K. Dielectric dispersion of short single-stranded DNA in aqueous solutions with and without added salt. *Physical Review E - Statistical, Nonlinear, and Soft Matter Physics* **2007**, *75*, 1–9.

[64] Mandel, M. The electric polarization of rod-like, charged macromolecules. *Molecular Physics* **1961**, *4*, 489–496.

[65] Oosawa, F. Counterion fluctuation and dielectric dispersion in linear polyelectrolytes. *Biopolymers* **1970**, *9*, 677–688.

[66] Fixman, M. Charged macromolecules in external fields. I. The sphere. *The Journal of Chemical Physics* **1980**, *72*, 5177–5186.

[67] Rau, D. C.; Charney, E. Polarization of the ion atmosphere of a charged cylinder. *Biophysical Chemistry* **1981**, *14*, 1–9.

[68] Bowers, J. S.; Prud'homme, R. K. Low field theory of polymer transient electric birefringence. *The Journal of Chemical Physics* **1992**, *96*, 7135–7143.

[69] Mohanty, U.; Zhao, Y. Polarization of counterions in polyelectrolytes. *Biopolymers* **1996**, *38*, 377–88.

[70] Zhao, H. Role of hydrodynamic behavior of DNA molecules in dielectrophoretic polarization under the action of an electric field. *Physical Review E* **2011**, *84*, 021910.

[71] Washizu, H.; Kikuchi, K. Electric Polarizability of DNA in Aqueous Salt Solution. *The Journal of Physical Chemistry B* **2006**, *110*, 2855–2861.

[72] Schlagberger, X.; Netz, R. R. Anomalous birefringence and polarizability saturation of charged elastic rods: Field-strength, salt and finite-concentration effects. *EPL (Europhysics Letters)* **2008**, *83*, 36003.

[73] Fischer, S. *Polyelectrolytes in Electric Fields (PhD thesis)*; 2009.

[74] Kasper, S. *Novel Applications for Condiff Algorithm (MSc thesis)*; 2017.

[75] Marrink, S. J.; Risselada, H. J.; Yefimov, S.; Tieleman, D. P.; de Vries, A. H. The MARTINI Force Field: Coarse Grained Model for Biomolecular Simulations. *The Journal of Physical Chemistry B* **2007**, *111*, 7812–7824.

[76] Bradley, R.; Radhakrishnan, R. Coarse-grained models for protein-cell membrane interactions. *Polymers* **2013**, *5*, 890–936.

[77] Izvekov, S.; Parrinello, M.; Burnham, C. J.; Voth, G. A. Effective force fields for condensed phase systems from ab initio molecular dynamics simulation: A new method for force-matching. *The Journal of Chemical Physics* **2004**, *120*, 10896–10913.

[78] Lyubartsev, A. P.; Laaksonen, A. Calculation of effective interaction potentials from radial distribution functions: A reverse Monte Carlo approach. *Physical Review E* **1995**, *52*, 3730–3737.

[79] Reith, D.; Pütz, M.; Müller-Plathe, F. Deriving effective mesoscale potentials from atomistic simulations. *Journal of Computational Chemistry* **2003**, *24*, 1624–1636.

[80] Shell, M. S. The relative entropy is fundamental to multiscale and inverse thermodynamic problems. *The Journal of Chemical Physics* **2008**, *129*, 144108.

[81] Henderson, R. A uniqueness theorem for fluid pair correlation functions. *Physics Letters A* **1974**, *49*, 197–198.

[82] Hanke, M. Well-Posedness of the Iterative Boltzmann Inversion. *Journal of Statistical Physics* **2018**, *170*, 536–553.

[83] Jung, G.; Hanke, M.; Schmid, F. Iterative Reconstruction of Memory Kernels. *Journal of Chemical Theory and Computation* **2017**, *13*, 2481–2488.

[84] Plimpton, S. Fast Parallel Algorithms for Short-Range Molecular Dynamics. *Journal of Computational Physics* **1995**, *117*, 1–19.

[85] Zwanzig, R. Memory Effects in Irreversible Thermodynamics. *Physical Review* **1961**, *124*, 983–992.

[86] Mori, H. Transport, Collective Motion, and Brownian Motion. *Progress of Theoretical Physics* **1965**, *33*, 423–455.

[87] Zwanzig, R. *Nonequilibrium statistical mechanics*; Oxford University Press, 2001.

[88] Kinjo, T.; Hyodo, S.-a. Equation of motion for coarse-grained simulation based on microscopic description. *Physical Review E* **2007**, *75*, 051109.

[89] Kubo, R. The fluctuation-dissipation theorem. *Reports on Progress in Physics* **1966**, *29*, 306.

[90] Schnurr, B.; Gittes, F.; MacKintosh, F. C.; Schmidt, C. F. Determining Microscopic Viscoelasticity in Flexible and Semiflexible Polymer Networks from Thermal Fluctuations. *Macromolecules* **1997**, *30*, 7781–7792.

[91] Fricks, J.; Yao, L.; Elston, T. C.; Forest, M. G. Time-Domain Methods for Diffusive Transport in Soft Matter. *SIAM Journal on Applied Mathematics* **2009**, *69*, 1277–1308.

[92] Shin, H. K.; Kim, C.; Talkner, P.; Lee, E. K. Brownian motion from molecular dynamics. *Chemical Physics* **2010**, *375*, 316–326.

[93] Carof, A.; Vuilleumier, R.; Rotenberg, B. Two algorithms to compute projected correlation functions in molecular dynamics simulations. *The Journal of Chemical Physics* **2014**, *140*, 124103.

[94] Lesnicki, D.; Vuilleumier, R.; Carof, A.; Rotenberg, B. Molecular Hydrodynamics from Memory Kernels. *Physical Review Letters* **2016**, *116*, 147804.

[95] Lei, H.; Baker, N. A.; Li, X. Data-driven parameterization of the generalized Langevin equation. *Proceedings of the National Academy of Sciences* **2016**, *113*, 14183–14188.

[96] Alder, B. J.; Wainwright, T. E. Studies in Molecular Dynamics. I. General Method. *The Journal of Chemical Physics* **1959**, *31*, 459–466.

[97] Verlet, L. Computer "Experiments" on Classical Fluids. I. Thermodynamical Properties of Lennard-Jones Molecules. *Physical Review* **1967**, *159*, 98–103.

[98] Kohn, W.; Sham, L. J. Self-Consistent Equations Including Exchange and Correlation Effects. *Physical Review* **1965**, *140*, A1133–A1138.

[99] Rahman, A. *Correlation Functions and Quasiparticle Interactions in Condensed Matter. Numerical Calculations in Classical Liquids.*; NATO Advanced Study Institute Series, 1978.

[100] Car, R.; Parrinello, M. Unified Approach for Molecular Dynamics and Density-Functional Theory. *Physical Review Letters* **1985**, *55*, 2471–2474.

[101] Weiner, P. K.; Kollman, P. A. AMBER: Assisted model building with energy refinement. A general program for modeling molecules and their interactions. *Journal of Computational Chemistry* **1981**, *2*, 287–303.

[102] Cornell, W. D.; Cieplak, P.; Bayly, C. I.; Gould, I. R.; Merz, K. M.; Ferguson, D. M.; Spellmeyer, D. C.; Fox, T.; Caldwell, J. W.; Kollman, P. A. A Second Generation Force Field for the Simulation of Proteins, Nucleic Acids, and Organic Molecules. *Journal of the American Chemical Society* **1995**, *117*, 5179–5197.

[103] Frenkel, D.; Smit, B. *Understanding Molecular Simulation*; Elsevier, 2002.

[104] Allen, M. P.; Tildesley, D. J. *Computer simulation of liquids*; Clarendon Press, 1989; p 385.

[105] Hoogerbrugge, P. J.; Koelman, J. M. V. A. Simulating Microscopic Hydrodynamic Phenomena with Dissipative Particle Dynamics. *Europhysics Letters (EPL)* **1992**, *19*, 155–160.

[106] Español, P.; Warren, P. Statistical Mechanics of Dissipative Particle Dynamics. *Europhysics Letters (EPL)* **1995**, *30*, 191–196.

[107] Medina, S.; Zhou, J.; Wang, Z.-G.; Schmid, F. An efficient dissipative particle dynamics-based algorithm for simulating electrolyte solutions. *The Journal of Chemical Physics* **2015**, *142*, 024103.

[108] Li, Z.; Bian, X.; Li, X.; Karniadakis, G. E. Incorporation of memory effects in coarse-grained modeling via the Mori-Zwanzig formalism. *The Journal of Chemical Physics* **2015**, *143*, 243128.

[109] Li, Z.; Lee, H. S.; Darve, E.; Karniadakis, G. E. Computing the non-Markovian coarse-grained interactions derived from the Mori-Zwanzig formalism in molecular systems: Application to polymer melts. *The Journal of Chemical Physics* **2017**, *146*, 014104.

[110] Hijón, C.; Español, P.; Vanden-Eijnden, E.; Delgado-Buscalioni, R. Mori-Zwanzig formalism as a practical computational tool. *Faraday Discuss.* **2010**, *144*, 301–322.

[111] Izvekov, S. Mori-Zwanzig theory for dissipative forces in coarse-grained dynamics in the Markov limit. *Physical Review E* **2017**, *95*.

[112] Español, P.; Warren, P. B. Perspective: Dissipative particle dynamics. *The Journal of Chemical Physics* **2017**, *146*, 150901.

[113] Medina, S. H. *A Mesoscopic Simulation Method for Electrolyte Solutions (PhD thesis)*; 2013.

[114] Frisch, U.; Hasslacher, B.; Pomeau, Y. Lattice-Gas Automata for the Navier-Stokes Equation. *Physical Review Letters* **1986**, *56*, 1505–1508.

[115] McNamara, G. R.; Zanetti, G. Use of the Boltzmann Equation to Simulate Lattice-Gas Automata. *Physical Review Letters* **1988**, *61*, 2332–2335.

[116] Malevanets, A.; Kapral, R. Mesoscopic model for solvent dynamics. *The Journal of Chemical Physics* **1999**, *110*, 8605–8613.

[117] Noguchi, H.; Kikuchi, N.; Gompper, G. Particle-based mesoscale hydrodynamic techniques. *Europhysics Letters (EPL)* **2007**, *78*, 10005.

[118] Dünweg, B.; Ladd, A. J. C. *Advanced Computer Simulation Approaches for Soft Matter Sciences III*; Springer Berlin Heidelberg: Berlin, Heidelberg, 2008; pp 89–166.

[119] Marsh, C. A.; Backx, G.; Ernst, M. H. Static and dynamic properties of dissipative particle dynamics. *Physical Review E* **1997**, *56*, 1676–1691.

[120] Ewald, P. P. Die Berechnung optischer und elektrostatischer Gitterpotentiale. *Annalen der Physik* **1921**, *369*, 253–287.

[121] Eastwood, J.; Hockney, R.; Lawrence, D. P3M3DP-the three-dimensional periodic particle-particle/particle-mesh program. *Computer Physics Communications* **1984**, *35*, C–618–C–619.

[122] Risken, H. *The Fokker-Planck Equation - Methods of Solution and Applications*; Springer, 1988.

[123] Ermak, D. L. A computer simulation of charged particles in solution. I. Technique and equilibrium properties. *The Journal of Chemical Physics* **1975**, *62*, 4189–4196.

[124] van Gunsteren, W.; Berendsen, H. Algorithms for brownian dynamics. *Molecular Physics* **1982**, *45*, 637–647.

[125] Brady, J. F.; Bossis, G. Stokesian Dynamics. *Annual Review of Fluid Mechanics* **1988**, *20*, 111–157.

[126] Hernando, S. M. *A Mesoscopic Simulation Method for Electrolyte Solutions (PhD thesis)*; 2013.

[127] Dobrynin, A. V.; Rubinstein, M.; Obukhov, S. P. Cascade of transitions of polyelectrolytes in poor solvents. *Macromolecules* **1996**, *29*, 2974–2979.

[128] Lyulin, A. V.; Dünweg, B.; Borisov, O. V.; Darinskii, A. A. Computer simulation studies of a single polyelectrolyte chain in poor solvent. *Macromolecules* **1999**, *32*, 3264–3278.

[129] Hodgson, D. F.; Amis, E. J. Dilute solution behavior of cyclic and linear polyelectrolytes. *The Journal of Chemical Physics* **1991**, *95*, 7653–7663.

[130] Robertson, R. M.; Laib, S.; Smith, D. E. Diffusion of isolated DNA molecules: Dependence on length and topology. *Proceedings of the National Academy of Sciences* **2006**, *103*, 7310–7314.

[131] Khokhlov, A.; Khachaturian, K. On the theory of weakly charged polyelectrolytes. *Polymer* **1982**, *23*, 1742–1750.

[132] Everaers, R.; Milchev, A.; Yamakov, V. The electrostatic persistence length of polymers beyond the OSF limit. *The European Physical Journal E* **2002**, *8*, 3–14.

[133] Dobrynin, A. V.; Rubinstein, M. Theory of polyelectrolytes in solutions and at surfaces. *Progress in Polymer Science (Oxford)* **2005**, *30*, 1049–1118.

[134] Soysa, W. C.; Dünweg, B.; Prakash, J. R. Size, shape, and diffusivity of a single Debye-Hückel polyelectrolyte chain in solution. *The Journal of Chemical Physics* **2015**, *143*, 064906.

[135] Humphrey, W.; Dalke, A.; Schulten, K. VMD: Visual molecular dynamics. *Journal of Molecular Graphics* **1996**, *14*, 33–38.

[136] Zhou, C.; Riehn, R. Collapse of DNA under alternating electric fields. *Physical Review E* **2015**, *92*, 012714.

[137] Irving, J. H.; Kirkwood, J. G. The Statistical Mechanical Theory of Transport Processes. IV. The Equations of Hydrodynamics. *The Journal of Chemical Physics* **1950**, *18*, 817–829.

[138] Smith, D. E.; Harris, C. B. Generalized Brownian dynamics. I. Numerical integration of the generalized Langevin equation through autoregressive modeling of the memory function. *The Journal of Chemical Physics* **1990**, *92*, 1304–1311.

[139] Ceriotti, M.; Bussi, G.; Parrinello, M. Colored-Noise Thermostats à la Carte. *Journal of Chemical Theory and Computation* **2010**, *6*, 1170–1180.

[140] Córdoba, A.; Indei, T.; Schieber, J. D. Elimination of inertia from a Generalized Langevin Equation: Applications to microbead rheology modeling and data analysis. *Journal of Rheology* **2012**, *56*, 185–212.

[141] Baczewski, A. D.; Bond, S. D. Numerical integration of the extended variable generalized Langevin equation with a positive Prony representable memory kernel. *The Journal of Chemical Physics* **2013**, *139*, 044107.

[142] Meyer, H.; Voigtmann, T.; Schilling, T. On the non-stationary generalized Langevin equation. *The Journal of Chemical Physics* **2017**, *147*, 214110.

[143] Barrat, J.-L.; Rodney, D. Portable Implementation of a Quantum Thermal Bath for Molecular Dynamics Simulations. *Journal of Statistical Physics* **2011**, *1*.

[144] Córdoba, A.; Schieber, J. D.; Indei, T. The effects of hydrodynamic interaction and inertia in determining the high-frequency dynamic modulus of a viscoelastic fluid with two-point passive microrheology. *Physics of Fluids* **2012**, *24*, 073103.

[145] Grønbech-Jensen, N.; Farago, O. A simple and effective Verlet-type algorithm for simulating Langevin dynamics. *Molecular Physics* **2013**, *111*, 983–991.

[146] Ricci, A.; Cicotti, G. Algorithms for Brownian dynamics. *Molecular Physics* **2003**, *101*, 1927–1931.

[147] Rotne, J.; Prager, S. Variational Treatment of Hydrodynamic Interaction in Polymers. *The Journal of Chemical Physics* **1969**, *50*, 4831–4837.

[148] Hochbruck, M.; Lubich, C. On Krylov Subspace Approximations to the Matrix Exponential Operator. *SIAM Journal on Numerical Analysis* **1997**, *34*, 1911–1925.

[149] Higham, N. J. *Functions of Matrices*; Society for Industrial and Applied Mathematics, 2008.

[150] Aune, E.; Eidsvik, J.; Pokern, Y. Iterative numerical methods for sampling from high dimensional Gaussian distributions. *Statistics and Computing* **2013**, *23*, 501–521.

[151] Press, W. H.; Teukolsky, S. A.; Vetterling, W. T.; Flannery, B. P. *Numerical Recipes 3rd Edition: The Art of Scientific Computing*, 3rd ed.; Cambridge University Press: New York, NY, USA, 2007.

[152] Mason, T. G.; Weitz, D. A. Optical Measurements of Frequency-Dependent Linear Viscoelastic Moduli of Complex Fluids. *Physical Review Letters* **1995**, *74*, 1250–1253.

[153] Frembgen-Kesner, T.; Elcock, A. H. Striking Effects of Hydrodynamic Interactions on the Simulated Diffusion and Folding of Proteins. *Journal of Chemical Theory and Computation* **2009**, *5*, 242–256.

[154] Manning, G. S. Limiting Laws and Counterion Condensation in Polyelectrolyte Solutions I. Colligative Properties. *The Journal of Chemical Physics* **1969**, *51*, 924–933.

[155] Schiessel, H. Counterion condensation on flexible polyelectrolytes: dependence on ionic strength and chain concentration. *Macromolecules* **1999**, *32*, 5673–5680.

[156] Deserno, M.; Holm, C.; May, S. Fraction of condensed counterions around a charged rod: Comparison of Poisson-Boltzmann theory and computer simulations. *Macromolecules* **2000**, *33*, 199–206.

[157] Naji, A.; Netz, R. R. Scaling and Universality in the Counterion-Condensation Transition at Charged Cylinders. **2005**, 1–31.

[158] Deshkovski, A.; Obukhov, S.; Rubinstein, M. Counterion Phase Transitions in Dilute Polyelectrolyte Solutions. *Physical Review Letters* **2001**, *86*, 2341–2344.

[159] Baeurle, S.; Kiselev, M.; Makarova, E.; Nogovitsin, E. Effect of the counterion behavior on the frictional–compressive properties of chondroitin sulfate solutions. *Polymer* **2009**, *50*, 1805–1813.

[160] Dysthe, D. K.; Renard, F.; Porcheron, F.; Rousseau, B. Fluid in mineral interfaces—molecular simulations of structure and diffusion. *Geophysical Research Letters* **2002**, *29*, 1109.

[161] Heyes, D. M. Thermal conductivity and bulk viscosity of simple fluids. A molecular-dynamics study. *Journal of the Chemical Society, Faraday Transactions 2* **1984**, *80*, 1363.

[162] Palla, P. L.; Pierleoni, C.; Ciccotti, G. Bulk viscosity of the Lennard-Jones system at the triple point by dynamical nonequilibrium molecular dynamics. *Physical Review E* **2008**, *78*, 021204.

[163] Hoover, W. *Computational Statistical Mechanics*; Elsevier Science, 1991; p 330.

[164] Todd, B. D.; Daivis, P. J. Elongational viscosities from nonequilibrium molecular dynamics simulations of oscillatory elongational flow. *The Journal of Chemical Physics* **1997**, *107*, 1617–1624.

[165] Hauge, E. H.; Martin-Löf, A. Fluctuating hydrodynamics and Brownian motion. *Journal of Statistical Physics* **1973**, *7*, 259–281.

[166] Baum, L. E.; Petrie, T. Statistical Inference for Probabilistic Functions of Finite State Markov Chains. *The Annals of Mathematical Statistics* **1966**, *37*, 1554–1563.